

Numerical and Analytical Study of Curvature Effects in Laminar  
Shock Wave/Boundary Layer Interactions

by

JAMES R. GRISHAM IV

Presented to the Faculty of the Graduate School of  
The University of Texas at Arlington in Partial Fulfillment  
of the Requirements  
for the Degree of

DOCTOR OF PHILOSOPHY

THE UNIVERSITY OF TEXAS AT ARLINGTON

May 2017

Numerical and Analytical Study of Curvature Effects in Laminar  
Shock Wave/Boundary Layer Interactions

The members of the Committee approve the doctoral  
dissertation of James R. Grisham IV

Frank Lu  
Supervising Professor \_\_\_\_\_

Brian Dennis \_\_\_\_\_

Guojun Liao \_\_\_\_\_

Luca Maddalena \_\_\_\_\_

Donald Wilson \_\_\_\_\_

Dean of the Graduate School \_\_\_\_\_

Copyright © by James R. Grisham IV 2017  
All Rights Reserved

To my wife, Anna, who brings much color and joy to my life.

## ACKNOWLEDGEMENTS

I would like to express deep gratitude to my advisor, Frank Lu, and co-advisor, Brian Dennis, both of whom have invested countless hours in me. I think it is fair to say that Dr. Lu took a gamble when he accepted me as a student, a gamble I am extremely grateful for. I would like to thank Professors Luca Maddalena, Guojun Liao, and Donald Wilson for serving on my committee. In particular, I would like to thank Dr. Maddalena for his excellent courses on boundary layers and high-temperature gas dynamics, as well as his inputs which have helped to improve my research work. I would also like to thank Dr. Dennis for allowing me to work under him as a research assistant for a few semesters.

I would like to acknowledge my friends from the CFDLab and Aerodynamics Research Center, especially Ashkan, Siddarth, and Dibesh, who were an endless source of encouragement and support throughout this process. I have learned so much from each of you. I am sure I will look back on our time together with great fondness.

I would like to thank NASA Langley Research Center for numerous internships, Texas Space Grant Consortium for generously supporting my studies via the Columbia Crew Memorial Scholarship and the graduate fellowship program, Lockheed Martin for its support through the Lockheed Martin Missiles and Fire Control Graduate Fellowship, and the MAE Department at UTA for its generous support through various fellowships.

The Texas Advanced Computing Center provided access to its clusters and training courses throughout this research, for which I am grateful. I would like to thank Pointwise for providing meshing software to UT Arlington.

Lastly, I would like to thank my wife, Anna, for endlessly supporting and encouraging me through all the ups-and-downs of this journey. I would also like to thank all my family for their encouragement.

April 20, 2017

## ABSTRACT

Numerical and Analytical Study of Curvature Effects in Laminar  
Shock Wave/Boundary Layer Interactions

James R. Grisham IV, Ph.D.

The University of Texas at Arlington, 2017

Supervising Professor: Frank Lu

Shock wave/boundary-layer interactions (SBLIs) are one of the most complex flow phenomena because of the different types of physics involved (i.e., viscous versus inviscid) and their side effects such as boundary layer separation and extreme localized heating. Control surfaces based on compliant mechanisms are becoming a reality and introduce an additional variable into the already complex SBLI, namely surface curvature. The purpose of the present work is to systematically study the effects of surface curvature on laminar, ramp-induced SBLIs. This is accomplished using numerical and theoretical approaches in the form of numerical solutions to the compressible Navier–Stokes equations and triple-deck theory, respectively. Results include a unique comparison between triple-deck theory and numerical solutions to the Navier–Stokes equations, a new scaling relationship involving Reynolds number, Mach number and radius of curvature, and unsteady three-dimensional results for a select case, which was undertaken to investigate the onset of unsteadiness in the nominally steady, two-dimensional SBLI.

## TABLE OF CONTENTS

ACKNOWLEDGEMENTS . . . . .	v
ABSTRACT . . . . .	vii
LIST OF ILLUSTRATIONS . . . . .	x
LIST OF TABLES . . . . .	xiv
Chapter	Page
1. INTRODUCTION AND BACKGROUND . . . . .	1
1.1 Motivation . . . . .	1
1.2 Background . . . . .	3
1.3 Outline and contributions . . . . .	9
2. TRIPLE-DECK THEORY . . . . .	10
2.1 Background . . . . .	10
2.2 Triple-deck applications . . . . .	13
2.3 Numerical solution of triple-deck equations . . . . .	14
2.4 Results . . . . .	22
2.4.1 Comparison with previous results . . . . .	22
2.4.2 Scaled ramp angle sweep . . . . .	23
2.4.3 Curvature effects . . . . .	25
3. TWO-DIMENSIONAL NUMERICAL SOLUTIONS . . . . .	30
3.1 Geometry and mesh generation . . . . .	30
3.2 Numerical scheme . . . . .	31
3.3 Post-processing . . . . .	36
3.4 Validation . . . . .	37

3.4.1	Flat plate . . . . .	37
3.4.2	Ramp . . . . .	40
3.5	Parametric sweep . . . . .	42
3.5.1	Data reduction . . . . .	43
3.5.2	$\alpha = 8$ degrees . . . . .	44
3.5.3	$\alpha = 12$ degrees . . . . .	47
3.5.4	Correlation based on free-interaction theory . . . . .	52
3.5.5	Flow features . . . . .	56
4.	COMPARISON BETWEEN TRIPLE-DECK THEORY AND CFD . . . . .	65
4.1	Scaling of CFD results . . . . .	65
4.2	Comparison between triple-deck results and compressible Navier–Stokes results . . . . .	66
4.3	Incipient separation criterion . . . . .	67
4.4	Comparison with existing criteria . . . . .	70
5.	THREE-DIMENSIONAL NUMERICAL SOLUTIONS . . . . .	74
5.1	Mesh generation and boundary conditions . . . . .	74
5.2	Validation . . . . .	75
5.3	Numerical solution procedure . . . . .	80
5.4	Unsteady results . . . . .	80
6.	CONCLUDING REMARKS . . . . .	86
6.1	Summary . . . . .	86
6.2	Future work . . . . .	87
Appendix		
A.	Upstream influence length calculation . . . . .	88
Bibliography . . . . .		92
BIOGRAPHICAL STATEMENT . . . . .		100

## LIST OF ILLUSTRATIONS

Figure	Page
1.1 Adaptive compliant trailing edge ( <a href="http://www.nasa.gov">www.nasa.gov</a> ). . . . .	2
1.2 Unseparated interaction. . . . .	3
1.3 Separated interaction. . . . .	3
1.4 Example surface pressure for ramp-induced SBLI. . . . .	5
2.1 Triple-deck scales. . . . .	11
2.2 Example geometry used in triple-deck solutions. . . . .	16
2.3 Comparison between developed code and results of Cassel, et al [1]. . .	22
2.4 Scaled shear stress and scaled pressure distribution at a range of scaled ramp angles. . . . .	24
2.5 Scaled separation and reattachment points vs scaled ramp angle. . . .	25
2.6 Effect of increasing surface curvature on triple-deck ramp geometry. . .	26
2.7 Surface curvature effects on scaled pressure and scaled shear stress dis- tributions. . . . .	28
2.8 Scaling of separation and reattachment points for different surface cur- vature and different ramp angles. . . . .	29
3.1 Schematic of ramp geometry. . . . .	30
3.2 Ramp geometries and derivatives. . . . .	32
3.3 Example ramp mesh (every third point shown). . . . .	33
3.4 Computational domain. . . . .	36
3.5 Howarth–Dorodnitsyn compressibility transformation results. . . . .	37

3.6	Comparison between the transformed Blasius profile and FUN3D velocity profiles at different streamwise locations. . . . .	39
3.7	Stagnation and static temperature profiles at $x/\ell = 0.5$ . . . . .	39
3.8	Comparison between FUN3D and Sfeir's experimental results [2]. . . . .	40
3.9	Size of separated region versus number of nodes in the mesh. . . . .	40
3.10	Contours of Mach number at $Re_L = 140\,000$ , $M_\infty = 2.64$ and $\alpha = 11$ degrees. . . . .	42
3.11	Computational schlieren image at $Re_L = 140\,000$ , $M_\infty = 2.64$ and $\alpha = 11$ degrees. . . . .	43
3.12	Separation point as a function of Reynolds number based on displacement thickness, Mach number and radius of curvature (inches). . . . .	45
3.13	Upstream influence length as a function of Reynolds number based on displacement thickness, Mach number, and radius of curvature (inches). . . . .	45
3.14	Reattachment point as a function of Reynolds number based on displacement thickness, Mach number, and radius of curvature (inches). . . . .	46
3.15	Size of separated region as a function of Reynolds number based on displacement thickness, Mach number, and radius of curvature (inches). . . . .	46
3.16	Shape factor for $\alpha = 8$ degrees as a function of Reynolds number based on length, Mach number and radius of curvature (inches). . . . .	48
3.17	Example pressure distribution for $\alpha = 12$ degrees. . . . .	49
3.18	Separation point as a function of Reynolds number based on displacement thickness, Mach number and radius of curvature (inches). . . . .	50
3.19	Upstream influence length as a function of Reynolds number based on displacement thickness, Mach number and radius of curvature (inches). . . . .	50
3.20	Reattachment point as a function of Reynolds number based on displacement thickness, Mach number, and radius of curvature (inches). . . . .	51

3.21	Size of separated region as a function of Reynolds number based on displacement thickness, Mach number, and radius of curvature (inches).	51
3.22	Shape factor for $\alpha = 12$ degrees as a function of Reynolds number based on length, Mach number and radius of curvature (inches).	52
3.23	Free-interaction theory-based scaling of separation point as a function of Mach number and Reynolds number for $r = 0.05$ inches and different ramp angles.	54
3.24	Schematic of ramp geometric parameters.	55
3.25	Collapse of Reynolds number, Mach number and radius of curvature effects for different deflection angles.	57
3.26	Example of separated region with multiple small features ( $Re_L = 110\,000$ , $M_\infty = 2$ , $r = 4$ inches).	58
3.27	Residual convergence for $Re_L = 110\,000$ , $M_\infty = 2$ , and $r = 4$ inches.	59
3.28	Mach number effects on the separated region ( $Re_L = 200\,000$ , $r = 4$ in.).	60
3.29	Reynolds number effects on the separated region ( $M_\infty = 2$ , $r = 4$ in.).	63
3.30	Radius of curvature effects ( $Re_L = 110\,000$ , $M_\infty = 2$ ).	64
4.1	Scaled separation point as a function of scaled ramp angle from triple-deck and Navier–Stokes solutions.	66
4.2	Scaled separation point as a function of scaled ramp angle for specific case of $M_\infty = 3$ and $\alpha = 8$ degrees.	67
4.3	Optimizer convergence to incipiently separated conditions.	68
4.4	Skin friction and pressure distribution for incipiently separated conditions at $M_\infty = 3$ and $\alpha' = 8$ degrees.	69
4.5	Numerical schlieren image of incipient separation conditions ( $M_\infty = 3$ , $\alpha = 8$ degrees, $Re_L = 11\,232$ ).	70

4.6	Comparison between correlations for incipient separation based on pressure coefficient. . . . .	72
5.1	Sample three-dimensional mesh (every third point shown). . . . .	75
5.2	Schematic of mesh boundaries. . . . .	76
5.3	Surface pressure distribution comparison between 2D/3D numerical results and experimental results from Sfeir [2]. . . . .	76
5.4	Size of separated region versus number of nodes in the mesh for three-dimensional numerical solutions. . . . .	77
5.5	Slice showing contours of Mach number for Sfeir's case. . . . .	78
5.6	Residual convergence for the level 3 mesh. . . . .	79
5.7	Schematic of locations at which wall pressures were extracted. . . . .	81
5.8	Wall pressure time history at different streamwise locations at the middle of the span. . . . .	82
5.9	Isosurfaces of $Q$ -criterion colored by Mach number at different instances in time. . . . .	84
5.10	Comparison of residual convergence for steady-state numerical solutions with different Reynolds numbers. . . . .	85
A.1	Convolved signal. . . . .	90
A.2	Initial upstream influence point. . . . .	90
A.3	Sample upstream influence location. . . . .	91

## LIST OF TABLES

Table	Page
3.1 List of parameters. . . . .	43
5.1 Details of meshes used in mesh-independence study. . . . .	77

## CHAPTER 1

### INTRODUCTION AND BACKGROUND

#### 1.1 Motivation

Shock wave/boundary layer interactions (SBLIs) are one of the most complex flow phenomena because of the different types of physics involved (e.g., viscous versus inviscid) and their many side effects (e.g., boundary layer separation). At the heart of SBLIs are inviscid–viscous interactions. Due to Prandtl’s breakthrough, it is well-known that viscous effects are mostly confined to a thin region near solid surfaces in wall-bounded flows which is called the boundary layer. When a shock wave penetrates a boundary layer, the drastic increase in pressure, often termed adverse pressure gradient, encourages boundary layer thickening which may lead to separation, as indicated by negative wall shear stress. As the boundary layer thickens, it sheds compression waves into the inviscid region which will eventually coalesce into a shock wave, hence the coupling between the viscous boundary layer and the inviscid freestream. This concept will be further elaborated in later sections.

An understanding of the interactions between shock waves and boundary layers is critical in the design of high-speed flight vehicles. These interactions can be responsible for adverse effects such as boundary layer separation, localized heating, and unsteady loading. One of the side effects of boundary layer separation is poor pressure recovery, which has profound impacts on the design of wings, inlets, and turbine blades, for example. Although these interactions have been studied since the 1950s, many questions remain [3, 4]. One such question that has not been well-addressed pertains to flow separation and the effects of surface curvature. As we move



Figure 1.1: Adaptive compliant trailing edge ([www.nasa.gov](http://www.nasa.gov)).

deeper into the twenty-first century, morphing control surfaces based on compliant mechanisms are becoming a reality. These control surfaces are smooth, continuous, and flexible. See Figure 1.1 for an example of a compliant mechanism-based control surface. If these control surfaces were used on high-speed flight vehicles, they would introduce another variable to the already complex shock wave/boundary layer interactions, namely, radius of curvature. How does the radius of curvature affect the shock wave/boundary-layer interaction? Furthermore, how does radius of curvature affect the onset of separation, often termed incipient separation? These are questions this work will attempt to address.

Although morphing control surfaces represent an application for the present work, they are not the focus of the study. Rather, the focus is on fundamentally understanding how changes in surface curvature affect shock wave/boundary layer interactions.

The present study is focused on laminar SBLIs to avoid the additional uncertainty introduced by turbulence modeling. Turbulence is a complicated phenomenon by itself. There are many precedents for such a simplification which will be presented in the literature review. As such, laminar simulations were performed using a well-validated computational fluid dynamics code, FUN3D, and analytical solutions were

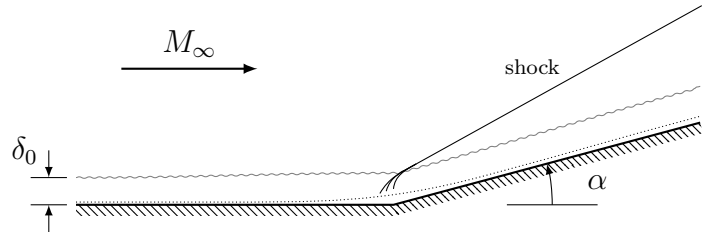


Figure 1.2: Unseparated interaction.

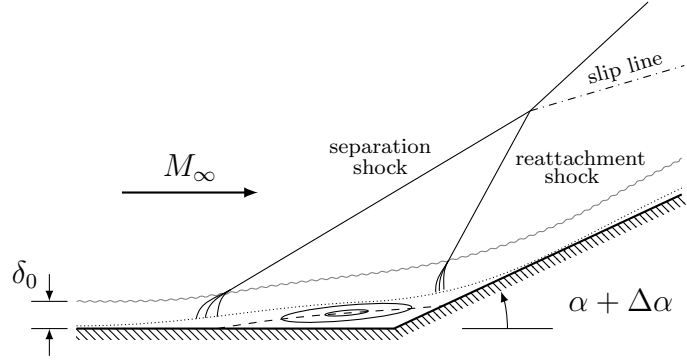


Figure 1.3: Separated interaction.

sought using triple-deck theory. The next sections provide some background on SBLIs and a literature review of related work.

1.2 Background

The essence of the incipient separation phenomenon can be described using Figures 1.2 and 1.3. The first shows an unseparated interaction. The incoming boundary layer has thickness  $\delta_0$ . The finely dotted line represents the sonic line. The flow is deflected through an angle  $\alpha$ , resulting in the formation of an oblique shock wave. The adverse pressure gradient causes some boundary layer thickening, but is not strong enough to cause the boundary layer to separate in this case. Figure 1.3 shows the case in which the flow deflection angle is incremented by a small angle,  $\Delta\alpha$ , which increases the strength of the shock enough to result in the separation of the boundary layer. A recirculation region, also known as a separation bubble, is

present near the corner. Moving from left to right, the first feature is the separation shock which is caused by the flow deflection due to the separation bubble. Below the dotted line, the flow is subsonic. The dashed line represents a line of zero velocity. The beginning and end of this dashed line represent separation and reattachment, respectively. Further downstream, the next shock is caused again by turning the flow, this time due to reattachment. Compression waves can be seen coalescing into the reattachment shock wave. High localized heating can occur in the reattachment region due to the slow velocity of the flow presenting nearly stagnant conditions. The flow can be considered incipiently separated when it exists between the two states shown in Figures 1.2 and 1.3. More explicitly, incipient separation can be described as a situation in which the flow is on the verge of separation.

Early in shock wave/boundary layer interaction research, it was thought that incipient separation is sudden – a bifurcation. Settles performed experiments of compression corner configurations, from which he found that separation was gradual, rather than abrupt [5]. He suggested that incipient separation should be classified not based on whether or not a separation bubble exists, but rather based on the size of the separated region. The review by Détery and Marvin further classifies incipient separation as true incipient separation and effective incipient separation [6]. They regard true incipient separation to be of academic interest, and effective incipient separation as the case where the effects of the separation begin to have practical consequences. This background on incipient separation is useful to set the stage for later discussion.

In early SBLI research, one focus was providing an explanation for upstream influence. The upstream influence length,  $L_0$ , is shown schematically in Figure 1.4, using the surface pressure distribution as an indicator. It is defined as the distance between the point where pressure rise due to the shock wave begins and the location

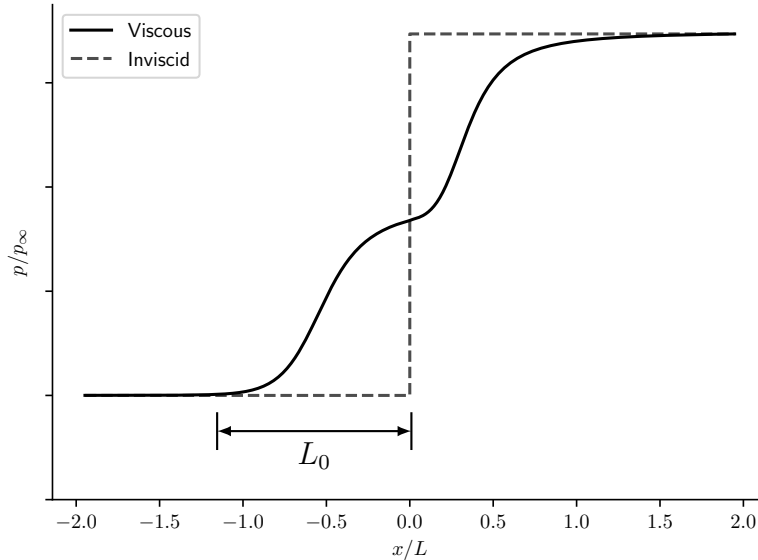


Figure 1.4: Example surface pressure for ramp-induced SBLI.

where the shock would impinge if the flow were inviscid [7]. The upstream influence length can be thought of as the distance that viscous effects spread the pressure rise in the upstream direction. Without viscous effects, the pressure rise is discontinuous, as shown by the dashed line in Figure 1.4.

The nature of the governing equations is now considered to further elucidate the mechanism responsible for upstream influence. The inviscid, freestream flow outside of the boundary layer is governed by the Euler equations, which are hyperbolic, while the boundary layer equations are parabolic [8]. The goal was to explain how the viscous solution could affect the pressure upstream when the types of the governing equations indicated that information could not propagate upstream. It was suggested by some that disturbances were propagating upstream from a separated region to create the upstream influence. However, it was shown that the subsequent streamwise scale was too small [9]. Furthermore, upstream influence is still present in flows with unseparated boundary layers.

The traditional approach to boundary layer analysis involves partitioning the flow into two different regions: the inviscid freestream and the boundary layer. The inviscid solution is used to find the pressure which is imposed on the boundary layer. This approach works well for flows with attached boundary layers. In the case of boundary layer separation, a singularity arises in the boundary layer equations, known as the Goldstein singularity [10]. This singularity prevented theoretical studies of separated flows until Lighthill's groundbreaking work [9, 11].

Lighthill surveyed a large amount of experimental data and developed a theoretical approach for describing boundary layer separation. He suggested separating the flow into three regions or decks.<sup>1</sup> Lighthill's approach, which was generalized by Stewartson and Williams, allows for theoretical study of separated boundary layers [8].

More specifically, Lighthill discussed two mechanisms for upstream influence [9, 11, 12]. The first proposed mechanism suggests that when a boundary layer is subjected to some disturbance which creates an adverse pressure gradient, the boundary layer thickness increases, which causes compression waves to be shed into the freestream which in turn creates an adverse pressure gradient further upstream. The second mechanism pertains to the spreading of the separation bubble. Assuming a large enough pressure gradient exists, the boundary layer will separate. The separated region will then affect the external flow. That is, the displacement thickness will grow, which then causes deflection of streamlines and an adverse pressure gradient further upstream. The separated region continues to grow in this manner until the adverse pressure gradient induced upstream is not enough to cause further separation. According to Lighthill, the first mechanism is unique to supersonic flow, while the second is present in subsonic and supersonic flows. In his second paper,

---

<sup>1</sup>More about this approach will be explained in Chapter 2.

Lighthill used an analytical approach to study the second mechanism in more detail [11].

Chapman, et al., performed experiments of several different configurations, such as ramps and impinging shocks, over a large range of Mach numbers and Reynolds numbers with the goal of developing a better understanding of flow separation and upstream influence ( $0.4 \leq M_\infty \leq 3.6$  and  $4\,000 \leq Re \leq 5\,000\,000$ ) [13]. An important result of their study was the development of free interaction theory which suggested that the upstream part of the interaction is independent of downstream events or disturbances. The theory allowed for a prediction of the pressure in the separated region which closely matches experimental results. The free interaction concept is important for this dissertation because the results in Chapter 3 will be discussed in terms of free interaction.

Although much work has been done in laminar, two-dimensional SBLIs, and some would consider the physics to be well-understood, it is believed that further physical understanding can be gained by examining these simplified configurations. A recent study that focused on two-dimensional, laminar SBLIs is that of Sansica, et al., who used a laminar, impinging shock configuration in an effort to better understand the source of unsteadiness in turbulent SBLIs [14]. Smith and Khorrami developed a new numerical scheme for solving the triple-deck equations and suggested that there was some critical ramp angle beyond which singularities arise [15]. Korolev, et al., used two numerical schemes to solve the triple-deck equations and showed that additional eddies form inside the separation bubble [16]. They also showed that the singularity discussed by Smith and Khorrami was not present in their solutions. As such, it can be argued that the singularity was due to the numerical method used to solve the triple-deck equations rather than the equations themselves.

Inger investigated the effects of curvature on streamlines and the subsequent production of Görtler vortices in supersonic SBLIs by a modification of Oswatitsch's expression of streamline curvature [17]. Inger also examined curvature effects in turbulent, transonic flows via triple-deck theory and found that increasing convex surface curvature increases the size of the interaction [18]. Additionally, he found that modifications to the surface curvature are capable of postponing the onset of separation to a small degree.

Some early experimental work by Sturek and Danberg focused on turbulent interactions over an isentropic compression ramp [19, 20]. It seems the motivation of the study was to produce reliable turbulence data in the mean sense. Donovan, et al., used a single curved ramp geometry to experimentally examine the effects of surface curvature on the large-scale turbulent structures in a turbulent, supersonic SBLI [21]. Wang used analysis and experiments to study mixing layers subjected to curvature with the emphasis being on turbulence [22].

This review of the literature reveals that there is no systematic study which adequately quantifies the effects of curvature on laminar or turbulent SBLIs. Much of the previous experimental and computational work has been focused on only a few configurations and flow conditions. The previous theoretical work concentrated on streamline curvature in the supersonic regime and surface curvature in the transonic regime. All this points to the fact that the effects of curvature on laminar, supersonic shock wave/boundary layer interactions have not been studied in depth. As such, there is still room for contributions. A better understanding of the physics of laminar SBLIs may open up new ways to attack the more complicated turbulent SBLIs. We now move to a discussion of the methods used to obtain results.

### 1.3 Outline and contributions

The present study of curvature effects in laminar shock wave/boundary layer interactions is approached using theory and numerics. For the sake of simplicity, two-dimensional interactions are considered first, followed by three-dimensional, unsteady numerical solutions to the Navier–Stokes equations. In chapter 2, triple-deck theory will be introduced and numerical results will be presented. Chapter 3 presents the numerical method used to compute solutions to the compressible Navier–Stokes equations along with results. Chapter 4 consists of a novel comparison between supersonic triple-deck theory and development of a new correlation for incipient separation. Chapter 5 focuses on three-dimensional, unsteady numerical simulations of the compressible Navier–Stokes equations.

In a broad sense, the contribution of the present work is a systematic study of laminar, compression ramp-induced shock wave/boundary layer interactions. More specifically, the individual contributions are: (1) a novel comparison between triple-deck theory and CFD, (2) a free-interaction theory-based correlation for the scaling of the separation bubble, (3) a new scaling relationship involving Reynolds number, Mach number and radius of curvature, and (4) a criterion for incipient separation which was developed using CFD results and triple-deck scalings.

## CHAPTER 2

### TRIPLE-DECK THEORY

Triple-deck theory represents a simplification of the Navier–Stokes equations. This simplification is achieved using knowledge of the physics and asymptotic theory. In pursuit of an explanation of the upstream influence present in SBLIs, Lighthill laid the groundwork for triple-deck theory via a linearized solution [9, 11]. Stewartson and Williams, and Neiland independently formalized the theory and presented numerical solutions to the nonlinear triple-deck equations [8, 23]. In the present section, some background on the underpinnings of triple-deck theory will be provided and the numerical method used to obtain solutions will be explained. The chapter will conclude with results.

#### 2.1 Background

The derivation of the simplified form of the governing equations assumes an initially undisturbed incoming flow, i.e., a transformed Blasius profile, into which a disturbance is introduced. The boundary layer is then divided into three main regions, or decks. Simplifying assumptions based on knowledge of the flow physics are then made. The solution in each deck is then sought with matching at the interfaces accomplished via the method of matched asymptotic expansions (MMAE) [24]. For a comprehensive view of asymptotic methods, see reference 25.

Considering the flow over the flat plate portion of a ramp, upstream of the compression corner, the solution is given by a compressibility transformation, such as the Howarth–Dorodnitsyn transformation. Introducing a small disturbance in the

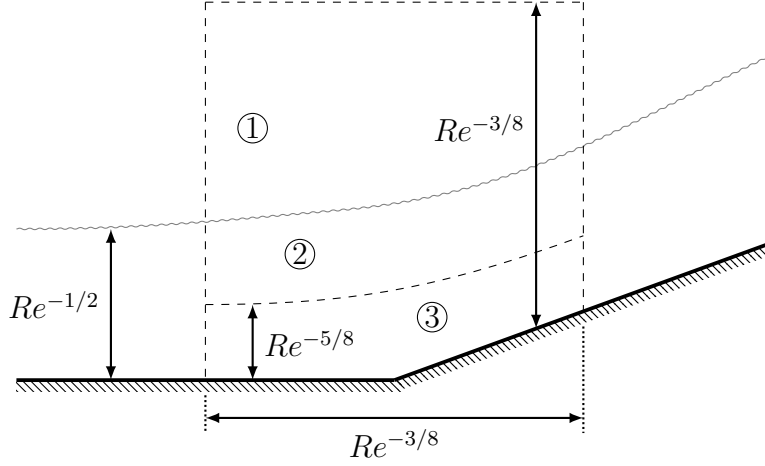


Figure 2.1: Triple-deck scales.

incoming profile,  $\epsilon$ , which could be due to interaction with the freestream, we may write the solution in terms of asymptotic expansions as

$$u(X, Y) = U_0(Y) + \sum_{n=1}^{\infty} \epsilon^n u_n(X, Y), \quad (2.1a)$$

$$v(X, Y) = V_0(Y) + \sum_{n=1}^{\infty} \epsilon^n v_n(X, Y), \quad (2.1b)$$

$$p(X, Y) = p_{\infty} + \sum_{n=1}^{\infty} \epsilon^n p_n(X, Y), \quad (2.1c)$$

$$\rho(X, Y) = \rho_0(Y) + \sum_{n=1}^{\infty} \epsilon^n \rho_n(X, Y), \quad (2.1d)$$

where  $X$  and  $Y$  are new coordinates which are defined so that they are  $\mathcal{O}(1)$  in the boundary layer and terms with subscript 0 denote the undisturbed flow.

The resulting triple-deck structure is shown in Figure 2.1. The streamwise extent of the interaction is  $\mathcal{O}(Re^{-3/8})$  [8]. Region 1 represents the inviscid freestream. Inserting asymptotic expansions in terms of some small parameter  $\epsilon$  into the Navier–Stokes equations and keeping terms of order  $\epsilon$  while neglecting viscosity reveals that

the governing equation in this region is the Prandtl–Glauert equation, which is given by

$$(1 - M_\infty^2) \frac{\partial^2 p_2}{\partial X^2} + \frac{\partial^2 p_2}{\partial Y^2} = 0. \quad (2.2)$$

Region 2 is the middle deck, where inserting a similar asymptotic expansion into the Navier–Stokes and simplifying shows that the flow in this deck is inviscid, but rotational. As such, the main effect of the middle deck is to transmit disturbances from the lower deck to the upper deck via streamline divergence. This streamline divergence is defined via a pressure-deflection relationship. For a supersonic flow, this relationship is given by the Ackeret formula [26]:

$$p = -\frac{\partial A}{\partial x} + \frac{\partial f}{\partial x}, \quad (2.3)$$

where  $A(x)$  is the displacement thickness and  $f(x)$  is the surface geometry.

Region 3 is the lower deck. Stewartson derives the equations for the lower deck by enforcing the no-slip condition, as well as imposing the undisturbed profile<sup>1</sup> at the beginning of the interaction region. New scaled variables are then introduced to simplify the final form of the governing equations. For all the details, see Stewartson and Williams original paper [8]. After much effort, the following result is achieved:

$$\frac{\partial u}{\partial x} + \frac{\partial v}{\partial y} = 0, \quad (2.4a)$$

$$\frac{\partial u}{\partial t} + u \frac{\partial u}{\partial x} + v \frac{\partial u}{\partial y} = -\frac{\partial p}{\partial x} + \frac{\partial^2 u}{\partial y^2}, \quad (2.4b)$$

which are subject to

$$u|_{y=0} = v|_{y=0} = 0, \quad \lim_{y \rightarrow \infty} u = y + A + \dots, \quad \lim_{x \rightarrow -\infty} u = y. \quad (2.5)$$

---

<sup>1</sup>The Blasius profile with an appropriate compressibility transformation is imposed at the beginning of the interaction.

The equations given in (2.4) are the conventional incompressible boundary layer equations in nondimensional form, subject to unconventional boundary conditions which come about due to matching requirements and an undisturbed initial profile.

The goal is to solve the equations in each deck and match the solutions. An exact solution to the Prandtl–Glauert equation (2.2) is known [8]. In the middle deck, Ackeret’s equation gives a relationship between the pressure, displacement thickness and surface geometry. However, the pressure and displacement thickness are not known. They must be determined by solving (2.4). Treating the pressure and displacement thickness as unknowns in this way avoids the singularity described by Goldstein [10].

Because of the nonlinear convective terms in (2.4), approximate solutions have been sought using perturbation methods and numerical methods. Myriad numerical solution approaches have been proposed over the years which have been partly documented in chapter seven of the text by Sychev et al. [26]. The given equations can be challenging to solve because (1) they are nonlinear, (2) the pressure and displacement thickness are not known, and (3) boundary conditions must be enforced at  $\pm\infty$ . Now, a few example applications of triple-deck theory are discussed and the numerical scheme used in the present work is explained.

## 2.2 Triple-deck applications

The literature on triple-deck theory is rich and diverse. Triple-deck theory has been applied to study laminar and turbulent flows in subsonic, transonic, supersonic and hypersonic speed regimes. For some examples, see [18, 27, 28, 29, 30]. Modifications have been made to the theory to account for nonadiabatic walls [31]. The theory has also been extended for the purposes of stability analysis by Smith, with some recent work on supersonic stability analysis undertaken by Ryzhov [32, 33].

### 2.3 Numerical solution of triple-deck equations

The nonlinear triple-deck equations given by (2.4) must now be solved. Due to the nonlinearity, a numerical solution is undertaken. Specifically, a numerical method developed by Ruban was implemented using the C++ language [34]. The numerical method will now be described.

The scalings used in the lower deck are as follows

$$\tilde{x} = \rho_w^{-1/2} \mu_w^{-1/4} \lambda^{-5/4} \beta^{-3/4} Re_0^{-3/8} x, \quad (2.6a)$$

$$\tilde{y} = \rho_w^{-1/2} \mu_w^{1/4} \lambda^{-3/4} \beta^{-1/4} Re_0^{-5/8} (y - f(x)), \quad (2.6b)$$

$$\tilde{u} = \rho_w^{-1/2} \mu_w^{1/4} \lambda^{1/4} \beta^{-1/4} Re_0^{-1/8} u, \quad (2.6c)$$

$$\tilde{v} = \rho_w^{-1/2} \mu_w^{3/4} \lambda^{3/4} \beta^{1/4} Re_0^{-3/8} (v - df/dx), \quad (2.6d)$$

$$\tilde{p} - 1 = \lambda^{1/2} \mu_w^{1/2} \beta^{-1/2} Re_0^{-1/4} p, \quad (2.6e)$$

$$\tilde{t} = \lambda^{-3/2} \mu_w^{-1/2} \beta^{-1/2} Re_0^{-1/4} t, \quad (2.6f)$$

where the subscript  $w$  denotes properties at the wall,  $\lambda = 0.332$ ,  $\beta = (M_\infty^2 - 1)^{1/2}$ ,  $f(x)$  is the surface geometry<sup>2</sup> and

$$Re_0 = \frac{\rho_\infty U_\infty L}{\mu_0}, \quad (2.7)$$

where  $\mu_0$  is the dynamic viscosity evaluated at a reference enthalpy of  $U_\infty^2$ . A Prandtl transposition is incorporated in the scalings (that is,  $f(x)$  and  $df/dx$  in (2.6)). The scaled ramp angle is given by

$$\tilde{\alpha} = \lambda^{1/2} \mu_w^{1/2} \beta^{1/2} Re_0^{-1/4} \alpha. \quad (2.8)$$

It should be noted that all ( $\tilde{\cdot}$ ) variables are dimensionless with respect to  $L$ ,  $U_\infty$ ,  $\rho_\infty U_\infty^2$ ,  $\rho_\infty$ ,  $U_\infty^2$ , and  $\mu_0$ .

---

<sup>2</sup>The surface geometry has been incorporated in the scalings and thus in the triple-deck equations via a Prandtl transposition.

Beyond the Prandtl transposition, an additional coordinate transformation is introduced so that the computational plane is defined by  $\hat{x} \in [-1, 1]$  and  $\hat{y} \in [0, 1]$ . The transformation is

$$\hat{x} = \frac{2}{\pi} \tan^{-1} \left( \frac{x}{a} \right), \quad (2.9a)$$

$$\hat{y} = \frac{2}{\pi} \tan^{-1} \left( \frac{y}{b} \right), \quad (2.9b)$$

where  $a$  and  $b$  are constants which can be used to control the clustering of the mesh toward the corner. This transformation eliminates the need to enforce boundary conditions at  $\pm\infty$ . Results will be presented in Chapter 3.

It should be noted that the surface definition used in the triple-deck solutions is

$$f(x) = \frac{\alpha}{2} \left( x + \sqrt{x^2 + r^2} \right), \quad (2.10)$$

rather than the typical compression ramp geometry:

$$f(x) = \begin{cases} 0, & x < 0, \\ \alpha, & x \geq 0. \end{cases} \quad (2.11)$$

The reason for using (2.10) is because the formulation is dependent upon the second derivative,  $d^2f/dx^2$ . The typical compression ramp geometry has a discontinuity in slope. The surface definition given in (2.10) is at least  $C^2$  continuous. Additional solutions were attempted with the  $C^1$  continuous geometry which was used for the CFD work, but the numerical scheme did not converge. See Figure 2.2 for a plot of (2.10) at  $\alpha = 3$ , and  $r = 5$ .

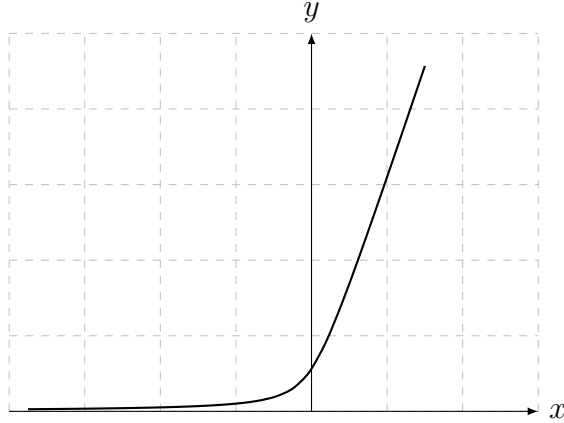


Figure 2.2: Example geometry used in triple-deck solutions.

For reasons that will be evident later, the triple-deck equations, (2.4), are recast in terms of the stream function,  $\psi$ , and scaled shear stress,  $\tau$ , where

$$u = \frac{\partial \psi}{\partial y} \tag{2.12a}$$

$$v = -\frac{\partial \psi}{\partial x} \tag{2.12b}$$

$$\tau = \frac{\partial u}{\partial y} \tag{2.12c}$$

The result is

$$\frac{\partial \tau}{\partial t} + u \frac{\partial \tau}{\partial x} + v \frac{\partial \tau}{\partial y} = \frac{\partial^2 \tau}{\partial y^2} \tag{2.13}$$

Using (2.12),  $\psi$  and  $\tau$  can be related as follows:

$$\tau = \frac{\partial^2 \psi}{\partial y^2} \tag{2.14}$$

It should be noted that the present formulation makes use of the unsteady form of the triple-deck equations. The strategy is to start with an initial guess for the solution and to march in time until convergence is achieved.

The boundary conditions are given by (2.5), and are repeated here:

$$u|_{y=0} = v|_{y=0} = 0, \quad \lim_{y \rightarrow \infty} u = y + A + \dots, \quad \lim_{x \rightarrow -\infty} u = y \tag{2.15}$$

Inserting (2.12) yields

$$\psi|_{y=0} = \frac{\partial\psi}{\partial y}\Big|_{y=0} = 0, \quad \lim_{x \rightarrow -\infty} \tau = 1, \quad \lim_{x \rightarrow \infty} \tau = 1, \quad \lim_{y \rightarrow \infty} \tau = 1 \quad (2.16)$$

The displacement function,  $A$ , which is unknown, is no longer present in the boundary conditions.

The attentive reader will notice that the boundary conditions must be enforced in the limit as  $(x, y) \rightarrow (\pm\infty, \infty)$ . Many previous studies have enforced these boundary conditions approximately by generating a large computational domain. Introducing the transformations given by (2.9) so that boundary conditions can be enforced at  $(\hat{x}, \hat{y}) \rightarrow (\pm 1, 1)$ ,

$$\frac{\partial\tau}{\partial t} + u \frac{\Gamma(\hat{x})}{a} \frac{\partial\tau}{\partial \hat{x}} + v \frac{\Gamma(\hat{y})}{b} \frac{\partial\tau}{\partial \hat{y}} = \frac{\Gamma(\hat{y})}{b} \frac{\Gamma'(\hat{y})}{b} \frac{\partial\tau}{\partial \hat{y}} + \frac{\Gamma^2(\hat{y})}{b^2} \frac{\partial^2\tau}{\partial \hat{y}^2} \quad (2.17a)$$

$$\frac{\Gamma(\hat{y})}{b} \frac{\partial}{\partial \hat{y}} \left( \frac{\Gamma(\hat{y})}{b} \frac{\partial\psi}{\partial \hat{y}} \right) = \tau \quad (2.17b)$$

where the function  $\Gamma(x)$  is given by

$$\Gamma(x) = \frac{1 + \cos(\pi x)}{\pi} \quad (2.18)$$

The interaction law can be written as

$$\frac{\Gamma(0)}{b} \frac{\partial\tau}{\partial \hat{y}}\Big|_{\hat{y}=0} = -\frac{\Gamma(\hat{x})\Gamma'(\hat{x})}{a^2} \frac{\partial\varphi}{\partial \hat{x}} - \frac{\Gamma^2(\hat{x})}{a^2} \frac{\partial^2\varphi}{\partial \hat{x}^2} + \frac{\partial^2 f}{\partial x^2} \quad (2.19)$$

where

$$\varphi = b \int_0^1 \frac{\tau - 1}{\Gamma(\hat{y})} d\hat{y} \quad (2.20)$$

Lastly, the relationship between the velocity components and the stream function becomes

$$u = \frac{\Gamma(\hat{y})}{b} \frac{\partial\psi}{\partial \hat{y}}, \quad v = -\frac{\Gamma(\hat{x})}{a} \frac{\partial\psi}{\partial \hat{x}} \quad (2.21)$$

Now, the goal is to numerically solve the momentum equation, given by (2.17a), subject to (2.16) and (2.19).

The domain in the streamwise direction is truncated at some finite value,  $\hat{y}_{\max}$ , in order to satisfy the boundary condition  $u \sim y$  as  $y$  approaches infinity. A uniform mesh over  $\hat{x} \in [-1, 1]$ ,  $\hat{y} \in [0, \hat{y}_{\max}]$  must be supplied by the user.

Equation (2.17a) is now discretized using finite differences with second-order spatial accuracy and first-order temporal accuracy. Doing so yields

$$\begin{aligned} \frac{\tau_{i,j}^n - \tau_{i,j}^{n-1}}{\Delta t} + \frac{\Gamma(\hat{x}_i)}{a} \left[ u \frac{\partial \tau}{\partial \hat{x}} \right]_{i,j}^{n-1} + \frac{\Gamma(\hat{y}_j)}{b} v_{i,j}^{n-1} \left( \frac{\tau_{i,j+1}^n - \tau_{i,j-1}^n}{2\Delta \hat{y}} \right) = \\ \frac{\Gamma(\hat{y}_j)\Gamma'(\hat{y}_j)}{b^2} \left( \frac{\tau_{i,j+1}^n - \tau_{i,j-1}^n}{2\Delta \hat{y}} \right) + \frac{\Gamma^2(\hat{y}_j)}{b^2} \left( \frac{\tau_{i,j+1}^n - 2\tau_{i,j}^n + \tau_{i,j-1}^n}{(\Delta \hat{y})^2} \right) \end{aligned} \quad (2.22)$$

The streamwise convective term is evaluated at the previous timestep because of how it must be computed in reversed flow (i.e., upwinding vs downwinding). If the flow is not reversed, upwind differencing is used. Otherwise, the direction is reversed. That is,

$$\left[ u \frac{\partial \tau}{\partial \hat{x}} \right]_{i,j}^{n-1} = \begin{cases} u_{i,j}^{n-1} \frac{3\tau_{i,j}^{n-1} - 4\tau_{i-1,j}^{n-1} + \tau_{i-2,j}^{n-1}}{2\Delta \hat{x}}, & \text{for } u_{i,j}^{n-1} \geq 0 \\ -u_{i,j}^{n-1} \frac{3\tau_{i,j}^{n-1} - 4\tau_{i+1,j}^{n-1} + \tau_{i+2,j}^{n-1}}{2\Delta \hat{x}}, & \text{for } u_{i,j}^{n-1} < 0 \end{cases} \quad (2.23)$$

According to Cassel, et al., this method for handling separated flow should yield better results than previous methods which set the streamwise convective term to zero for reversed flow [1]. Terms which involve the velocities are calculated at the previous timestep, denoted  $n - 1$ , in order to avoid having to deal with the nonlinearity via an iterative method.

Solving the system of equations in (2.22) yields  $\tau_{i,j}^n$  at each node. The tridiagonal problem may be stated as

$$c_j^- \tau_{i,j-1}^n + c_j \tau_{i,j}^n + c_j^+ \tau_{i,j+1}^n = d_j \quad (2.24)$$

where

$$c_j = -2A - \frac{1}{\Delta t} \quad (2.25a)$$

$$c_j^- = A - \frac{\Gamma(\hat{y}_j)}{2b\Delta\hat{y}} \left( \frac{\Gamma'(\hat{y}_j)}{b} - v_{i,j}^{n-1} \right) \quad (2.25b)$$

$$c_j^+ = 2A - c_j^- \quad (2.25c)$$

$$d_j = \frac{\Gamma(\hat{x}_i)}{a} \left[ u \frac{\partial \tau}{\partial \hat{x}} \right]_{i,j}^{n-1} - \frac{\tau_{i,j}^n - 1}{\Delta t} \quad (2.25d)$$

$$A = \frac{\Gamma^2(\hat{y}_j)}{(b\Delta\hat{y})^2} \quad (2.25e)$$

Equations (2.25) may be manipulated into the following form

$$\tau_{i,j}^n = R_j \tau_{i,j-1}^n + Q_j \quad \text{for } j = 2, \dots, J \quad (2.26)$$

where  $I$  and  $J$  are the number of points in the streamwise and normal directions, respectively. To satisfy the boundary conditions,  $R_J = 0$  and  $Q_J = 1$ . Also,

$$R_j = -\frac{c_j^-}{c_j + c_j^+ R_{j+1}} \quad (2.27a)$$

$$Q_j = -\frac{c_j^+ Q_{j+1} - d_j}{c_j + c_j^+ R_{j+1}} \quad (2.27b)$$

which are evaluated from  $j = J - 1$  to  $j = 2$ . Examining (2.26) shows that  $\tau_{i,j}$  can be found as long as  $\tau_{i,j-1}$  is known. Thus, as long as  $\tau_{i,1}$  is known, the above equations may be used to find the solution at all the other points. Using this knowledge and manipulating the above equations,

$$\tau_{i,j} = C_{i,j} \tau_{i,1} + B_{i,j} \quad \text{for } j = 1, \dots, J \quad (2.28)$$

with  $C_{i,1} = 1$  and  $B_{i,1} = 0$ . Furthermore,

$$C_{i,j} = R_j C_{i,j-1} \quad (2.29a)$$

$$B_{i,j} = R_j B_{i,j-1} + Q_j \quad (2.29b)$$

which are evaluated for  $j = 2, \dots, J$ . If the shear stress at the wall,  $\tau_{i,1}$ , can be found, the momentum equation may be solved for the shear stress at all the remaining points using the formulation above.

The objective now is to come up with a way to find  $\tau_{i,1}$ . The integral in the interaction law may be represented approximately using the trapezoidal rule:

$$\varphi = b \int_0^{\hat{y}_{\max}} \frac{\tau - 1}{\Gamma(\hat{y})} d\hat{y} \approx \frac{\Delta\hat{y}}{2} \sum_{j=2}^J \left[ \frac{b}{\Gamma(\hat{y}_j)} (\tau_{i,j} - 1) + \frac{b}{\Gamma(\hat{y}_{j-1})} (\tau_{i,j-1} - 1) \right] \quad (2.30)$$

Using (2.29) in (2.30) yields

$$\varphi = N_i \tau_{i,1} + M_i \quad (2.31)$$

where

$$N_i = \frac{\Delta\hat{y}}{2} \sum_{j=2}^J \left[ \frac{b}{\Gamma(\hat{y}_j)} C_{i,j} + \frac{b}{\Gamma(\hat{y}_{j-1})} C_{i,j-1} \right] \quad (2.32a)$$

$$M_i = \frac{\Delta\hat{y}}{2} \sum_{j=2}^J \left[ \frac{b}{\Gamma(\hat{y}_j)} (B_{i,j} - 1) + \frac{b}{\Gamma(\hat{y}_{j-1})} (B_{i,j-1} - 1) \right] \quad (2.32b)$$

The normal derivative of the shear stress on the left hand side of the interaction law is now written using second-order accurate forward differences as follows:

$$\left. \frac{\partial \tau}{\partial \hat{y}} \right|_{\hat{y}=0} = \frac{4C_{i,2} - 3 - C_{i,3}}{2\Delta\hat{y}} \tau_{i,1} + \frac{4B_{i,2} - B_{i,3}}{2\Delta\hat{y}} \quad (2.33)$$

Now, a tridiagonal system for the wall shear stress may be formed:

$$\bar{c}_i^- \tau_{i-1,1} + \bar{c}_i \tau_{i,1} + \bar{c}_i^+ \tau_{i+1,1} = \bar{d}_i \quad \text{for } i = 2, \dots, I-1 \quad (2.34)$$

with

$$\bar{c}_i = \frac{\Gamma^2(\hat{x}_i)}{a^2} \frac{2N_i}{(\Delta\hat{x})^2} - \frac{\Gamma(0)}{b} \left( \frac{4C_{i,2} - 3 - C_{i,3}}{2\Delta\hat{y}} \right) \quad (2.35a)$$

$$\bar{c}_i^- = -\frac{\Gamma^2(\hat{x}_i)}{a^2} \frac{N_{i-1}}{(\Delta\hat{x})^2} + \frac{\Gamma(\hat{x}_i)\Gamma'(\hat{x}_i)}{a^2} \frac{N_{i-1}}{2\Delta\hat{x}} \quad (2.35b)$$

$$\bar{c}_i^+ = -\frac{\Gamma^2(\hat{x}_i)}{a^2} \frac{N_{i+1}}{(\Delta\hat{x})^2} - \frac{\Gamma(\hat{x}_i)\Gamma'(\hat{x}_i)}{a^2} \frac{N_{i+1}}{2\Delta\hat{x}} \quad (2.35c)$$

$$\bar{d}_i = \frac{\Gamma^2(\hat{x}_i)}{a^2} \left( \frac{M_{i+1} - 2M_i + M_{i-1}}{(\Delta\hat{x})^2} \right) + \frac{\Gamma(\hat{x}_i)\Gamma'(\hat{x}_i)}{a^2} \left( \frac{M_{i+1} - M_{i-1}}{2\Delta\hat{x}} \right) - \frac{d^2f}{dx^2} \Big|_{x=x_i} \quad (2.35d)$$

$$+ \frac{\Gamma(0)}{b} \left( \frac{4B_{i,2} - B_{i,3}}{2\Delta\hat{y}} \right)$$

The tridiagonal system of equations may be solved for the wall shear stress using Thomas algorithm. After the wall shear stress is known, the shear stress at all the other points is computed using (2.28). Now, assuming that  $\tau$  has been computed at each point, the streamwise velocity,  $u$ , and the stream function may be computed via integration:

$$u = b \int_0^{\hat{y}} \frac{\tau}{\Gamma(\hat{y})} d\hat{y} \quad (2.36a)$$

$$\psi = b \int_0^{\hat{y}} \frac{u}{\Gamma(\hat{y})} d\hat{y} \quad (2.36b)$$

This integration was accomplished using the trapezoidal rule. The normal velocity component,  $v$ , may be computed from the stream function, using second-order accurate finite differences as follows:

$$v_{i,j} = \frac{-\Gamma(\hat{x}_i)}{a} \frac{\psi_{i+1,j} - \psi_{i-1,j}}{2\Delta\hat{x}} \quad (2.37)$$

Information about pressure is not included in the above formulation, but it can be computed as a post-processing step. This is accomplished using the following equation which comes from the interaction law:

$$p_i = \frac{df}{dx} \Big|_{x=x_i} - \frac{\Gamma(\hat{x}_i)}{a} \left( \frac{N_{i+1}\tau_{i+1,1} + M_{i+1} - N_{i-1}\tau_{i-1,1} - M_{i-1}}{2\Delta\hat{x}} \right) \quad (2.38)$$

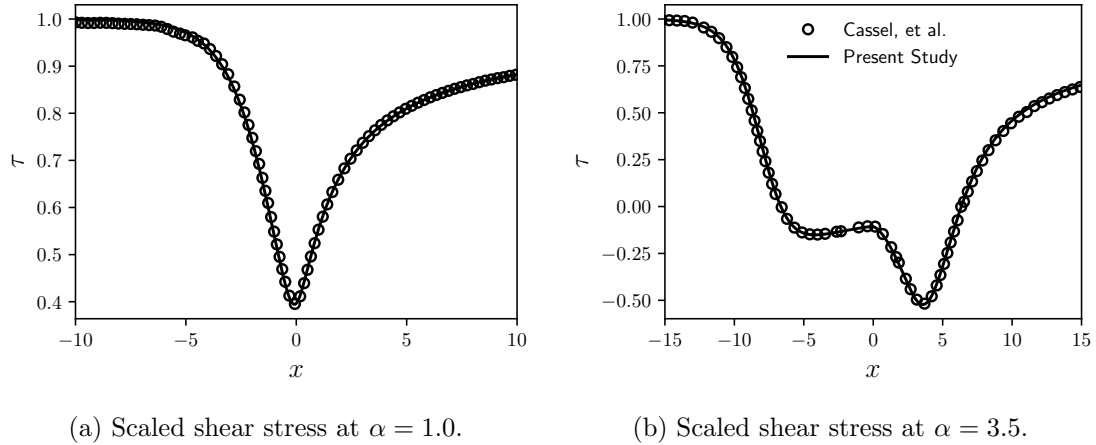


Figure 2.3: Comparison between developed code and results of Cassel, et al [1].

The algorithm described above was implemented in the C++ language. The convergence criterion used was based on the  $L^2$  norm of the difference between the wall shear stress at the current time and at the previous time step. That is,

$$\mathcal{E} = \sqrt{\sum_i (\tau_{i,1}^n - \tau_{i,1}^{n-1})^2} \quad (2.39)$$

The code was run until the change in the wall shear stress fell below a prespecified tolerance of  $1 \times 10^{-6}$ .

## 2.4 Results

Results will now be presented in terms of the scaled wall shear stress and scaled pressure. The results from the developed code will be compared against the results of Cassel, et al., after which curvature effects will be investigated.

### 2.4.1 Comparison with previous results

To ensure that the developed code was correct, the scaled shear stress distributions at scaled ramp angles of 1.0 and 3.5 are compared against the results of Cassel,

et al. [1]. Figure 2.3 shows that the present results match those of Cassel, et al. very closely. This result serves as validation that the code was developed correctly.

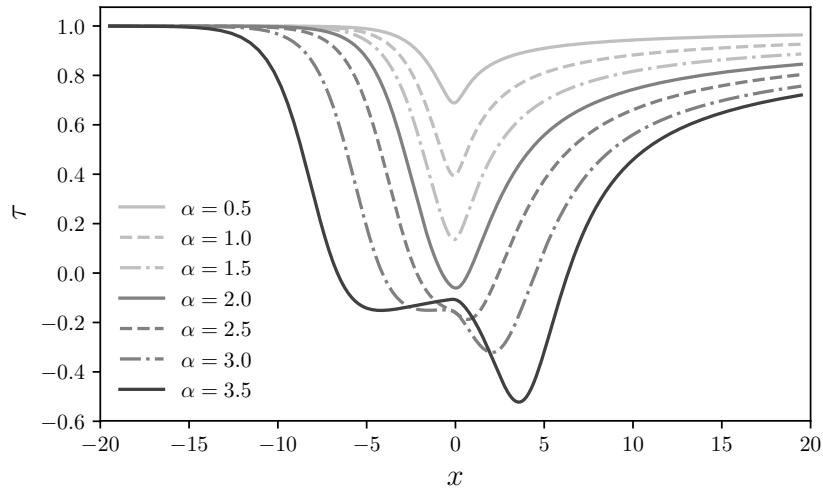
#### 2.4.2 Scaled ramp angle sweep

Results are now presented for several values of the scaled ramp angle ranging from 0.5 to 3.5. The computations were performed by restarting solutions from the preceding ramp angle thereby allowing for faster convergence. The results are depicted in Figure 2.4. Figure 2.4(b) shows the emergence of the pressure plateau as the scaled ramp angle increases which is typical of ramp-induced shock wave/boundary layer interactions. Figure 2.4(a) shows the variation of the scaled wall shear stress as a function of the scaled ramp angle. At scaled ramp angles of 2 and greater, negative wall shear stress indicates boundary layer separation and reversed flow. An iterative approach was used to find the scaled deflection angle required for incipient separation. The function which was minimized to find the scaled ramp angle is as follows:

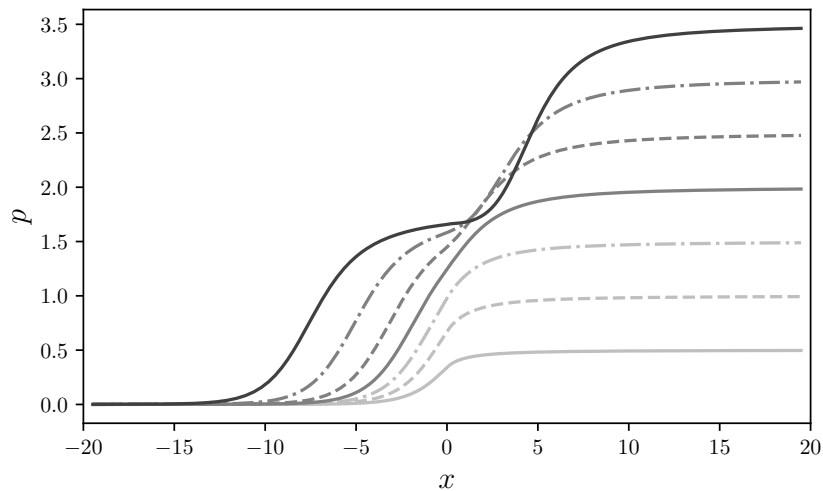
$$\min |\tau(\alpha)| = 0 \tag{2.40}$$

Minimizing the above function using optimization results in  $\alpha_{is} = 1.8226$ .

The separation and reattachment points for various scaled ramp angles were calculated by finding the locations where the scaled wall shear stress underwent a sign change. The result is shown in Figure 2.5. The corner is located at  $x = 0$ . Interestingly, the reattachment point exhibits a linear trend with decreasing scaled ramp angle. The same can be said for the separation point below a scaled ramp angle of approximately 2.5. The trend lines of the separation and reattachment points intersect near the scaled ramp angle required for incipient separation, which was independently found using an iterative approach.



(a) Scaled shear stress.



(b) Scaled pressure distribution.

Figure 2.4: Scaled shear stress and scaled pressure distribution at a range of scaled ramp angles.

The expected trends are present in Figure 2.5, namely the size of the separated region increases as the scaled ramp angle increases. The triple-deck equations represent a simplification of the full set of governing equations. As such, triple-deck theory can be said to be an approximation of the actual physics. The mentioned

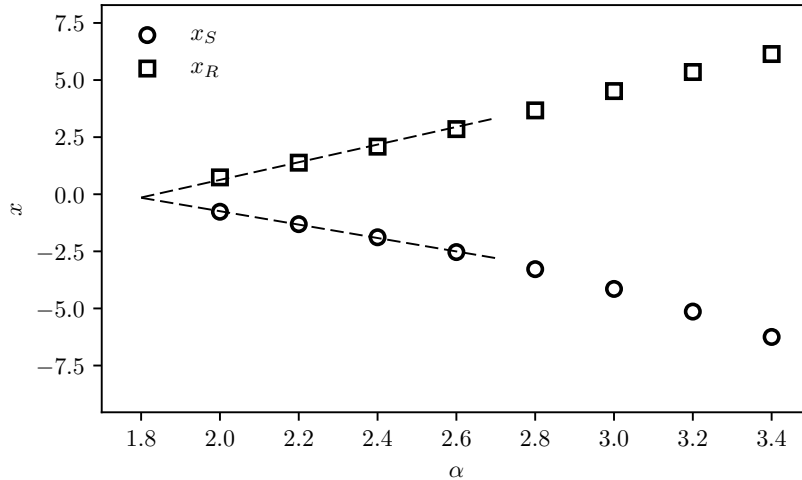


Figure 2.5: Scaled separation and reattachment points vs scaled ramp angle.

linear trends call into question whether the separation and reattachment points from solutions to the full set of governing equations will also exhibit linear trends when scaled using the triple-deck scalings.

### 2.4.3 Curvature effects

Curvature effects are now investigated using the variable  $\tilde{r}$  present in the geometric definition given by (2.10). The effects of changing surface curvature on the geometry definition can be seen in Figure 2.6. Increasing  $\tilde{r}$  gradually smooths the corner.

Figure 2.7 shows how the changes in the surface curvature affect the scaled pressure and scaled shear stress distributions. The changes in the surface pressure distributions due to changes in surface curvature are very minor (see Figures 2.7(a), 2.7(c), 2.7(e)). However, the changes in the shear stress distributions due to the changes in curvature are more readily evident. More specifically, Figure 2.7(b) shows that the minimum value of shear stress, which occurs at the corner, increases as the

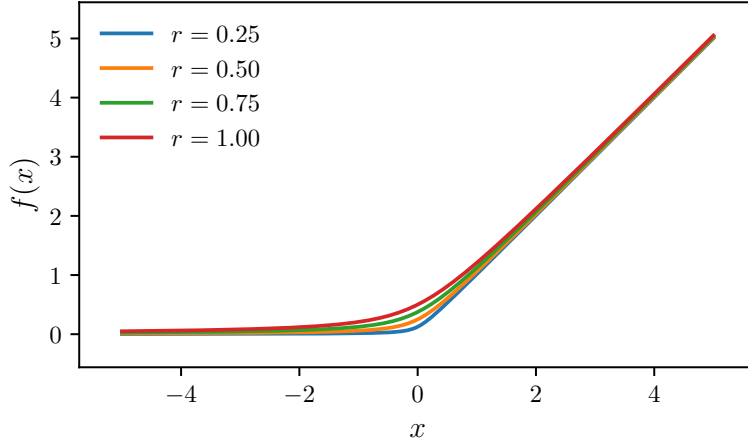
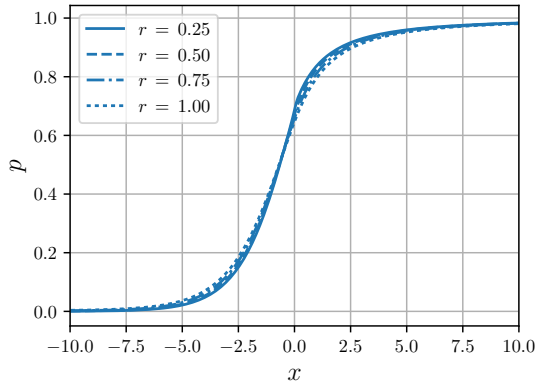


Figure 2.6: Effect of increasing surface curvature on triple-deck ramp geometry.

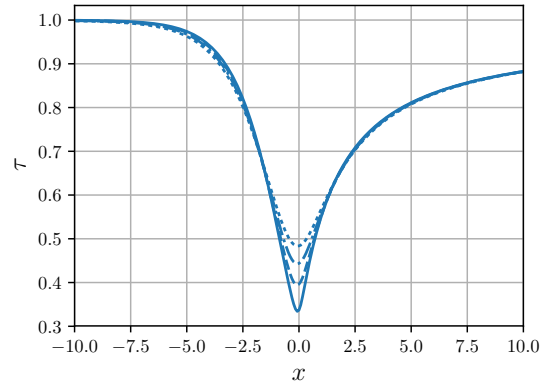
surface curvature increases. Figure 2.7(d) shows that increasing surface curvature actually removes the small separated region. That is, for  $\tilde{r} = 1$  in Figure 2.7(d), there is no separation, as evidenced by the fact that the shear stress is always positive. For the case of  $\alpha = 3$  as depicted in Figure 2.7(f), a much larger separated region is present as compared to the case with  $\alpha = 2$ . Changes in the surface curvature has less of an effect on this larger separated region, as compared to the small separated region present in the  $\alpha = 2$  interaction.

Figure 2.8 shows a plot of the separation and reattachment points versus the parameter which controls the surface curvature,  $\tilde{r}$ . For the scaled ramp angle of 3, changes in surface curvature have little effect on the separation and reattachment points. However, increasing the parameter  $\tilde{r}$  from 0.75 to 1 for the  $\alpha = 2$  case results in removal of the small separated region. Said another way, increasing the surface curvature gradually shrinks the size of the separated region until it is removed altogether. These results suggest that it is possible to mitigate small separations via increasing surface curvature. This is possible because increasing the radius of curvature has the effect of decreasing the pressure gradient by spreading the pressure rise

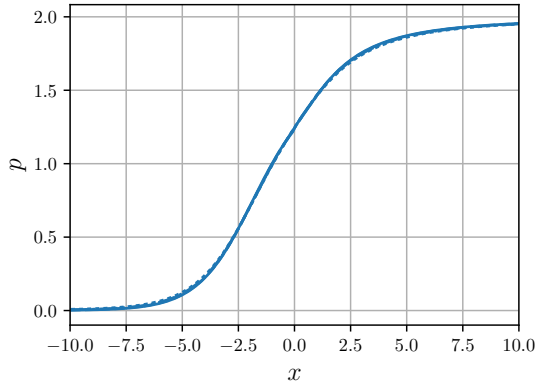
over a larger distance. This might be of limited use since for such a small separation, the adverse effects of shock wave/boundary layer interactions such as flow unsteadiness and increased heat transfer are likely not severe. We now move to numerical solutions of the full set of governing equations.



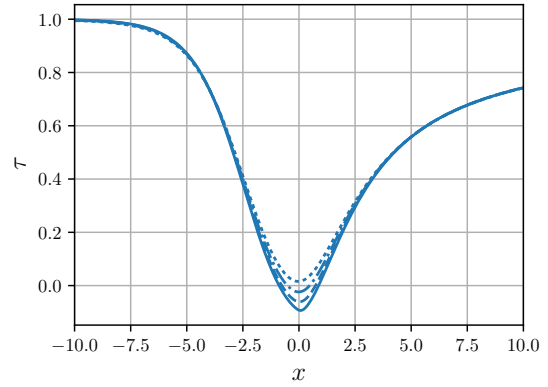
(a) Scaled pressure for  $\alpha = 1$ .



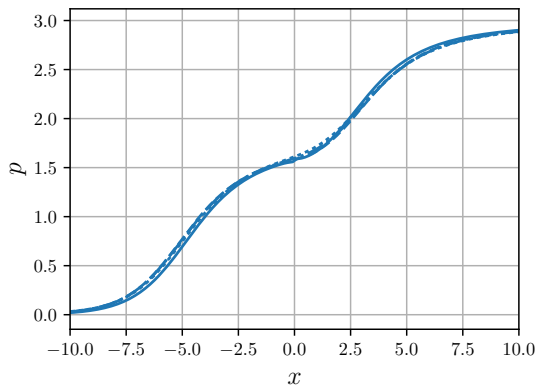
(b) Scaled shear stress for  $\alpha = 1$ .



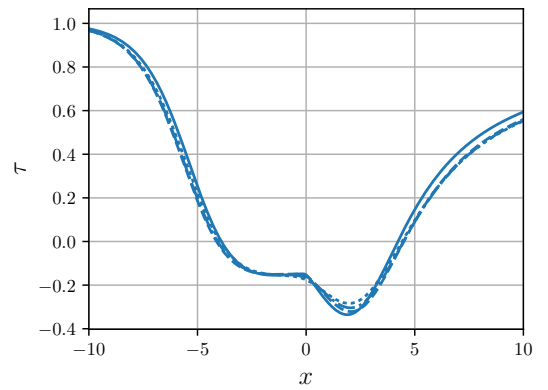
(c) Scaled pressure for  $\alpha = 2$ .



(d) Scaled shear stress for  $\alpha = 2$ .



(e) Scaled pressure for  $\alpha = 3$ .



(f) Scaled shear stress for  $\alpha = 3$ .

Figure 2.7: Surface curvature effects on scaled pressure and scaled shear stress distributions.

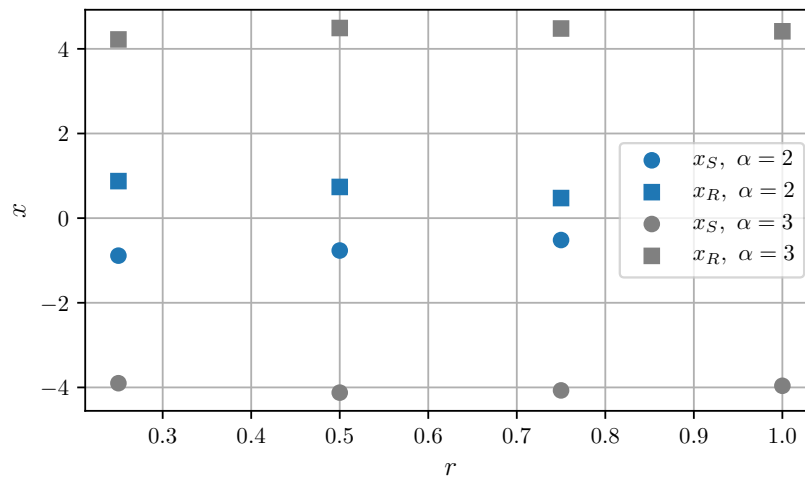


Figure 2.8: Scaling of separation and reattachment points for different surface curvature and different ramp angles.

## CHAPTER 3

### TWO-DIMENSIONAL NUMERICAL SOLUTIONS

In general, the numerical solution of partial differential equations requires three steps: pre-processing, solution of the discretized system, and post-processing. The pre-processing step involves defining the geometry and generating meshes. The mesh and relevant physical quantities, such as freestream Mach number and Reynolds number, are inputs to the flow solver. The flow solver outputs data which must then be further reduced to a form from which meaningful insights may be drawn. These steps are described next, followed by results and discussion.

#### 3.1 Geometry and mesh generation

Figure 3.1 shows the geometry which was modeled. Compression ramps have a geometric discontinuity in the first derivative,  $dy/dx$ . In the present work, this discontinuity has been shifted to the second derivative by using a circular arc with radius  $r$  to turn the flow more gradually than a sharp ramp. The length of the flat

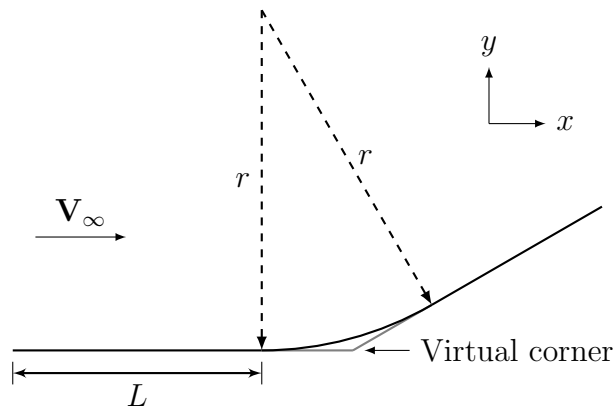


Figure 3.1: Schematic of ramp geometry.

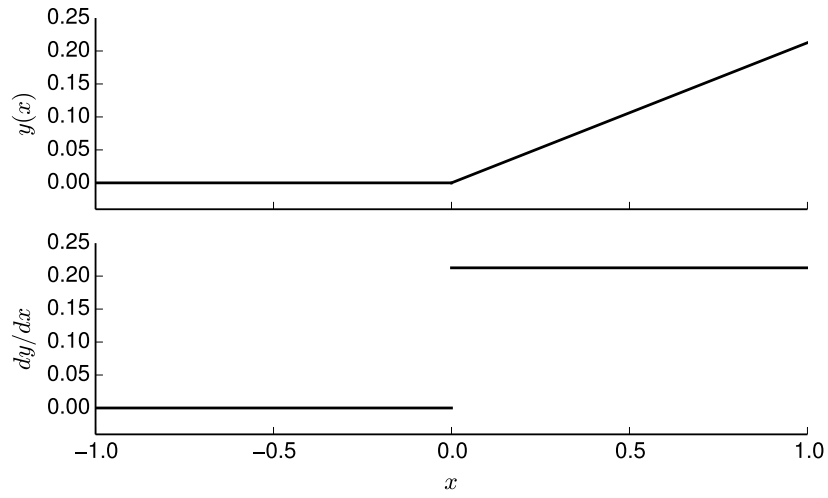
plate portion is measured relative to the beginning of the circular arc. The surface definitions and derivatives are plotted in Figure 3.2 to elucidate the discontinuities. A circular arc was used rather than, for example, an isentropic ramp because the radius of curvature is constant. An isentropic ramp geometry involves variable radius of curvature, therefore making it more difficult to quantify a characteristic length scale related to radius.

Figure 3.2(a) shows the surface geometry and the slope for the normal compression ramp. There is a very obvious discontinuity in the first derivative at  $x = 0$ . Figure 3.2(b) shows the surface geometry, the slope and the curvature of the ramp with the circular arc at the corner. The geometry is continuous up until the second derivative, hence the mention of shifting the discontinuity to a higher derivative.

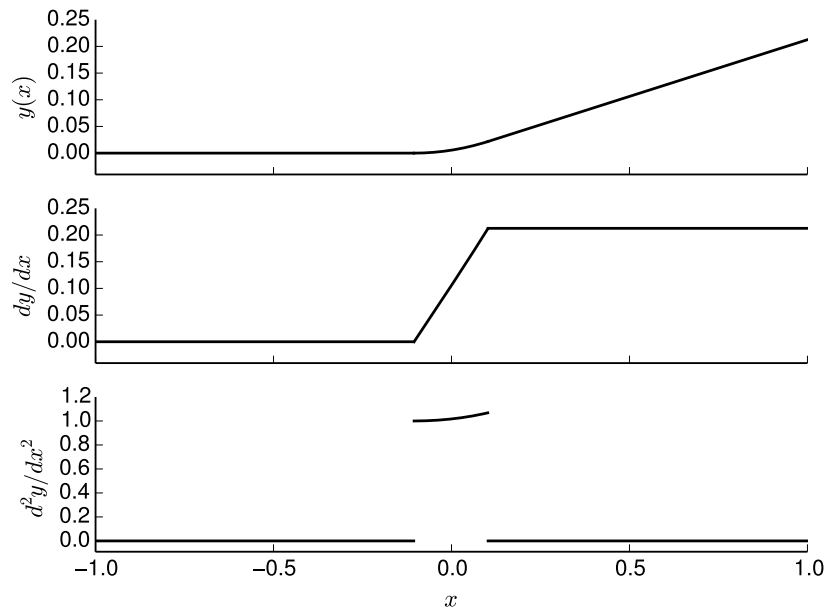
Pointwise<sup>®</sup> Glyph scripting was used to automate mesh generation. Only structured meshes are used in the present work to avoid biasing that may be introduced by tetrahedral and prism elements. For more information about tetrahedra and prisms in FUN3D, see [35]. An example mesh with every third point shown for clarity is provided in Figure 3.3. The dense clustering near the left side of the mesh is necessary to resolve the leading edge growth of the boundary layer. The mesh is also clustered in the wall-normal direction so that the boundary layer is resolved. Additional clustering is included where the boundary layer is ingested at the outlet. Specifics about the boundary conditions are discussed in the next section.

## 3.2 Numerical scheme

The FUN3D (Fully Unstructured Navier–Stokes 3D) code was used to numerically solve the governing equations [36]. FUN3D is a node-based finite volume code which has been in continuous development at NASA Langley Research Center since the 1980s. The code has many advanced capabilities such as adjoint and feature-based



(a) Straight ramp.



(b) Circular arc ramp.

Figure 3.2: Ramp geometries and derivatives.

mesh refinement, static and dynamic aeroelastic simulations, and adjoint-based design optimization, to name a few. Second-order spatial accuracy was used in the present work along with dissipative LDFSS flux construction and a van Albada flux

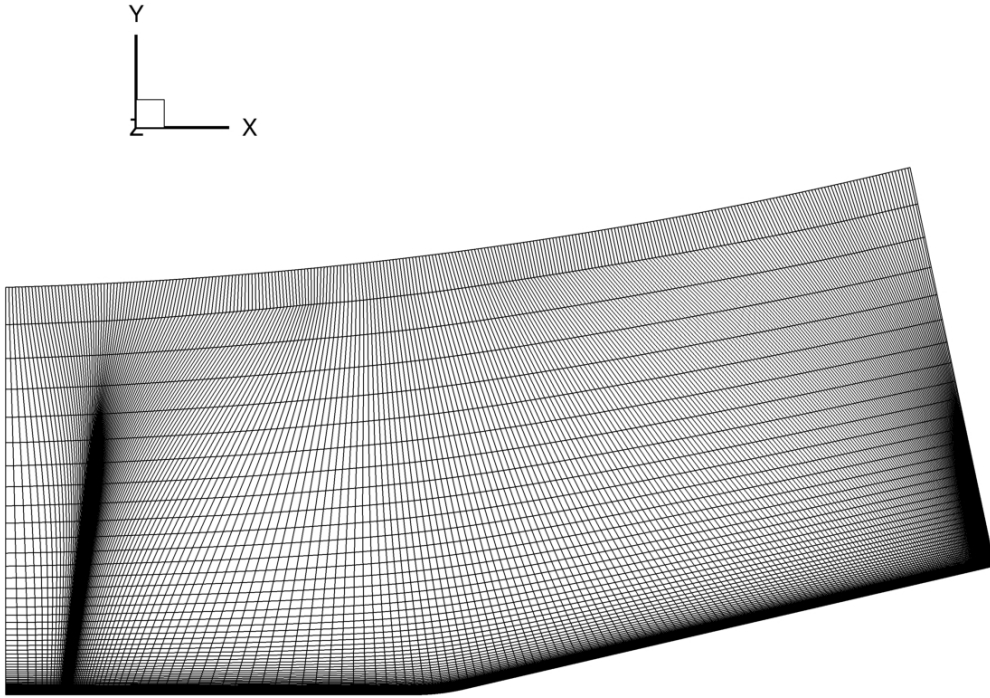


Figure 3.3: Example ramp mesh (every third point shown).

limiter [36]. The geometry creation, mesh generation and execution of the flow solver were automated using the TCL and Python scripting languages.

An overview of the numerical scheme will now be provided. For more details, see reference 37. The three-dimensional compressible Navier–Stokes can be written as a conservation law of the following form:

$$\frac{\partial \mathbf{q}}{\partial t} + \nabla \cdot \mathbf{F}(\mathbf{q}) = 0 \quad (3.1)$$

where  $\mathbf{F}$  is a tensor of rank 2 whose columns are flux vectors in each direction, and  $\mathbf{q}$  is a vector of conserved variables:

$$\mathbf{q} = \begin{bmatrix} \rho \\ \rho u \\ \rho v \\ \rho w \\ E \end{bmatrix} \quad (3.2)$$

where  $E = \rho e + \frac{1}{2}\rho(\mathbf{u} \cdot \mathbf{u})$ . The inviscid or advective fluxes at a face can be written as

$$\mathbf{F}_{\text{inv}} = \begin{bmatrix} \rho V \\ \rho u V + n_x p \\ \rho v V + n_y p \\ \rho w V + n_z p \\ HV \end{bmatrix} \quad (3.3)$$

where  $V$  is the contravariant velocity, defined by  $V = un_x + vn_y + wn_z$  and  $H$  is the total enthalpy,  $H = E + p$ . The viscous fluxes are written as

$$\mathbf{F}_{\text{visc}} = \begin{bmatrix} 0 \\ n_x \tau_{xx} + n_y \tau_{xy} + n_z \tau_{xz} \\ n_x \tau_{yx} + n_y \tau_{yy} + n_z \tau_{yz} \\ n_x \tau_{xx} + n_y \tau_{xy} + n_z \tau_{xz} \\ n_x \Theta_x + n_y \Theta_y + n_z \Theta_z \end{bmatrix} \quad (3.4)$$

where

$$\Theta_x = u\tau_{xx} + v\tau_{xy} + w\tau_{xz} - q_x \quad (3.5a)$$

$$\Theta_y = u\tau_{yx} + v\tau_{yy} + w\tau_{yz} - q_y \quad (3.5b)$$

$$\Theta_z = u\tau_{zx} + v\tau_{zy} + w\tau_{zz} - q_z \quad (3.5c)$$

The stress tensor can be written in index notation as

$$\tau_{ij} = \frac{\mu M_\infty}{Re} \left( u_{i,j} + u_{j,i} - \frac{2}{3} \delta_{ij} u_{k,k} \right) \quad (3.6)$$

Using Fourier's law, the heat transfer terms can be written as

$$q_i = -\frac{M_\infty}{Re(\gamma - 1)} \frac{\mu}{Pr} (a^2)_{,i} \quad (3.7)$$

Viscosity is computed using Sutherland's law. The ideal gas equation of state is used to close the system of equations:

$$p = (\gamma - 1) \left( E - \frac{1}{2} \rho (u^2 + v^2 + w^2) \right) \quad (3.8)$$

Integrating (3.1) over a finite control volume,  $\Omega$ ,

$$\int_{\Omega} \frac{\partial \mathbf{q}}{\partial t} d\Omega + \int_{\Omega} (\nabla \cdot \mathbf{F}) d\Omega = 0 \quad (3.9)$$

Using the divergence theorem, (3.9) becomes

$$\int_{\Omega} \frac{\partial \mathbf{q}}{\partial t} d\Omega + \oint_{\Gamma} (\mathbf{F} \cdot \hat{\mathbf{n}}) d\Gamma = \int_{\Omega} \frac{\partial \mathbf{q}}{\partial t} d\Omega + \oint_{\Gamma} (\mathbf{F}_{\text{inv}} - \mathbf{F}_{\text{visc}}) d\Gamma = 0 \quad (3.10)$$

Assuming the solution is constant over the control volume, (3.10) can be written as

$$\frac{d\mathbf{q}}{dt} = \frac{1}{\Omega} \left[ \sum_{i=1}^N (\mathbf{F}_{\text{inv}} - \mathbf{F}_{\text{visc}})_i \Delta S_i \right] \quad (3.11)$$

Now, the system of partial differential equations has been reduced to a system of coupled ordinary differential equations, which can be integrated in time. For more details about finite volume schemes, see the text by Blazek [38].

The boundary conditions used for the computations are shown schematically in Figure 3.4. The freestream state was set along the left boundary. A short inviscid wall preceded the viscous wall so that sharp gradients in the flow solution are not close to the inlet boundary. An extrapolate boundary condition was used at the exit of the

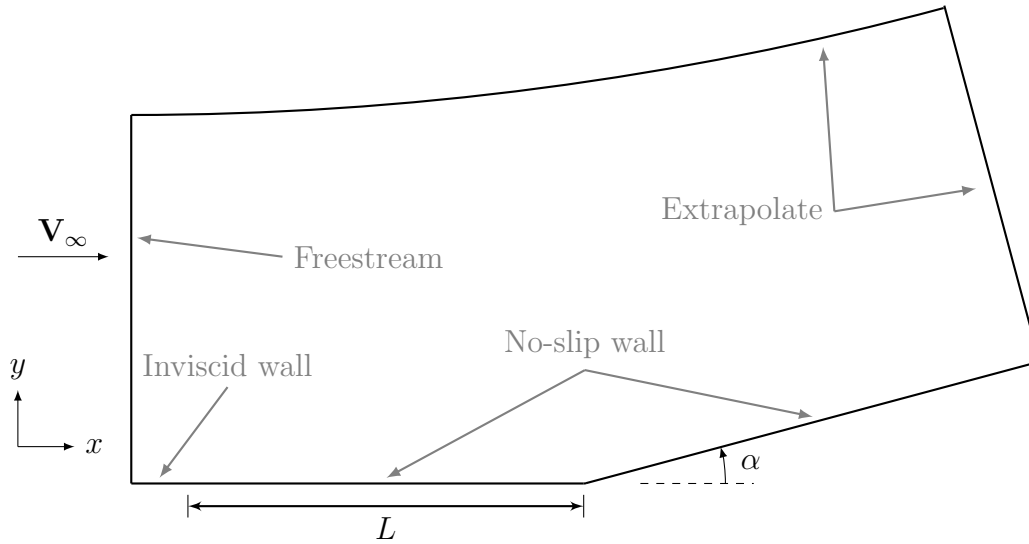


Figure 3.4: Computational domain.

domain and along the boundary. The boundary condition at the outlet extrapolates the state at the boundary if the local flow is supersonic. If the local Mach number was less than one, a back pressure was used to compute the state at the boundary. This back pressure was set using the inviscid pressure rise across a shock due to the deflection  $\alpha$ . This boundary condition is necessary to allow for ingestion of the subsonic portion of the boundary layer profile. An adiabatic, no-slip wall boundary was used along the flat plate of length  $L$  and the ramp.

### 3.3 Post-processing

Data reduction and visualization were accomplished using a combination of Python scripts, Tecplot<sup>®</sup>, and VisIt [39]. Specifically, Python scripts were developed for tasks such as extracting boundary layer profiles and computing integral thicknesses (e.g., displacement thickness). VisIt and Tecplot<sup>®</sup> were used mainly for visualization.

### 3.4 Validation

To ensure that FUN3D was capable of capturing the relevant physics, results from the code were compared against theoretical and experimental results. Each comparison is described in detail below.

#### 3.4.1 Flat plate

In this section, FUN3D results are compared against theoretical results for self-similar, laminar, supersonic flow over a flat plate. The theoretical results are obtained by transforming the flow to an equivalent incompressible flow via the Howarth–Dorodnitsyn compressibility transformation.

The Howarth–Dorodnitsyn transformation is one of several compressibility transformations which were constructed for the purpose of transforming compressible boundary layer problems into more simple incompressible problems. The main assumptions in the Howarth–Dorodnitsyn transformation are  $\mu \propto T$  and a Prandtl number of unity [40].

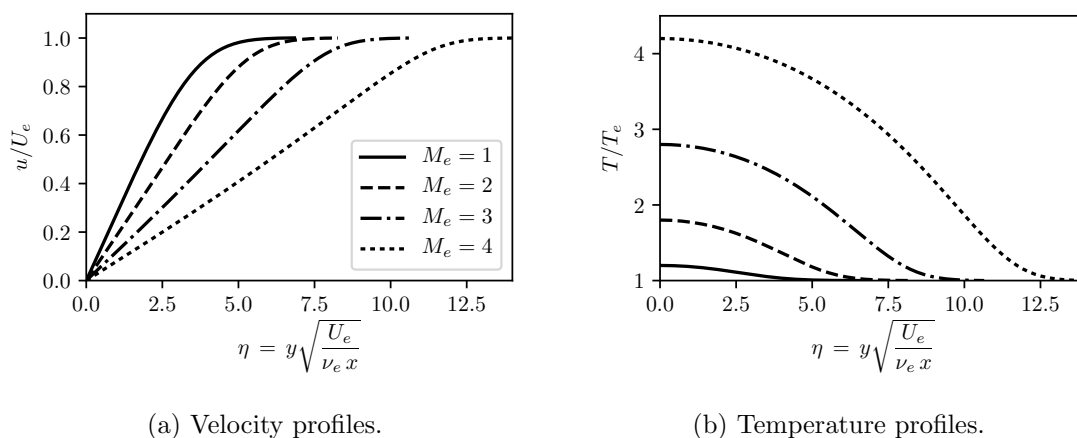


Figure 3.5: Howarth–Dorodnitsyn compressibility transformation results.

Essentially, the method involves “stretching” the normal coordinate via integration as follows:

$$Y = \int_0^y \frac{\rho(\tilde{y})}{\rho_e} d\tilde{y}, \quad (3.12)$$

where the subscript  $e$  refers to conditions at the edge of the boundary layer. The governing equations are then recast in terms of a compressible stream function. The resulting equation very much resembles Blasius equation. As such, Blasius solution can be defined in the  $(x, Y)$  plane. Finding the compressible solution requires inverting the transformation as follows:

$$y = \int_0^Y \frac{\rho_e}{\rho(\tilde{Y})} d\tilde{Y}. \quad (3.13)$$

Doing so yields the solution in the physical,  $(x, y)$  plane. For more information, see the original paper by Howarth [41].

A C++ code was developed for obtaining laminar boundary layer solutions using the Howarth–Dorodnitsyn transformation. The energy equation was solved simultaneously. The Odeint library from Boost was used to integrate the coupled system of ordinary differential equations, along with the NLopt library for performing the shooting procedure necessary to satisfy the boundary conditions [42, 43]. Sample results for an adiabatic wall can be seen in Figure 3.5.

FUN3D was used to simulate laminar flow over a flat plate of length  $L = 4$  m at  $Re_L = 300\,000$ ,  $M_\infty = 2.0$ ,  $T_\infty = 100$  K, and  $Pr = 1$ . The previously described Howarth–Dorodnitsyn transformation code was then run at the same conditions. Velocity profiles from FUN3D at different streamwise locations were then plotted in terms of the Blasius similarity variable,  $\eta$ . A comparison between the theoretical velocity profile and FUN3D velocity profiles is shown in Figure 3.6. The collapse of the FUN3D velocity profiles shows that they are indeed self-similar. Also, the profiles compare relatively well.

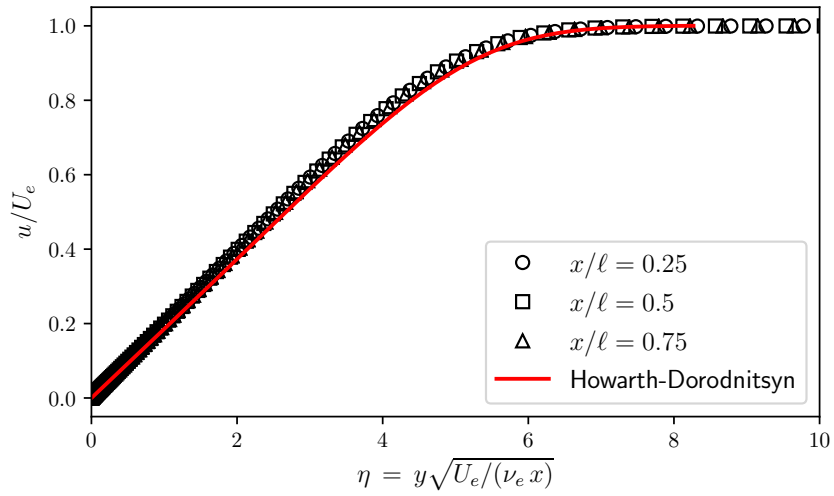


Figure 3.6: Comparison between the transformed Blasius profile and FUN3D velocity profiles at different streamwise locations.

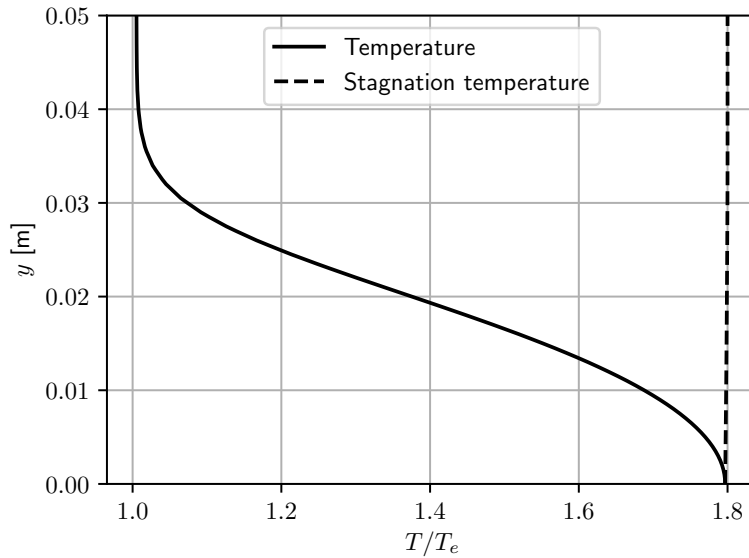


Figure 3.7: Stagnation and static temperature profiles at  $x/\ell = 0.5$ .

The total temperature should be constant since the flow is adiabatic,  $Pr = 1$ , and the gas is assumed to be calorically perfect. Figure 3.7 shows the static and total temperature profiles in the boundary layer at  $x/\ell = 0.5$ . As expected, the stagnation temperature is essentially constant. The self-similarity of the CFD velocity

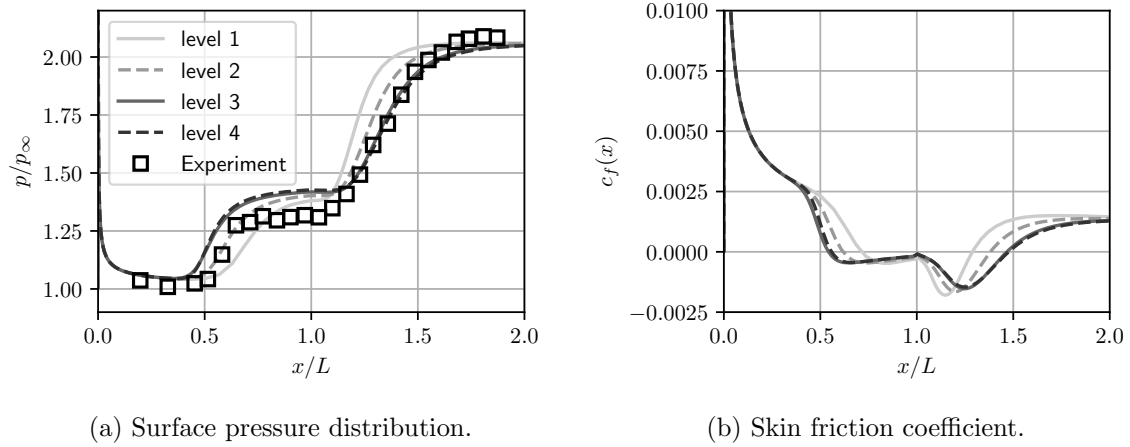


Figure 3.8: Comparison between FUN3D and Sfeir's experimental results [2].

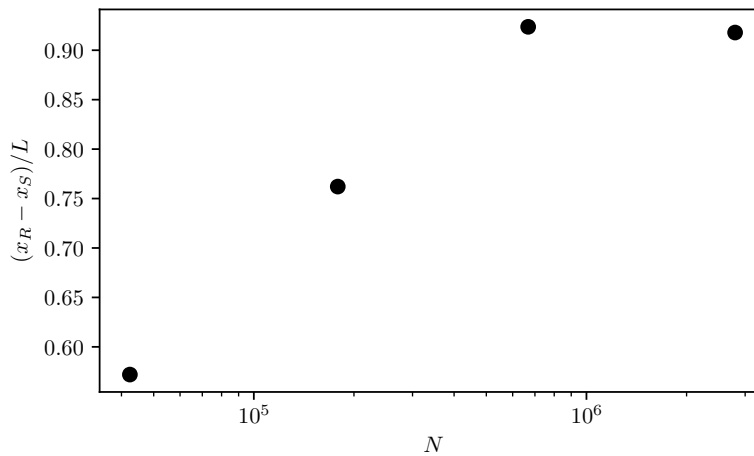


Figure 3.9: Size of separated region versus number of nodes in the mesh.

profiles along with the good comparison between CFD and theory and constant stagnation temperature in the boundary layer instill confidence that the code is capable of resolving the relevant physics.

### 3.4.2 Ramp

A comparison with the experiments of Sfeir was undertaken to ensure that FUN3D is capable of adequately capturing the physics of laminar SBLIs [2]. The

experiments made use of a compression ramp which was preceded by a 4 inch long flat plate. FUN3D was compared against test cases with  $Re_L = 140\,000$ ,  $M_\infty = 2.64$ , and an adiabatic wall. This comparison also allows for the determination of the necessary mesh resolution required for a mesh-independent solution. Results can be seen in Figure 3.8. In this case, the origin is at the beginning of the plate rather than the corner.

Figure 3.8(a) shows a comparison between the experimental pressure distribution and CFD pressure distributions for various mesh resolutions. Close examination reveals that there is not much change in the surface pressure distribution between levels 3 and 4. This conclusion is further reinforced by Figure 3.8(b), which shows little change in the skin friction distribution between levels 3 and 4.

Since the scaling of the separated region is to be studied, it is of interest to examine how the mesh resolution affects the size of the separated region. Figure 3.9 shows the size of the separated region versus the number of nodes in the mesh. As the mesh resolution increases, the growth of the separated region plateaus. This result is indicative of reaching a mesh resolution beyond which the metrics of interest do not substantially change. That is, the fine mesh is adequate to resolve the interaction.

Figures 3.10 and 3.11 show contours of Mach number and a computational schlieren image for the given experimental conditions, respectively. Schlieren images make use of the fact that density gradients change the index of refraction of light. The image shown in Figure 3.11 was computed by plotting contours of the norm of the density gradient,  $|\nabla\rho|$ . The overall structure of compression ramp-induced SBLIs, which was discussed in Chapter 1, is present in this figure. The separation bubble is evident near the corner, as is the separation shock, which is followed by the reattachment shock. The dark region near the wall in the computational schlieren is due to the large density variations in the boundary layer. The leading edge shock

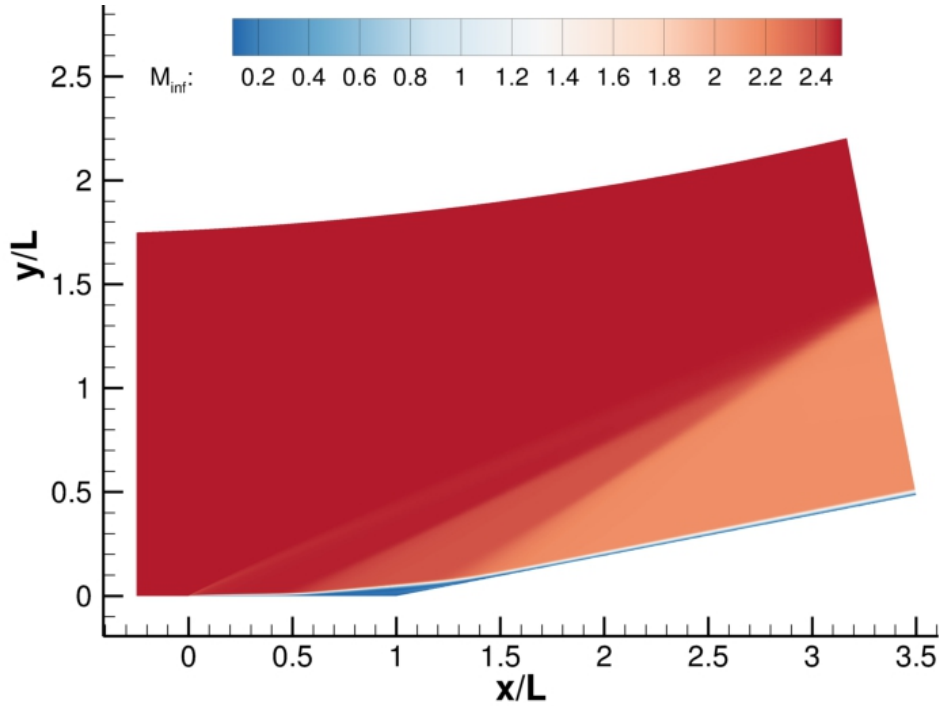


Figure 3.10: Contours of Mach number at  $Re_L = 140\,000$ ,  $M_\infty = 2.64$  and  $\alpha = 11$  degrees.

originates at the beginning of the flat plate region, where  $x/L = 0$ , and is due to the displacement thickness of the boundary layer which effectively deflects the flow.

### 3.5 Parametric sweep

To investigate the effects of the radius of curvature, Reynolds number and Mach number on the interaction, a parameter sweep was undertaken. The parameters can be seen in Table 3.1. The values of the radius (in inches) that were used are 0.05, 0.5, 1, 2, 3, 4, 5. Two different ramp angles of 8 degrees and 12 degrees were used to examine how the flow deflection affects the trends. A full-factorial sweep of these parameters yielded 420 flow solves, which were accomplished using the Lonestar 5 cluster at the Texas Advanced Computing Center.

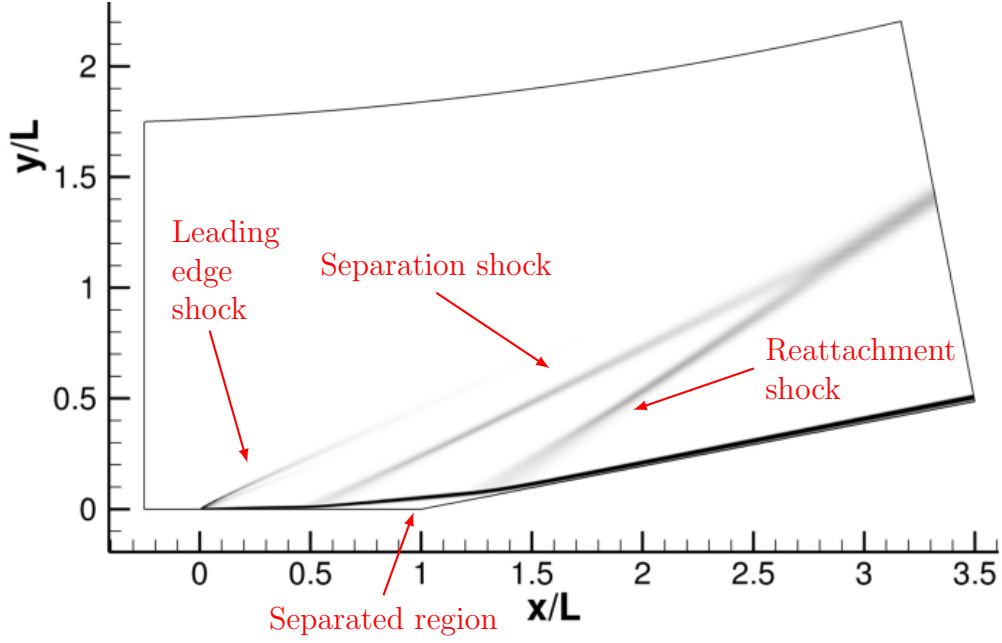


Figure 3.11: Computational schlieren image at  $Re_L = 140\,000$ ,  $M_\infty = 2.64$  and  $\alpha = 11$  degrees.

Table 3.1: List of parameters.

Parameter	Initial value	Final value	Increment
$M_\infty$	2	4	0.5
$Re_L$	50 000	200 000	30 000
$r$ [in]	0.05	5.0	—

### 3.5.1 Data reduction

The data reduction tasks were accomplished using a Python script which sequentially performed the following tasks: imported skin friction and surface pressure, computed upstream influence using a new, edge detection-based approach which is outlined in Appendix A, extracted boundary layer profiles at location of upstream influence using VisIt, computed integral thicknesses and shape factor, and plotted results. The boundary layer edge, denoted  $\delta_0$ , was determined by interpolating for

the  $y$ -location at which  $u = 0.99U_\infty$ . The integrals required to compute displacement thickness and momentum thickness were accomplished using Simpson's rule. The equations for integral thicknesses are provided below for completeness:

$$\delta_1 = \int_0^{\delta_0} \left( 1 - \frac{\rho(y)u(y)}{\rho_e U_e} \right) dy \quad (3.14)$$

$$\delta_2 = \int_0^{\delta_0} \left( 1 - \frac{u(y)}{U_e} \right) \frac{\rho(y)u(y)}{\rho_e U_e} dy \quad (3.15)$$

$$H = \frac{\delta_1}{\delta_2} \quad (3.16)$$

The results are presented in terms of the separation point, reattachment point, upstream influence, total size of separated region and shape factor at the location of upstream influence.

### 3.5.2 $\alpha = 8$ degrees

Figure 3.12 shows the scaling of the separation point, normalized by the displacement thickness computed at the location of upstream influence, as a function of the Reynolds number based on displacement thickness, freestream Mach number and radius of curvature in inches. Mach number effects are indicated by the different color plot markers. Radius of curvature effects are denoted by different symbols. For the cases with Mach number higher than 2.5, changes in the radius of curvature have little effect on the separation point. This finding is in accordance with free interaction. That is, the upstream portion of the shock boundary/layer interaction is independent of downstream events. In this case, changes in the downstream radius of curvature do not affect the location of boundary layer separation upstream.

Figure 3.14 shows how the location of boundary layer reattachment varies with Mach number, Reynolds number and radius of curvature. One difference between the separation and reattachment points is that the radius of curvature has an obvious

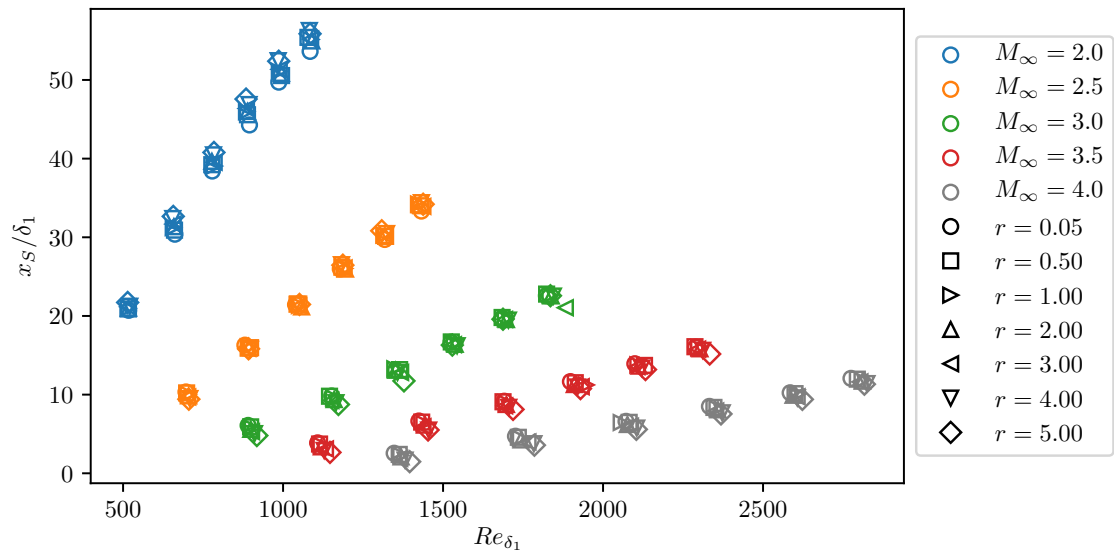


Figure 3.12: Separation point as a function of Reynolds number based on displacement thickness, Mach number and radius of curvature (inches).

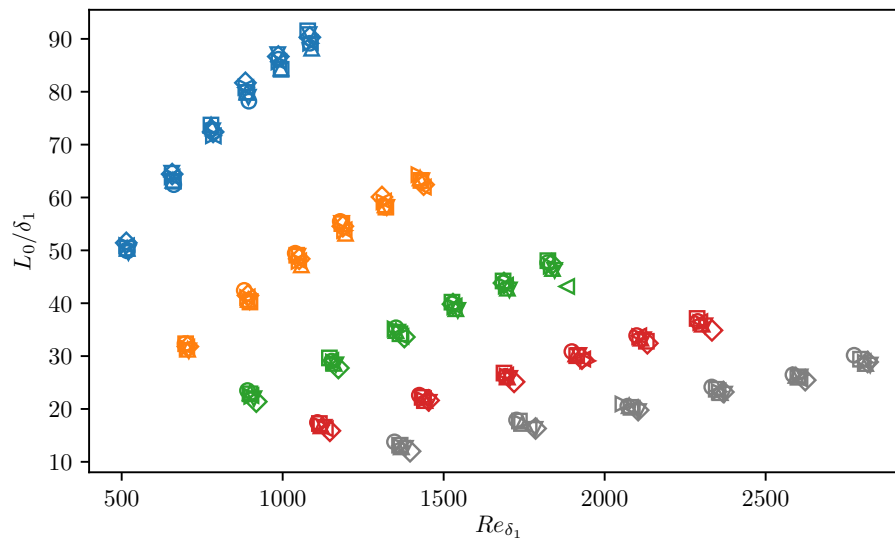


Figure 3.13: Upstream influence length as a function of Reynolds number based on displacement thickness, Mach number, and radius of curvature (inches).

effect on the point of reattachment. As the radius of curvature increases, the point at which the boundary layer reattaches moves downstream. This effect of elongating the

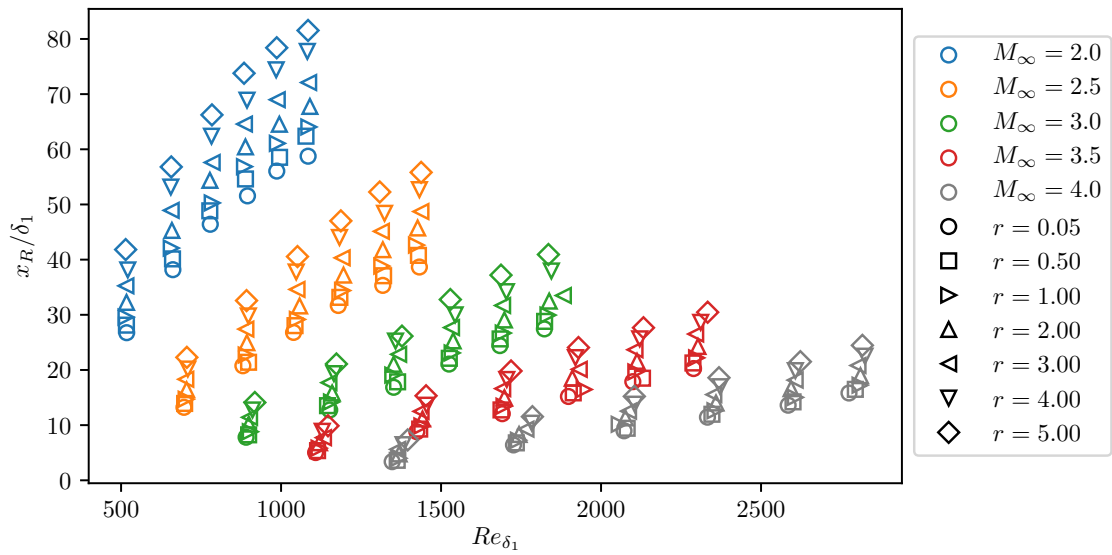


Figure 3.14: Reattachment point as a function of Reynolds number based on displacement thickness, Mach number, and radius of curvature (inches).

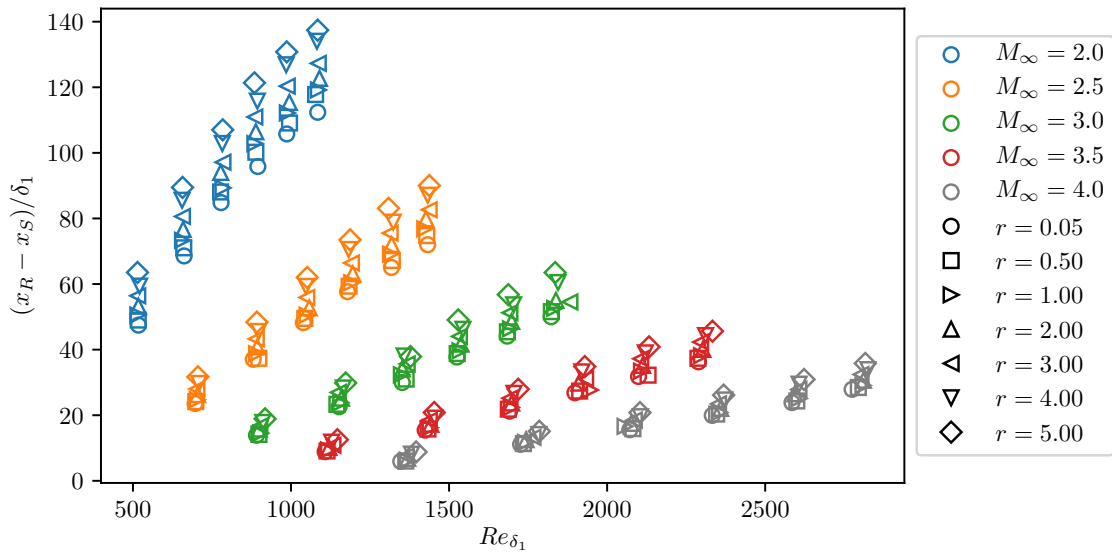


Figure 3.15: Size of separated region as a function of Reynolds number based on displacement thickness, Mach number, and radius of curvature (inches).

separation bubble increases as Mach number decreases, as indicated by the increasing spread of the data from Mach 4 to Mach 2.

Figure 3.15 shows the total size of the separated region. The trends in the overall separation size follow the trends of the separation and reattachment points. The figure is included for completeness.

Figure 3.16 shows the boundary layer shape factor as a function of the different parameters. The shape factor is important because it can be used to judge the “health” of the boundary layer. Increasing shape factor indicates increasing adverse pressure gradient imposed on the boundary layer. Examination of the figure reveals that the shape factor at the location of upstream influence is largely independent of Reynolds number and radius of curvature. This is somewhat expected due to the location at which the boundary layer profiles were extracted. The location of upstream influence represents the furthest upstream that the shock wave/boundary-layer interaction has a noticeable effect. If the upstream influence identification procedure that was developed is correct, it should identify the most downstream point at which the flow is representative of flow over a flat plate. Laminar compressible flow over a flat plate is self-similar which implies that the shape factors at different streamwise locations should be identical. This fact is represented in Figure 3.16 and represents validation that the procedure developed to identify the location of upstream influence is correct.

### 3.5.3 $\alpha = 12$ degrees

A full parametric sweep was accomplished at a flow deflection angle of 12 degrees in order to assess the effects of the ramp angle on the interaction. For the 8 degree flow deflection, the flat plate which preceded the ramp was set to a length of 6 inches. This distance was found to be too short for a flow deflection of 12 degrees because the interaction spreads far enough upstream that leading edge effects become significant. For an example, see Figure 3.17. The figure shows the pressure distribution for a

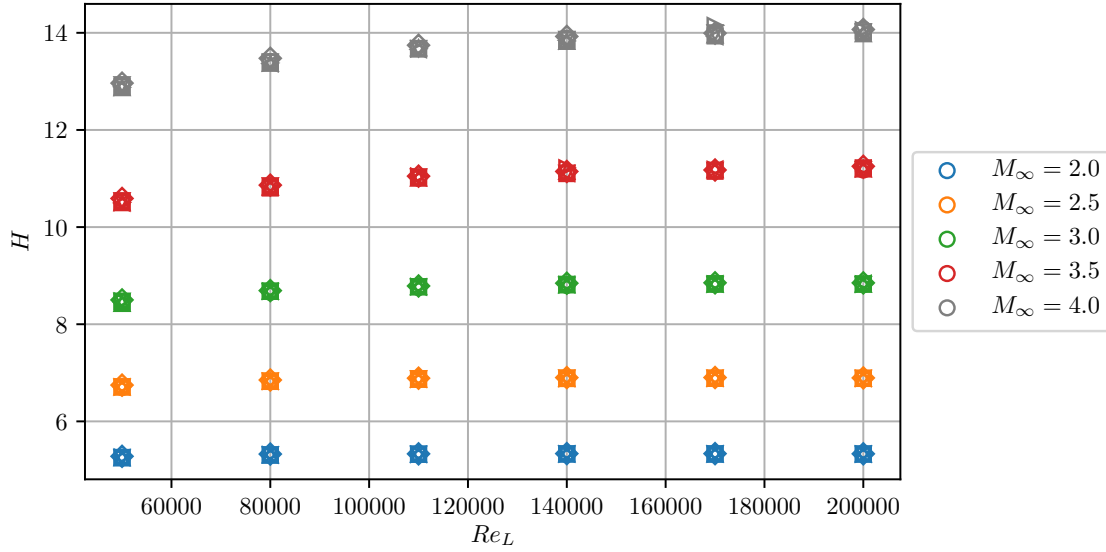


Figure 3.16: Shape factor for  $\alpha = 8$  degrees as a function of Reynolds number based on length, Mach number and radius of curvature (inches).

specific case in which the separation shock is far upstream. This upstream spreading of the interaction caused issues when computing the upstream influence. The errors in upstream influence propagated through the data reduction procedure because the boundary layer profiles were extracted at the location of the upstream influence. To mitigate this issue, the length of the flat plate portion was doubled from 6 inches to 12 inches and a new parametric sweep was undertaken. Results can be seen in Figure 3.18.

One major difference between the 8 degree flow deflection and the 12 degree flow deflection is that the separation point is strongly dependent on the radius of curvature for almost all cases. As the radius of curvature increases, the separation point moves further upstream. This trend is most evident for the Mach 2 case. For the highest Reynolds number Mach 2 case, the size of the separated region normalized

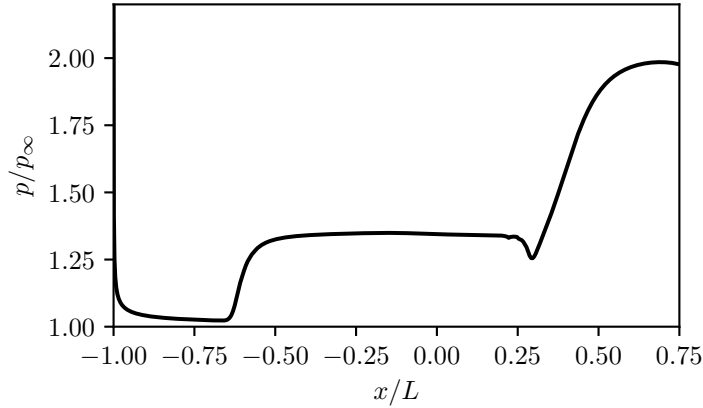


Figure 3.17: Example pressure distribution for  $\alpha = 12$  degrees.

by displacement thickness increases from approximately 150 to 200, which represents a 33 percent increase.

An additional observation is that the upstream separation point is much further upstream for the 12 degree flow deflection. This is to be expected since a larger flow deflection will cause a stronger shock wave to form, which in turn imposes a stronger adverse pressure gradient on the boundary layer.

Figure 3.19 depicts the effects of radius of curvature, Reynolds number and Mach number on the upstream influence length. The trends are obviously correlated with the upstream separation point. The upstream influence is larger than the separation point, because it represents the furthest upstream that the shock wave/boundary-layer interaction has a noticeable effect. The separation of the boundary layer is an effect of the adverse pressure gradient imposed by the shock wave. As such, the upstream influence length must be larger than the upstream length at which the boundary layer separates.

Figure 3.20 shows how the reattachment point changes as a function of the parameters. The same conclusions from the case with a ramp angle of 8 degrees hold

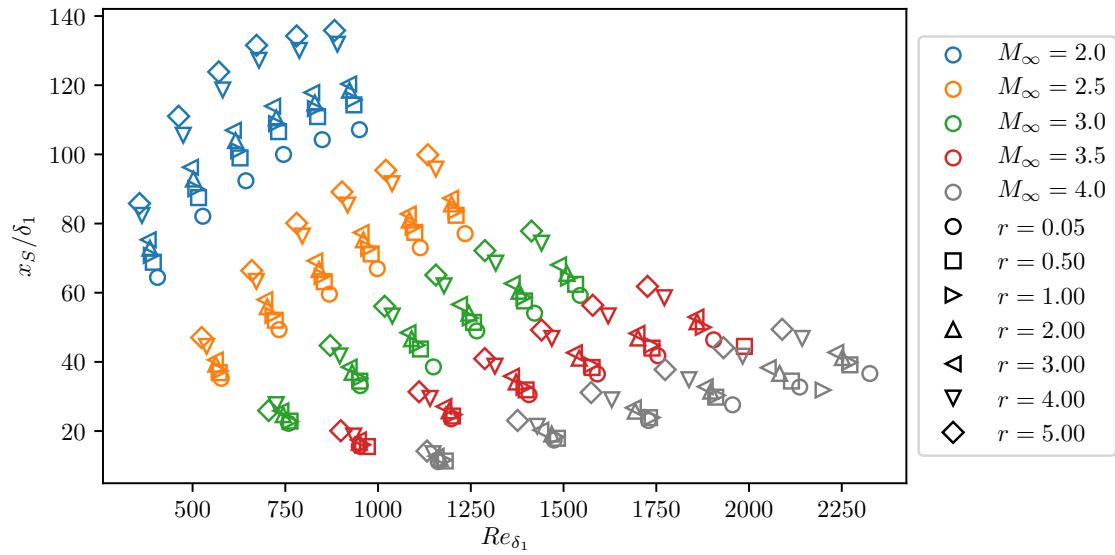


Figure 3.18: Separation point as a function of Reynolds number based on displacement thickness, Mach number and radius of curvature (inches).

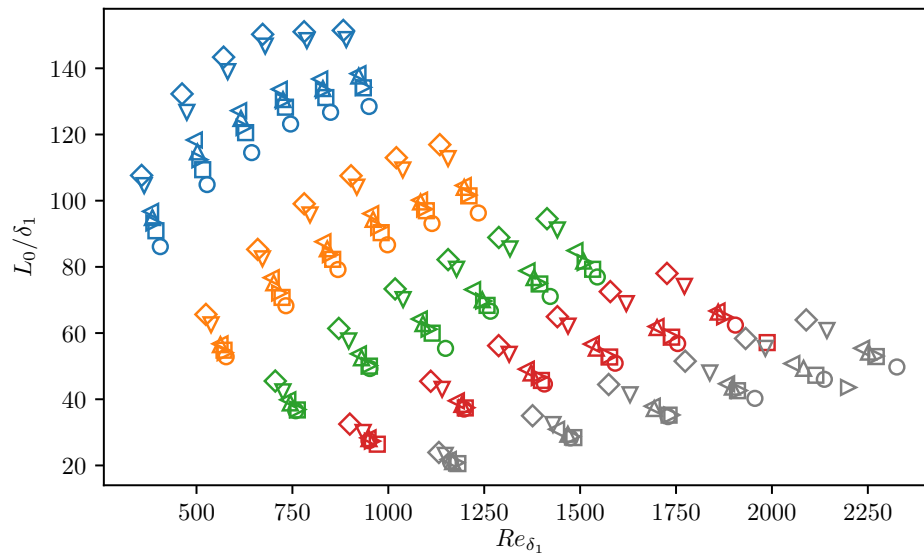


Figure 3.19: Upstream influence length as a function of Reynolds number based on displacement thickness, Mach number and radius of curvature (inches).

in this case, namely that as the radius of curvature increases, the reattachment point moves further downstream. This observation is reinforced by Figure 3.21, which shows

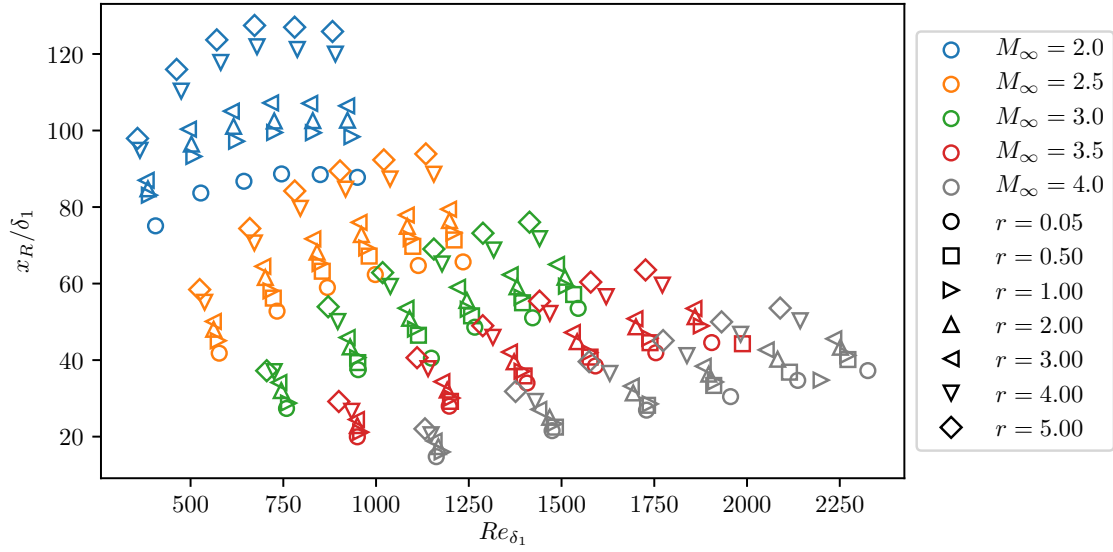


Figure 3.20: Reattachment point as a function of Reynolds number based on displacement thickness, Mach number, and radius of curvature (inches).

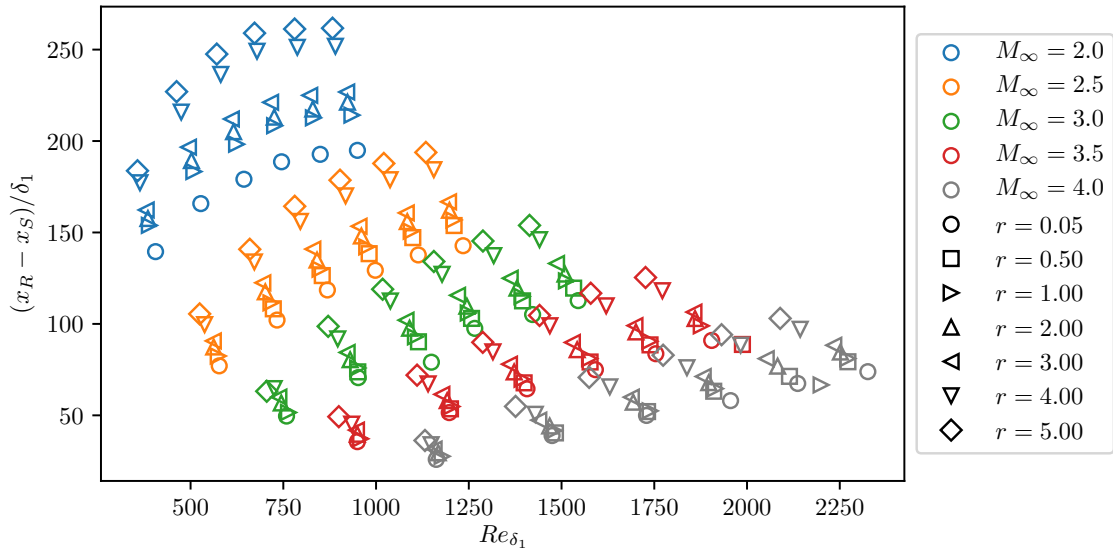


Figure 3.21: Size of separated region as a function of Reynolds number based on displacement thickness, Mach number, and radius of curvature (inches).

how Reynolds number, Mach number and radius of curvature affect the overall size

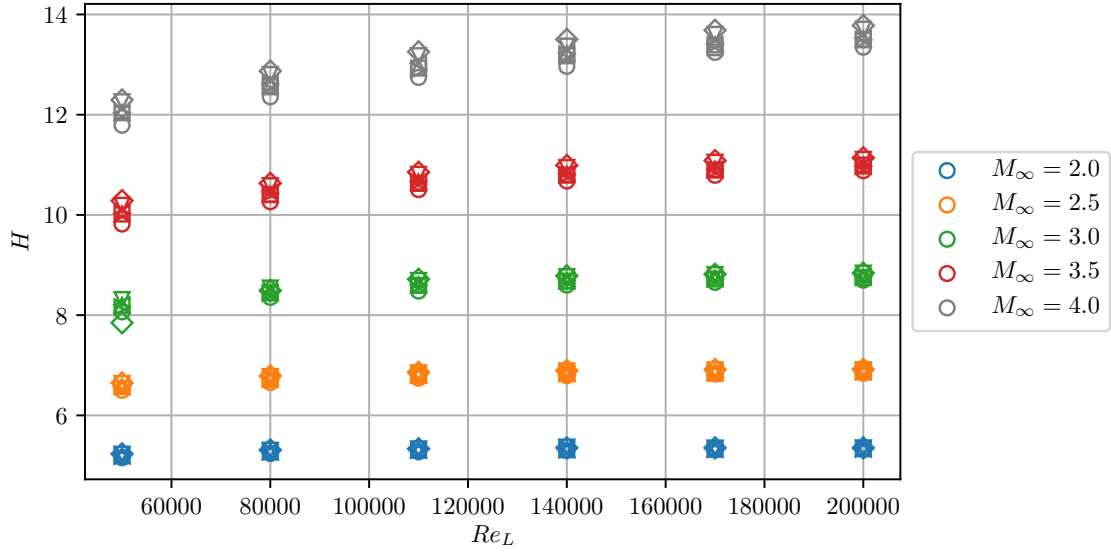


Figure 3.22: Shape factor for  $\alpha = 12$  degrees as a function of Reynolds number based on length, Mach number and radius of curvature (inches).

of the separated region. Increasing Mach number decreases the size of the separated region, while increasing Reynolds number has the opposite effect.

Figure 3.22 shows the shape factor as a function of Mach number, Reynolds number, and radius of curvature (represented by different marker shape). The shape factor is constant with changes in radius of curvature, as expected (see previous subsection for discussion).

### 3.5.4 Correlation based on free-interaction theory

Now, we turn to the development of a correlation for the point of separation as a function of Mach number and Reynolds number. Radius of curvature is excluded from the correlation initially because of the collapse of data shown in Figure 3.12. Modifications are then made to account for radius of curvature effects. The goal is to create a physics-based functional relationship between the parameters.

From free interaction theory,

$$L_0 \propto \delta_0^* (c_{f0})^{-1/2} (M_\infty^2 - 1)^{-1/4}, \quad (3.17)$$

where  $L_0$  is the interaction length,  $\delta_0^*$  and  $c_{f0}$  are the displacement thickness and the skin friction coefficient at the beginning of the interaction, respectively [7]. From traditional boundary layer theory,  $c_f \propto Re^{-1/2}$  and  $\delta^* \propto Re^{-1/2}$  so that

$$L_0 \propto [Re(M_\infty^2 - 1)]^{-1/4}. \quad (3.18)$$

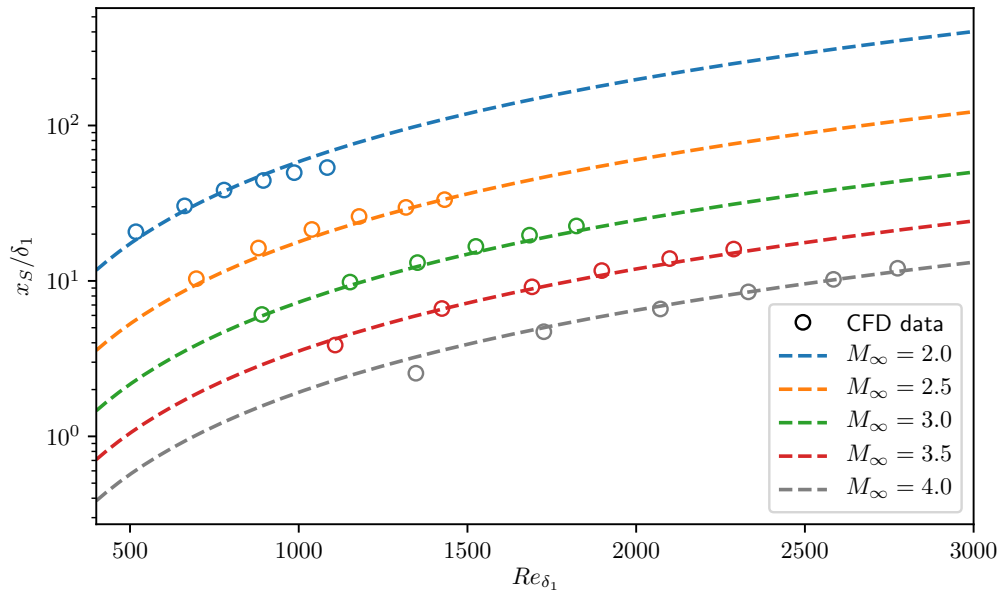
Using the fact that  $L_0$  and  $x_S$  follow roughly the same trends, as is shown in Figures 3.12 and 3.13, the functional relation between the separation point, Reynolds number and Mach number can be written as

$$\frac{x_S}{\delta_1} (Re_{\delta_1}, M_\infty) = C_1 Re_{\delta_1}^{C_2} (M_\infty^2 - 1)^{C_3}, \quad (3.19)$$

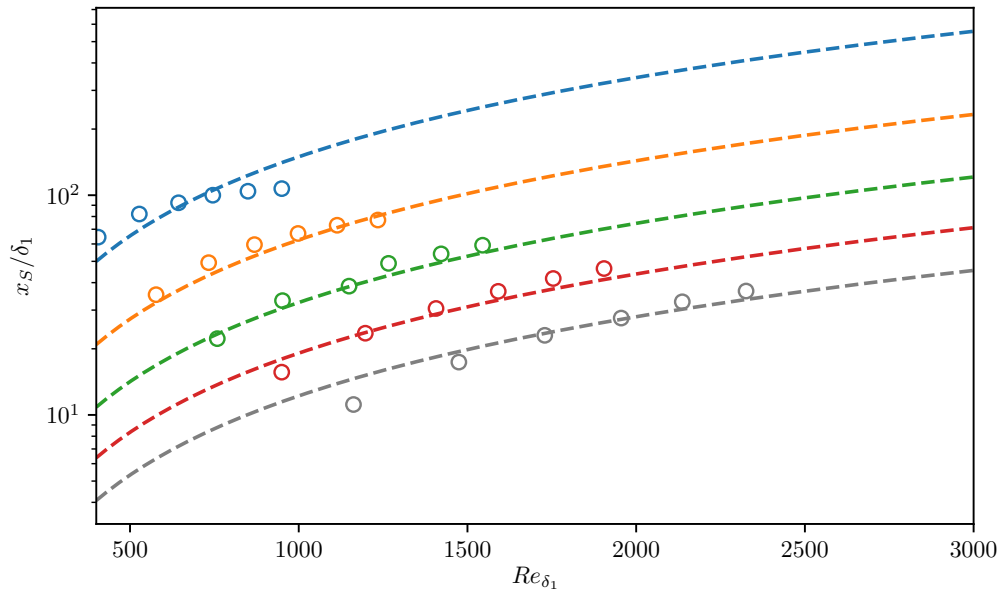
where the constants  $C_1$ ,  $C_2$ , and  $C_3$  are determined by a curve fit. Minimizing the sum-of-squares error between (3.19) and the CFD data for  $\alpha = 8$  degrees yields  $C_1 = 3.3 \times 10^{-3}$ ,  $C_2 = 1.75$ , and  $C_3 = -2.12$ . Figure 3.23(a) shows the curve fit. The functional relation given in (3.19) seems to adequately describe the trends present in the data. The same can be said for Figure 3.23(b), which shows the separation point, normalized by the displacement thickness at the location of upstream influence versus the Reynolds number based on displacement thickness for different Mach numbers for a flow deflection of 12 degrees. The numerical results and the scaling law compare well. For this case, the constants determined from the curve fit were  $C_1 = 0.213$ ,  $C_2 = 1.20$ , and  $C_3 = -1.56$ .

Modifications to the functional relation given in (3.19) are now undertaken in an effort to take curvature effects into account. A new length scale is defined,  $L'$ , which represents a virtual flat plate length. It can be written as

$$L' = L + \Delta L \quad (3.20)$$



(a)  $\alpha = 8$  degrees.



(b)  $\alpha = 12$  degrees.

Figure 3.23: Free-interaction theory-based scaling of separation point as a function of Mach number and Reynolds number for  $r = 0.05$  inches and different ramp angles.

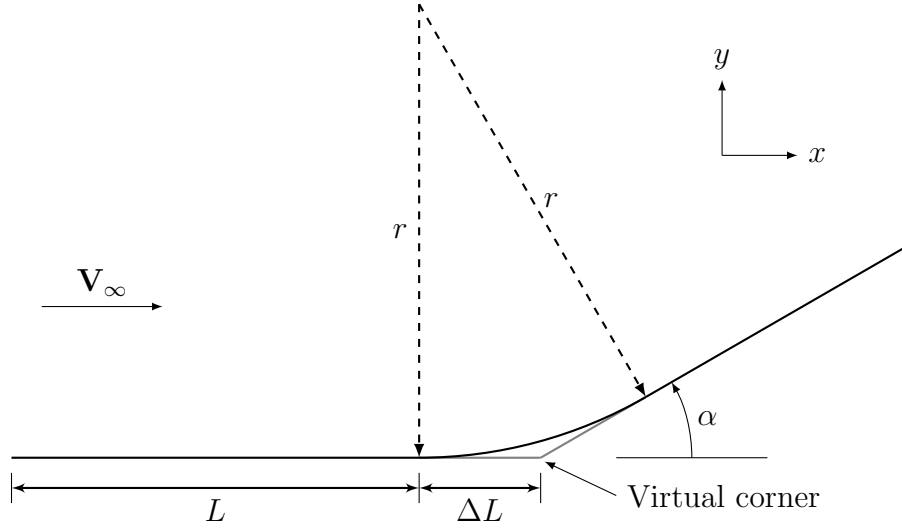


Figure 3.24: Schematic of ramp geometric parameters.

where  $L$  represents the length of the flat plate, and  $\Delta L$  represents the additional length required to reach the virtual corner. See Figure 3.24 for a schematic. For the case of a ramp with a corner that is rounded by a circular arc, (3.20) can be written as

$$L' = L + r \tan\left(\frac{\alpha}{2}\right) \quad (3.21)$$

where  $r$  is the radius of the circular arc used to smooth the corner, and  $\alpha$  is the ramp angle. The starting point for the new scaling relationship is what was predicted by free interaction theory:

$$x_S \propto L_0 \propto [Re(M_\infty^2 - 1)]^{-1/4} \quad (3.22)$$

Again the assumption that  $x_S \propto L_0$  is made due to the qualitative agreement between the trends in  $x_S$  and  $L_0$  presented earlier. In order to take curvature effects into account, the Reynolds number in (3.22) is based upon the virtual flat plate length,  $L'$ , rather than the flat plate length,  $L$ . The functional relation is then multiplied by

the virtual flat plate length normalized by the displacement thickness at the point of upstream influence as follows:

$$\frac{x_S}{\delta_1} \propto \frac{L'(r, \alpha, L)}{\delta_1} [Re_{L'}(M_\infty^2 - 1)]^{-1/4} \quad (3.23)$$

This relationship provided partial collapse of the data, but some Mach number effects were still present. Using a systematic trial-and-error approach, it was found that the Mach number, Reynolds number, and radius of curvature effects were all collapsed to a single line for each deflection angle by using the following

$$\frac{x_S}{\delta_1} \propto M_\infty^{5/4} \frac{L'(r, \alpha, L)}{\delta_1} [Re_{L'}(M_\infty^2 - 1)]^{-1/4} \quad (3.24)$$

The expression on the right hand side of (3.24) was set to an interaction parameter,  $\Gamma$ , so that the following functional relation can be written

$$\frac{x_S}{\delta_1} = f(\alpha, \Gamma) \quad (3.25)$$

Results can be seen in Figure 3.25. This is a new and unique result which has not been shown in the literature. A more complete scaling law will include the effect of the ramp deflection angle. The different colors in Figure 3.25 represent different Mach numbers, while the different symbols represent different radii of curvature, consistent with the previous plots.

### 3.5.5 Flow features

While post-processing the data, several interesting flow features were discovered. For an example, see Figure 3.26, which shows the streamlines inside the separated region for  $Re_L = 110\,000$ ,  $M_\infty = 2$ , and  $r = 4$  in. Dark arrows point to the small features inside the separated region.

Upon discovery of these features in the separated region, the fidelity of the numerical solutions to the compressible Navier–Stokes equations was investigated.

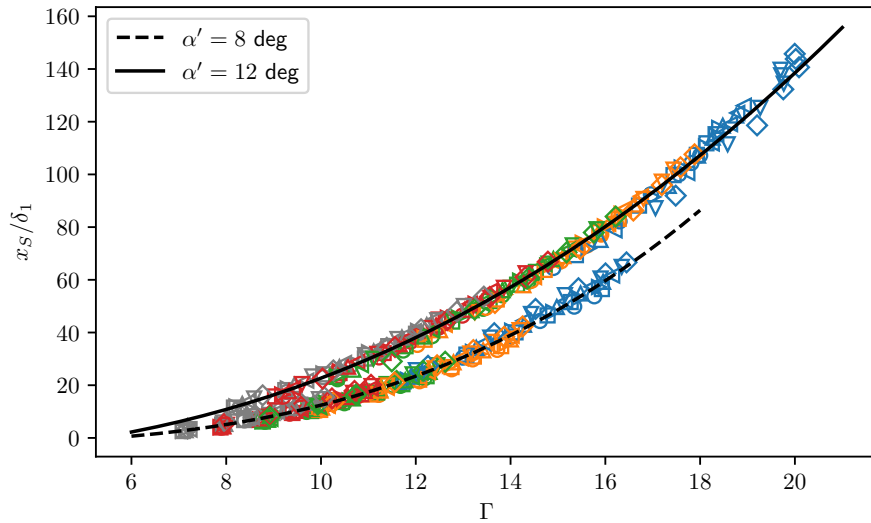


Figure 3.25: Collapse of Reynolds number, Mach number and radius of curvature effects for different deflection angles.

Figure 3.27 shows the residual convergence for the case shown in Figure 3.26. The residuals are a measure of how much the solution is changing between successive steps. The flow solver is executed with first-order spatial accuracy for the inviscid fluxes for the first 5000 iterations. The spatial accuracy for the inviscid fluxes is then switched to second-order for iterations 5000 to 15000. The flux limiter is frozen at 13000 iterations. Figure 3.27 shows that the residuals converged to at least  $1 \times 10^{-9}$ , which is satisfactory. Furthermore, oscillatory convergence, which is typical of flows that are inherently unsteady, is not evident in the figure. As a further check, a few cases were run in time-accurate mode. Inspection of the results showed that the flow was indeed steady.

Skepticism about the validity of the results is further alleviated by the similar CFD results of Brown, et al., and Sivasubramanian and Fasel [44, 45, 46]. Brown performed steady and unsteady simulations of a flare<sup>1</sup>-induced shock wave/boundary

<sup>1</sup>A flare is essentially an axisymmetric ramp.

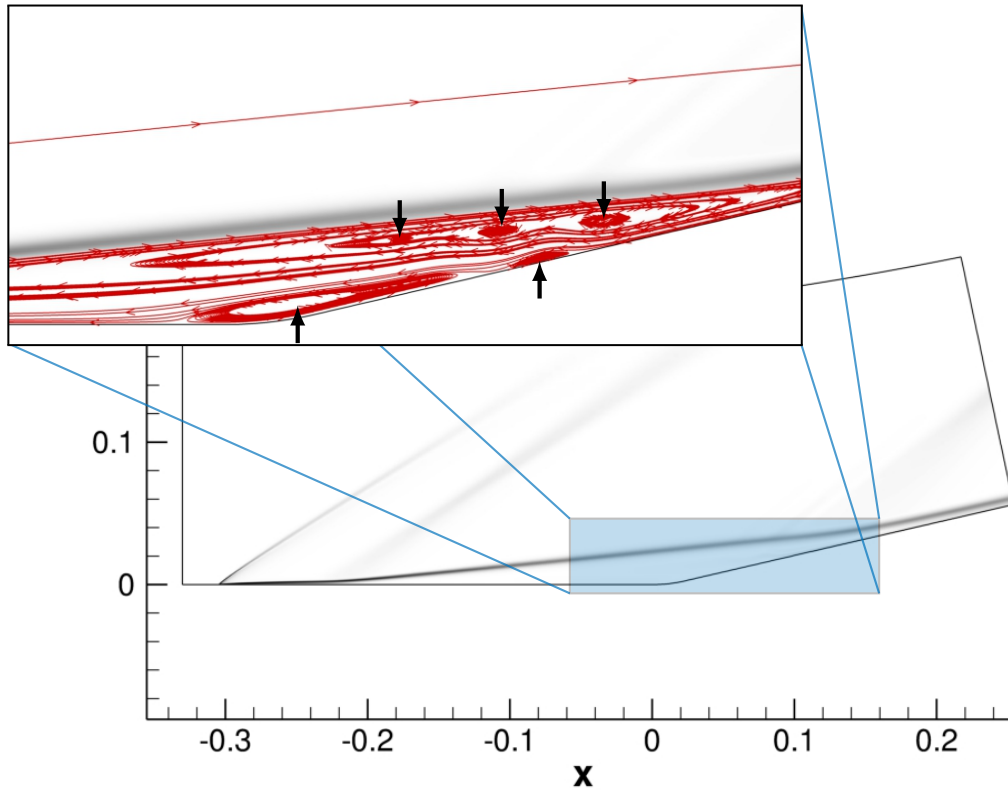


Figure 3.26: Example of separated region with multiple small features ( $Re_L = 110\,000$ ,  $M_\infty = 2$ ,  $r = 4$  inches).

layer interaction and found similar features to those seen in Figure 3.26. They hypothesized that a secondary separation, near the beginning of the separated region, destabilizes the separated boundary layer, which behaves as a free shear layer. They then suggested that the disturbances to the free shear layer are related to the formation of Görtler vortices. Furthermore, Brown conjectured that the formation of these additional features are a precursor to the quasi two-dimensional shock wave/boundary layer interaction becoming unsteady and three-dimensional. Sivasubramanian and Fasel performed two- and three-dimensional laminar simulations of an oblique shock impinging on a flat plate, followed by direct numerical simulations and linear stability analysis. DNS was used to simulate the transition process. Small spanwise

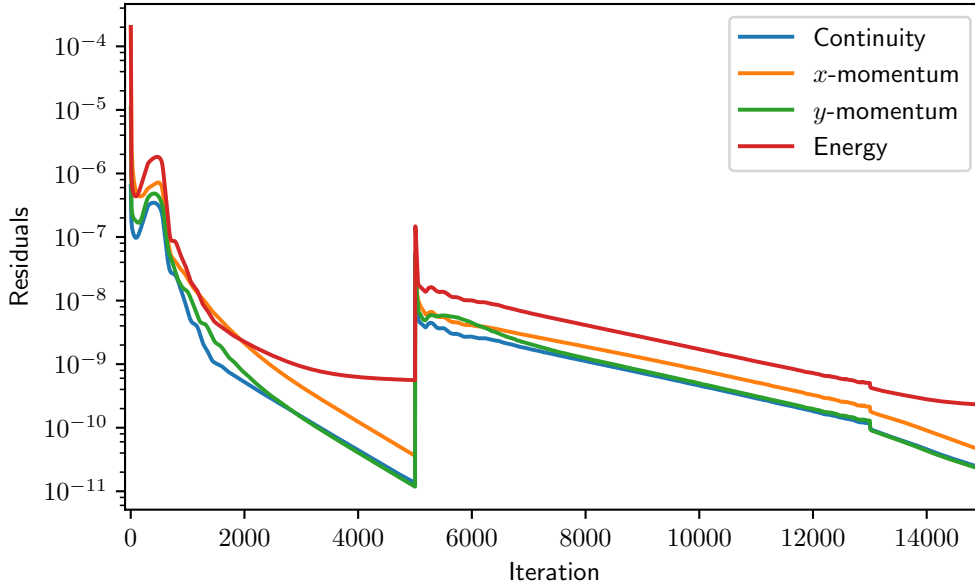
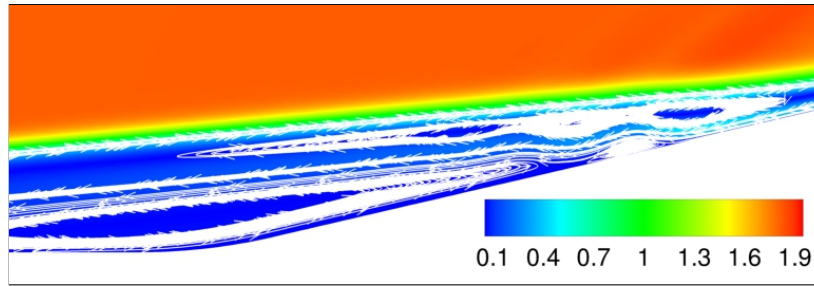


Figure 3.27: Residual convergence for  $Re_L = 110\,000$ ,  $M_\infty = 2$ , and  $r = 4$  inches.

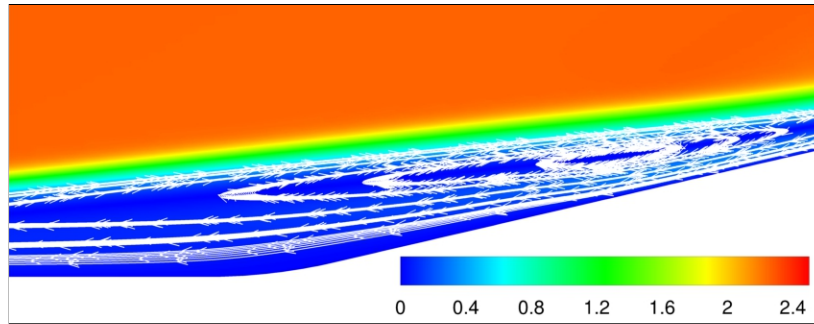
features were evident prior to the onset of instability. The idea that the nominally two-dimensional shock wave/boundary layer interaction becomes three-dimensional and unsteady was also investigated by Robinet using DNS and linear stability analysis [47]. Robinet found a three-dimensional, stationary global instability to be the cause of the three-dimensionality of the flow. Beyond the CFD results of other researchers, small spanwise features and secondary separations have also been seen in triple-deck solutions [16]. As such, it is believed that the observed features are physical and are not a numerical artifact.

Assuming the features inside the separated region are physical, the Mach number, Reynolds number, and radius of curvature effects on the number of features are now discussed. Mach number effects are presented first.

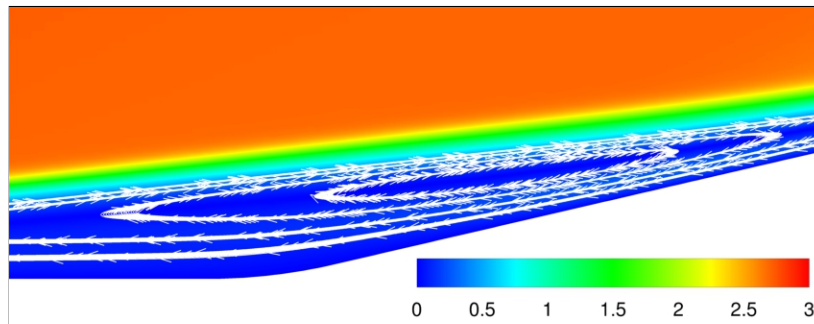
Figure 3.28 shows contours of Mach number for  $\alpha = 12$  degrees,  $Re_L = 200\,000$ , and  $r = 4$  in. As the Mach number increases from 2, to 2.5, the small features below



(a) Mach 2.



(b) Mach 2.5.



(c) Mach 3.

Figure 3.28: Mach number effects on the separated region ( $Re_L = 200\,000$ ,  $r = 4$  in.).

the separated boundary layer and the secondary separations disappear. No additional features appear at the higher Mach numbers. In their comprehensive experimental study, Chapman, et al., found that increasing the Mach number increases the stability of the free shear layer [13]. In the present results, increasing the Mach number decreases the number of features inside the separated region, which calls into question the influence of the free shear layer on the formation of these features.

Figure 3.29 shows how increases in Reynolds number change the features inside the separation bubble. As the Reynolds number increases, the number of features increases. Increasing the Reynolds number from 50 000 to 80 000 as shown in Figures 3.29(a-b), the large separation bubble splits into two smaller features. Increasing the Reynolds number further to 110 000, two secondary separations appear along the wall, and another feature appears near the shear layer, bringing the total number of features near the shear layer to three. Further increases in Reynolds number to 200 000 do not increase the number of features.

Radius of curvature effects are depicted in Figure 3.30 for  $Re_L = 110\,000$ , and  $M_\infty = 2$ . Beginning with Figure 3.30(a), three features are present, one secondary separation near the corner and two features near the separated boundary layer. Increasing the radius of curvature from 0.05 inches to 0.5 inches causes the secondary separation near the corner to grow larger, as is shown in Figure 3.30(b). Moving to a radius of curvature of 1 inch, an additional separation appears along the wall. Increasing further to  $r = 3$  in., an additional feature arises near the separated boundary layer and the secondary separations grow larger.

Increasing the Reynolds number above some critical value would lead to instability and eventually transition. With regard to Mach trends, Chapman, et al., suggested that increasing Mach number has a stabilizing effect on the free shear layer. Since increasing the Reynolds number increases the number of features present in the separated region, and increasing the Mach number decreases the number of features, it is of interest to consider the effects of these features on instability. To this end, three-dimensional numerical simulations were undertaken to determine when the shock wave/boundary layer interaction moves from a steady, nominally two-dimensional interaction to an unsteady three-dimensional interaction. Prior to presenting the

three-dimensional results, a novel comparison of triple-deck solutions and numerical solutions to the compressible Navier–Stokes equations is presented.

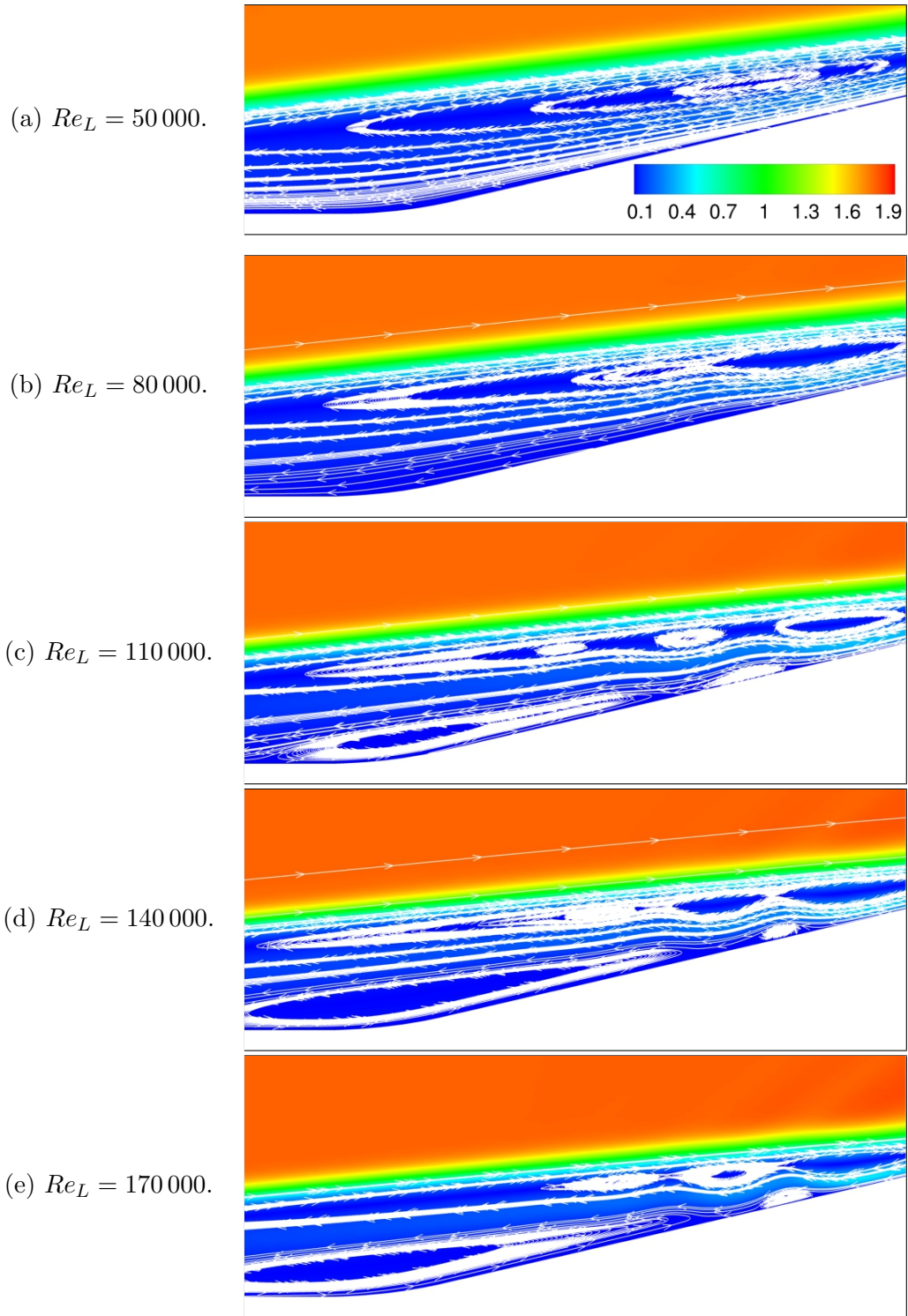


Figure 3.29: Reynolds number effects on the separated region ( $M_\infty = 2$ ,  $r = 4$  in.).

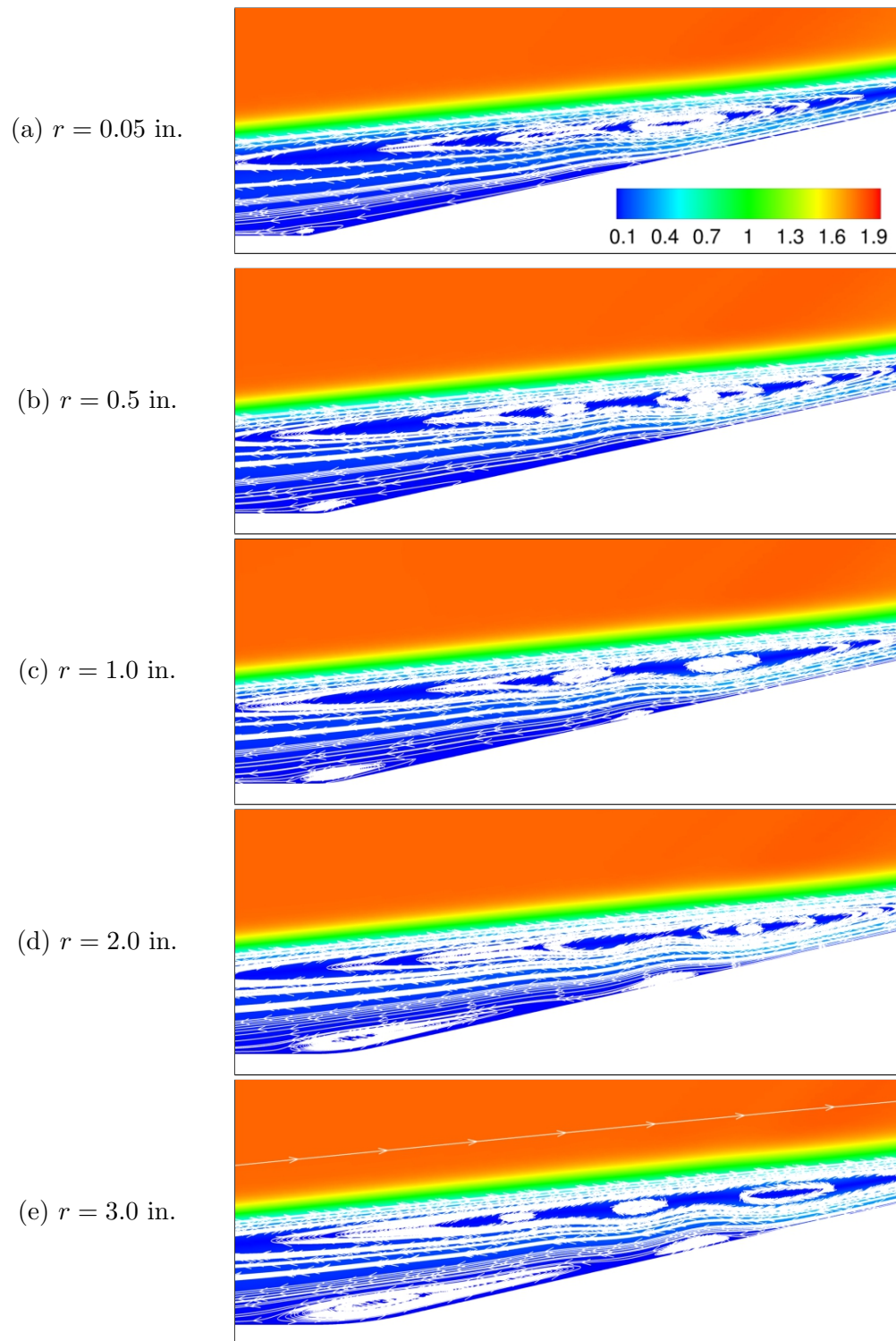


Figure 3.30: Radius of curvature effects ( $Re_L = 110\,000$ ,  $M_\infty = 2$ ).

## CHAPTER 4

### COMPARISON BETWEEN TRIPLE-DECK THEORY AND CFD

In this chapter, a novel comparison between triple-deck theory and numerical solutions to the full set of governing equations will be presented. The comparison will be in terms of the triple-deck scaled variables. It will be shown that scaling the CFD results using the triple deck scalings results in some interesting trends which have not been seen in the literature.

#### 4.1 Scaling of CFD results

In order to compare the triple-deck results to numerical solutions of the full set of governing equations, the CFD results from FUN3D were scaled using the triple-deck scalings. The results are presented in terms of scaled separation point, reattachment point, and overall separation size. The scalings used are as follows:

$$\frac{x'}{L'} = \rho_w^{-1/2} \mu_w^{-1/4} \lambda^{-5/4} \beta^{-3/4} Re_0^{-3/8} x \quad (4.1a)$$

$$\alpha' = \lambda^{1/2} \mu_w^{1/2} \beta^{1/2} Re_0^{-1/4} \alpha \quad (4.1b)$$

where  $(\prime)$  variables are dimensional,  $L'$  is a reference length,  $\rho_w$  and  $\mu_w$  are dimensionless density and viscosity at the wall (dimensionless with respect to  $\rho'_\infty$  and  $\mu'_0$ ),  $\lambda$  is a constant of  $\mathcal{O}(1)$ ,  $\beta \equiv (M_\infty^2 - 1)^{1/2}$ , and  $Re_0$  is

$$Re_0 = \frac{\rho'_\infty U'_\infty L'}{\mu'_0} \quad (4.2)$$

where  $\mu'_0$  is computed using a reference enthalpy of  $U'_\infty$ . The constant,  $\lambda$ , was set to 0.332 for the present work, and the viscosity at the wall was determined using the adiabatic wall temperature and the Sutherland viscosity law [7].

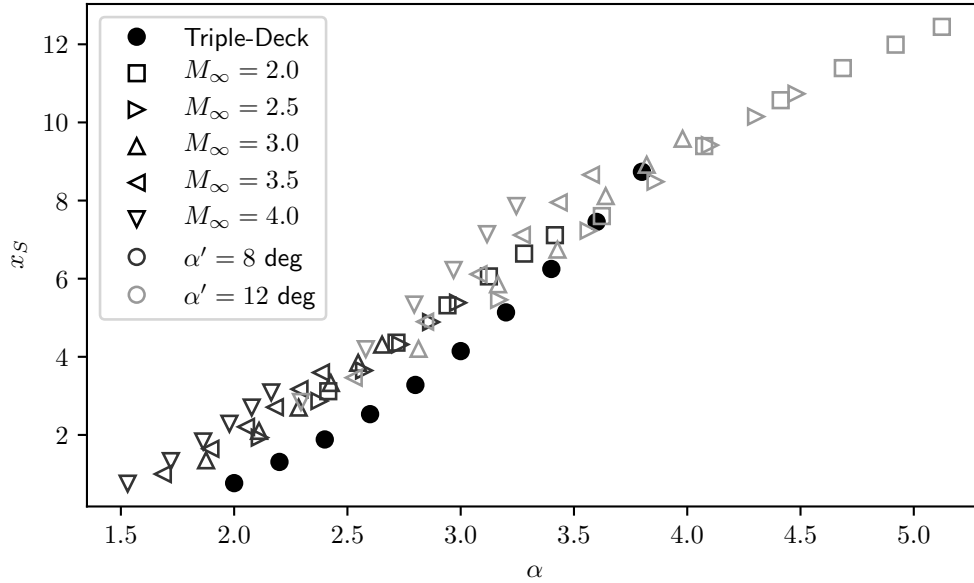


Figure 4.1: Scaled separation point as a function of scaled ramp angle from triple-deck and Navier–Stokes solutions.

#### 4.2 Comparison between triple-deck results and compressible Navier–Stokes results

Figure 4.1 shows a comparison between the scaled separation point from numerical solutions to the triple-deck equations and numerical solutions to the full set of governing equations. Mach number trends are indicated by different symbols, while different ramp angles are indicated by different shades of gray. The figure shows good qualitative agreement between Navier–Stokes solutions and triple-deck solutions. For the triple-deck results, the results are fairly linear below a scaled ramp angle of 2.75 and above a scaled ramp angle of 3.0. There is a noticeable slope change in the triple-deck results at a scaled ramp angle of approximately 2.8. To more clearly show the presence of this trend in the Navier–Stokes solutions, one set of data were plotted against triple-deck results and can be seen in Figure 4.2.

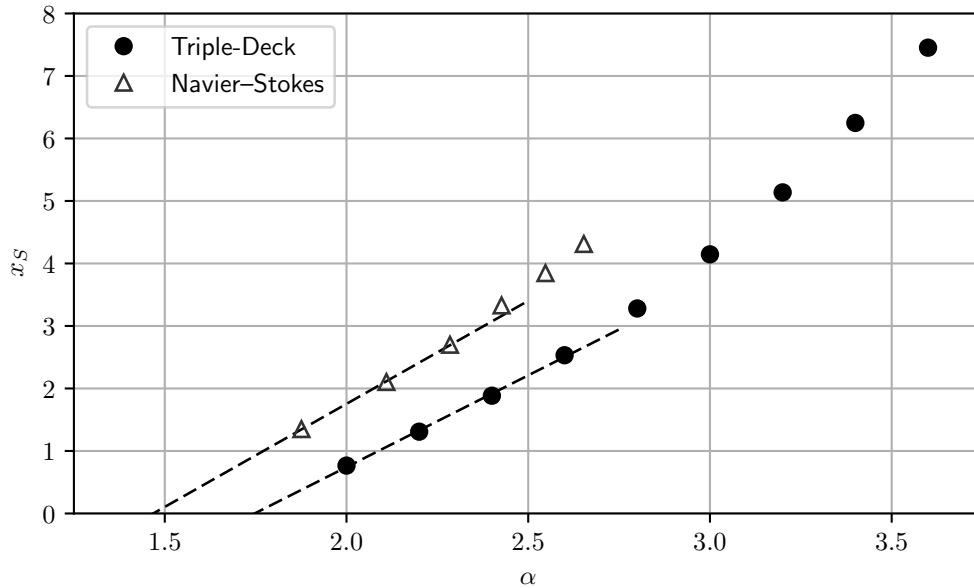


Figure 4.2: Scaled separation point as a function of scaled ramp angle for specific case of  $M_\infty = 3$  and  $\alpha = 8$  degrees.

Figure 4.2 shows Navier–Stokes results for  $M_\infty = 3$ , and  $\alpha = 8$  degrees. The qualitative agreement between the Navier–Stokes results and triple-deck results is more obvious in this figure. Specifically, both data sets show relatively linear trends with a slight change in slope, albeit at different scaled ramp angles.

### 4.3 Incipient separation criterion

The convergence of the linear trends at the lower scaled ramp angles to a single value suggests that the triple-deck scalings can be used to develop a criterion for incipient separation. To accomplish this, an optimization-based approach was used to determine the scaled ramp angle required for incipient separation using numerical

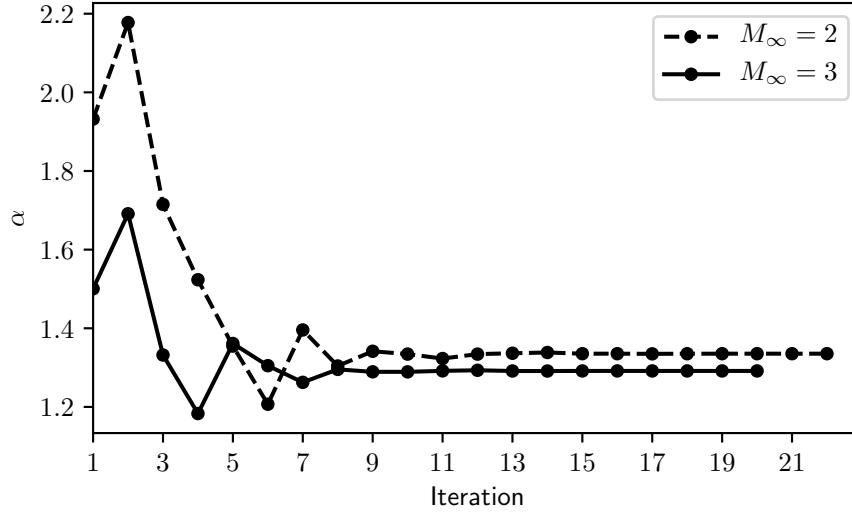


Figure 4.3: Optimizer convergence to incipiently separated conditions.

solutions to the compressible Navier–Stokes equations. The optimization problem was posed as

$$\begin{aligned} & \underset{Re_L}{\text{minimize}} && f(Re_L) \\ & \text{subject to} && 5\,000 \leq Re_L/L \leq 250\,000 \end{aligned}$$

where the objective function was defined as

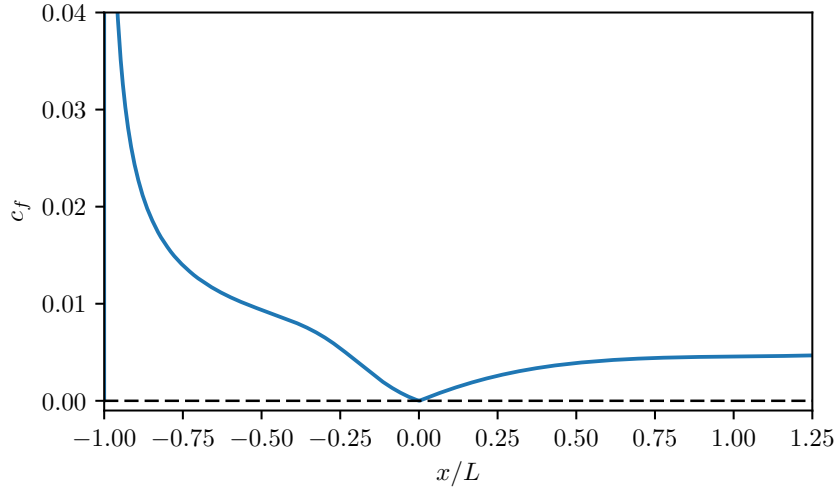
$$f(Re_L) = |\min(c_f(x, Re_L))| \tag{4.3}$$

Each call to the objective function changes the input file for FUN3D, runs the flow solve, extracts the skin friction profile on the wall, and returns the absolute value of the minimum skin friction.

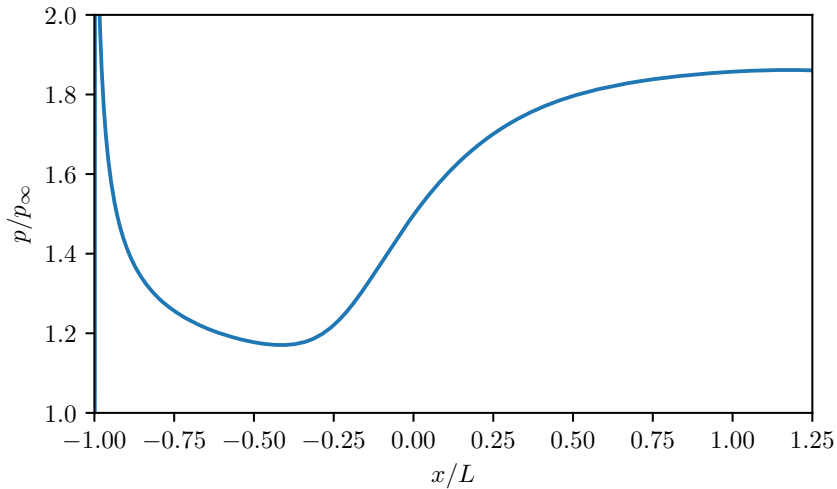
Two cases were run with Mach numbers of 2 and 3 and a physical ramp deflection angle of 8 degrees. Figure 4.3 shows the convergence of the optimization algorithm to the scaled ramp angles required for incipient separation. Each dot on the plot represents a flow solve. The Mach 2 case converged to a scaled ramp angle of 1.3354, while the Mach 3 case converged to a scaled ramp angle of 1.2915. The dif-

ference suggests that there are some Mach number trends in the incipient separation phenomena which are not completely captured by the triple-deck scalings. The final result is

$$\alpha'_{\text{is}} \approx 1.2915 \lambda^{1/2} \mu_w^{1/2} \beta^{1/2} Re_0^{-1/4} \quad (4.4)$$



(a) Skin friction.



(b) Pressure distribution.

Figure 4.4: Skin friction and pressure distribution for incipiently separated conditions at  $M_\infty = 3$  and  $\alpha' = 8$  degrees.



Figure 4.5: Numerical schlieren image of incipient separation conditions ( $M_\infty = 3$ ,  $\alpha = 8$  degrees,  $Re_L = 11\,232$ ).

Figure 4.4 shows the surface pressure distribution and skin friction distribution for the incipiently separated result at  $M_\infty = 3$  for a flow deflection angle of 8 degrees. Figure 4.5 shows a numerical schlieren image for the same case. The skin friction distribution, shown in Figure 4.4(a), shows that the minimum value of the skin friction occurs at the corner, where  $x/L = 0$ , and that it is approximately zero. The pressure distribution lacks the typical pressure plateau which accompanies a separation bubble, as expected.

#### 4.4 Comparison with existing criteria

In previous studies, Inger developed a triple-deck-based criterion and compared it to existing criteria [48]. It was shown in chapter 2 that the scaled ramp angle required for incipient separation was approximately 1.8226, which is higher than the value of 1.57 quoted by Inger [31]. Chapman, et al., developed a pressure-based correlation for incipient separation based on experimental data [13]. In the present

section, the developed criterion will be compared against the aforementioned criteria by Inger and Chapman, et al.

The correlation by Inger is

$$C_p = \left[ \left( \frac{T_{\text{ref}}}{T_\infty} \right) Re_L (M_\infty^2 - 1) \right]^{-1/4} \quad (4.5)$$

where  $T_{\text{ref}}$  is a characteristic boundary-layer reference temperature which can be attributed to Eckert [49]. The correlation by Chapman, et al., is

$$C_p = 0.093 [(M_e^2 - 1)Re]^{-1/4} \quad (4.6)$$

The newly developed criterion requires some modification in order to allow for comparison with pressure-based criterion because it is written in terms of the deflection angle required to produce incipient separation, not pressure. However, at incipiently separated conditions, there is no noticeable separation shock or reattachment shock (see Figure 4.5). As such, the deflection angle is related to the pressure across the shock wave using the traditional relations from inviscid gas dynamics. Doing so yields

$$C_p = \frac{2}{\gamma M_\infty^2} \left[ \frac{p}{p_\infty} (\alpha'_{\text{is}}(Re_L, M_\infty), M_\infty) - 1 \right] \quad (4.7)$$

where  $\alpha'_{\text{is}}$  represents the ramp deflection angle required for incipient separation as determined by (4.4). Figure 4.6 shows a comparison between the three criteria for different Mach and Reynolds numbers. All three correlations agree that as the Reynolds number increases, the pressure required to produce incipient separation decreases. According to Babinsky, this trend reverses above  $Re_\delta \approx 10^5$  [7]. Increasing Mach number also decreases the pressure ratio required to produce incipient separation. There is good qualitative agreement amongst the three criteria. However, the triple-deck-based correlation does not decay the same as the correlations by Inger

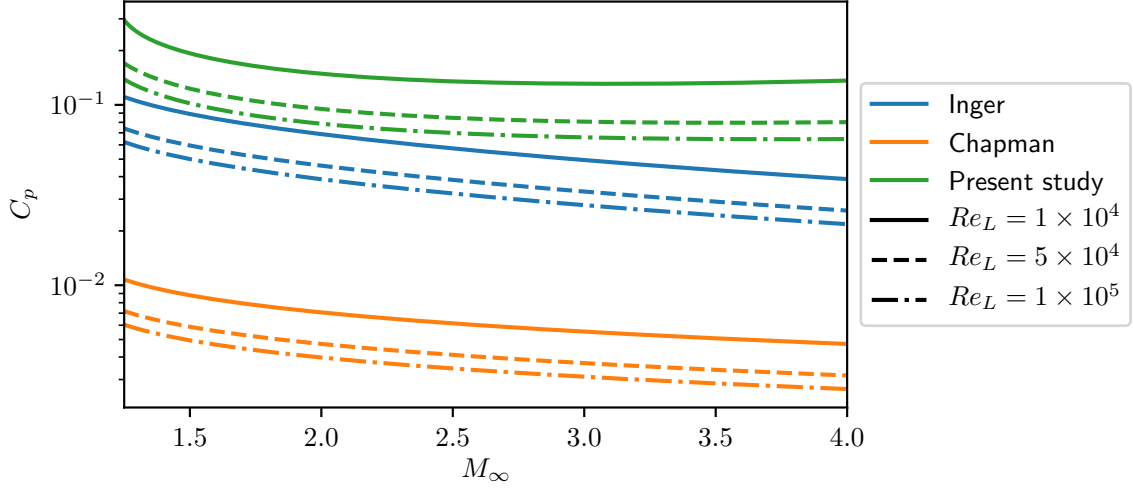


Figure 4.6: Comparison between correlations for incipient separation based on pressure coefficient.

and Chapman. Both of the existing correlations have the same functional dependence upon Reynolds number and Mach number. That is,

$$C_p \propto [Re_L(M_\infty^2 - 1)]^{-1/4} \quad (4.8)$$

This suggests that as the Mach number increases, the pressure ratio required to produce incipient separation decreases. The triple-deck-based correlation for the scaled ramp angle required to produce incipient separation is

$$\alpha'_{is} \propto (M_\infty^2 - 1)^{1/4} Re_0^{-1/4} \quad (4.9)$$

which implies that the deflection angle required to produce incipient separation increases as the Mach number increases. Maintaining the same Reynolds number and increasing the deflection angle increases the pressure ratio across the shock wave. This is an interesting finding which requires further investigation. One way to investigate the trends would be to use the optimization-based method described in the previous

section to compute the conditions necessary for incipient separation over a range of Mach and Reynolds numbers.

## CHAPTER 5

### THREE-DIMENSIONAL NUMERICAL SOLUTIONS

In this chapter, results from three-dimensional solutions to the compressible Navier-Stokes equations are presented. Results are compared against two-dimensional results from previous chapters and experimental results. The motivation for the three-dimensional numerical solutions is to investigate when the nominally two-dimensional shock wave/boundary layer interaction becomes three-dimensional and unsteady. A single case with a freestream Mach number of 2 and a radius of curvature of 4 inches was selected for the unsteady flow solves. This case was selected because of the numerous features inside the separated region. What follows is a discussion of the mesh generation process, validation via a mesh-independence study, selection of the time step, and unsteady, three-dimensional results.

#### 5.1 Mesh generation and boundary conditions

The meshing process was automated using Pointwise Glyph scripting. A sample mesh<sup>1</sup> can be seen in Figure 5.1. Figure 5.2 shows the boundary meshes excluding the closest domains for the sake of clarity. The inlet, left-most, and upper domains were set to a freestream boundary condition. The blue boundary is set to extrapolate for supersonic flow and back pressure for subsonic flow. The far side wall boundary is marked in red. The side wall boundaries were set to inviscid walls. The short orange portion represents an inviscid wall. The green portion is the flat plate and ramp and was set to an adiabatic, no-slip wall boundary condition.

---

<sup>1</sup>Only every third point is shown for clarity.

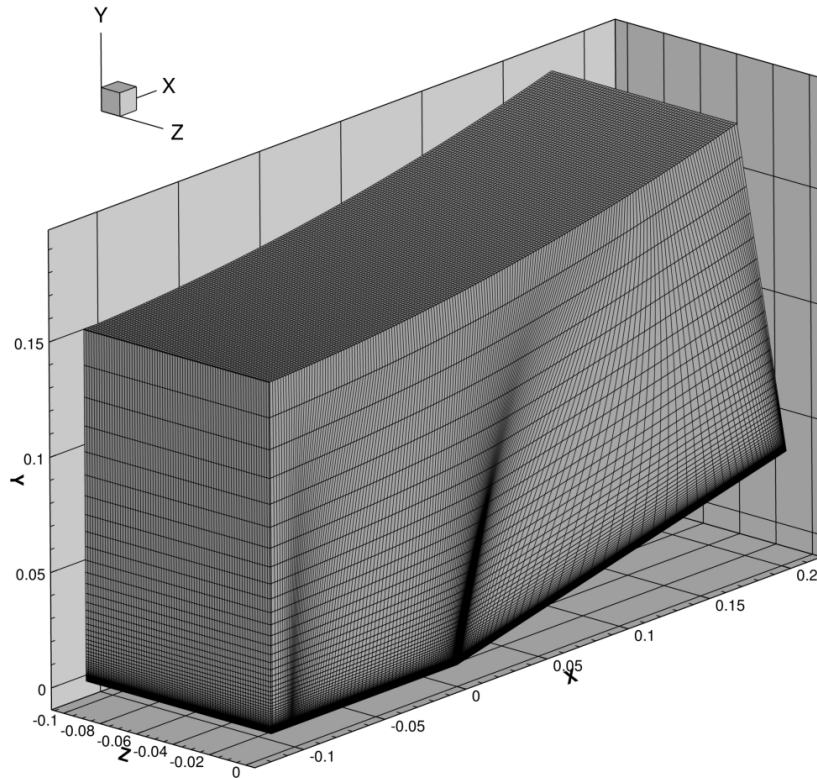


Figure 5.1: Sample three-dimensional mesh (every third point shown).

## 5.2 Validation

A mesh-independence study was undertaken to determine the mesh resolution required to resolve the shock wave/boundary layer interaction. The results are compared against the two-dimensional results from Chapter 3 and the experimental data from Sfeir [2]. Pressure and skin friction distributions were extracted at the middle of the span.

Figure 5.3 shows a comparison between wall pressure distributions from two- and three-dimensional numerical solutions to the compressible Navier–Stokes equations and the experiments of Sfeir [2]. The pressure distributions for mesh resolution levels 2-4 collapse into what is essentially one curve which indicates mesh indepen-

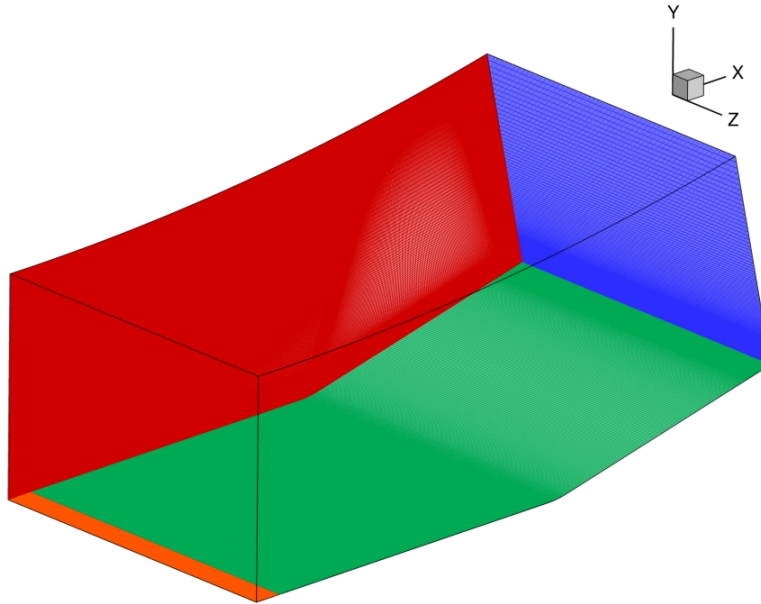


Figure 5.2: Schematic of mesh boundaries.

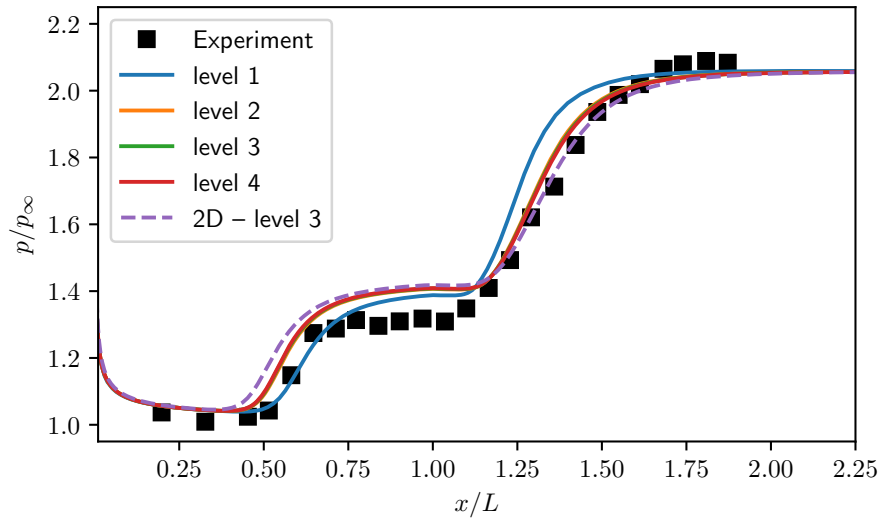


Figure 5.3: Surface pressure distribution comparison between 2D/3D numerical results and experimental results from Sfeir [2].

dence. This conclusion is further reinforced by Figure 5.4 which shows the total size of the separated region as a function of the number of nodes in the mesh. Increasing

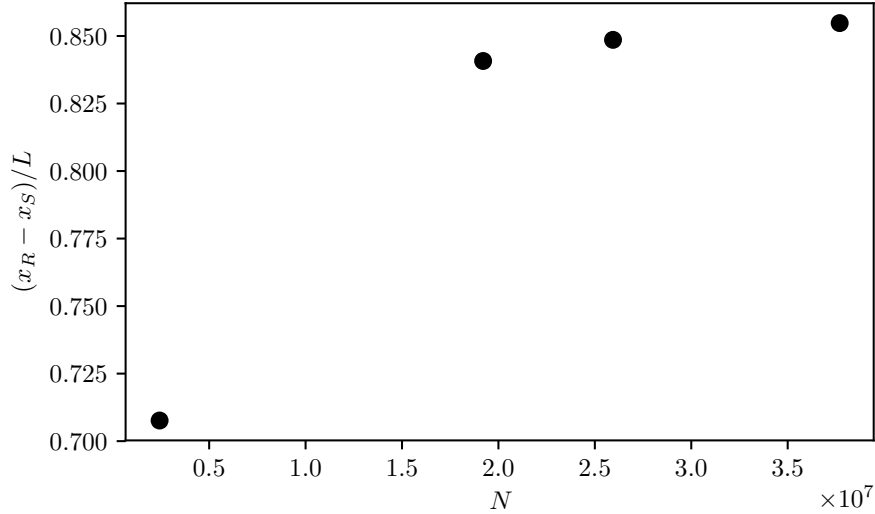


Figure 5.4: Size of separated region versus number of nodes in the mesh for three-dimensional numerical solutions.

Table 5.1: Details of meshes used in mesh-independence study.

Level	Dimensions ( $i \times j \times k$ )
1	$243 \times 100 \times 100$
2	$485 \times 199 \times 199$
3	$536 \times 220 \times 220$
4	$608 \times 249 \times 249$

the mesh resolution higher than level 2 has relatively little effect on the overall size of the separated region. For this reason, the level 3 mesh was selected for the unsteady flow solves. The mesh dimensions in each direction along with the total number of nodes are shown in Table 5.1. Robinet used mesh dimensions of  $600 \times 180 \times 60$  for his study, comparable to the level 3 mesh used in the present study which has dimensions of  $536 \times 220 \times 220$ .

Figure 5.5 shows results from the three-dimensional numerical solutions for Sfier’s case in the form of a slice taken at the midspan of the ramp. The separation and reattachment shocks are evident, as is the separated region (i.e., the blue region).

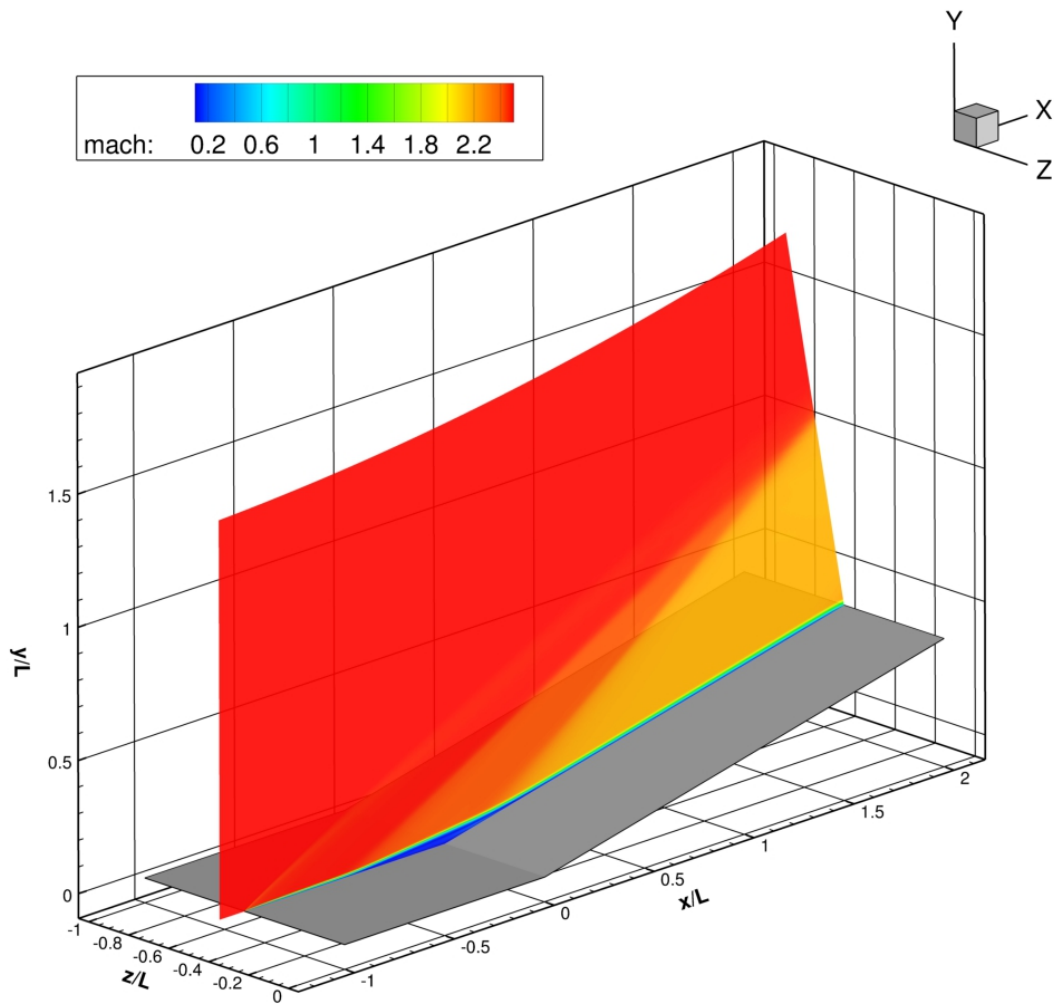


Figure 5.5: Slice showing contours of Mach number for Sfeir's case.

Figure 5.6 shows the residual convergence for the case shown in Figure 5.5. The inviscid terms were set to first order accuracy for the first 5000 iterations. The flow solver residuals converged to at least  $1 \times 10^{-12}$  by roughly 4200 iterations, after which the spatial accuracy was switched to second-order, as indicated by the spike in the residual values. Around 6000 iterations, oscillations become evident in the residuals which are indicative of flux limiter buzz. The flux limiters are frozen after 5000 second-order accurate iterations. This allowed the residuals to converge further

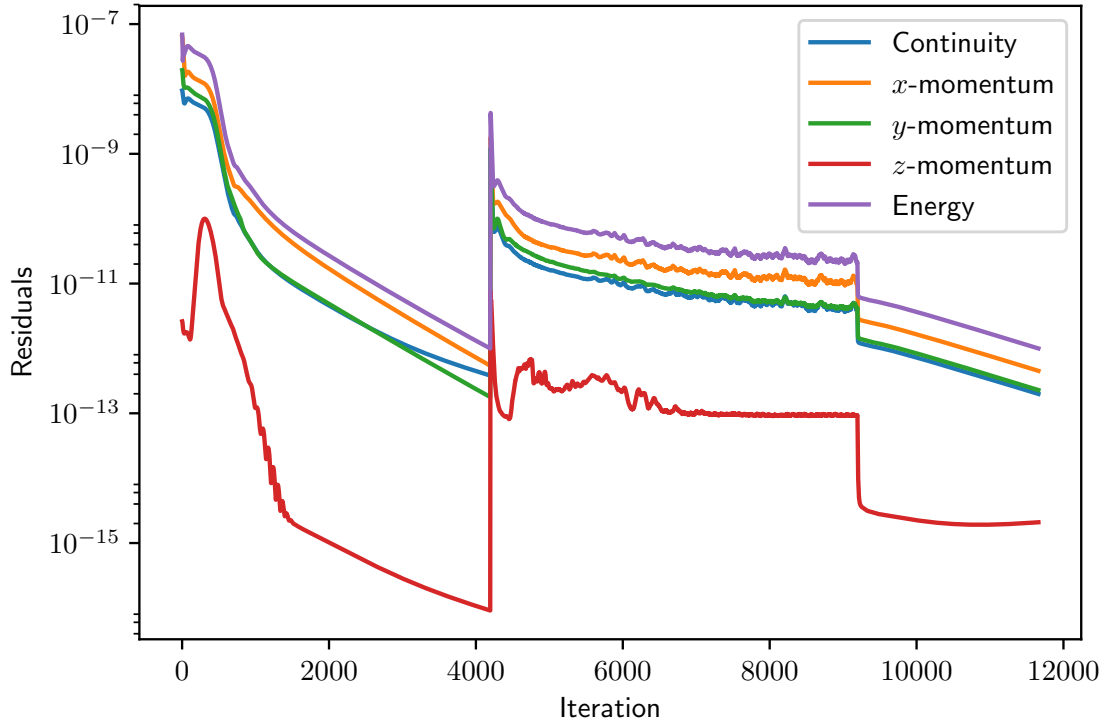


Figure 5.6: Residual convergence for the level 3 mesh.

so that all were below  $1 \times 10^{-12}$ . The convergence of the residuals suggests that the case studied by Sfeir is indeed steady.

For Sfeir’s case, the flat plate was only 4 inches long. In order to facilitate a proper comparison between the two- and three-dimensional results, the flat plate portion was lengthened to 12 inches, identical to what was used for the 12 degree ramp in Chapter 3. The spatial resolution determined in the mesh-independence study was enforced which resulted in a mesh with dimensions of  $852 \times 263 \times 220$ , which corresponds to a mesh with approximately 49.3 million nodes.

### 5.3 Numerical solution procedure

The dimensionless form of the compressible Navier–Stokes equations were numerically solved using FUN3D. The relevant features of FUN3D have been discussed in Chapter 3. The main difference between the previous two-dimensional flow solves and the flow solves accomplished for the present chapter is how time advancement was accomplished. Up to this point, only the steady-state flow solver has been used. This means that local time stepping and other solution acceleration methods were used to aid in the convergence to steady-state. As such, the steady-state flow solves were not time-accurate. In what follows, the flow solver is run in time-accurate mode, using an implicit optimized second-order backward difference formula [36].

We now turn to selection of the time step used in the numerical scheme. According to Robinet, the global instabilities of interest usually have relatively low frequencies which correspond to timescales of  $\mathcal{O}[10^{-5}]$  seconds [47]. Robinet used a time step of  $6.82 \times 10^{-6}$  [47]. In the present work, a characteristic time was estimated using the length of the flat plate and the freestream velocity (i.e.,  $t_{\text{char}} = L/U_\infty$ ). The result is a characteristic time of  $7.213 \times 10^{-4}$ . A physical timestep of  $3 \times 10^{-6}$  seconds was used to ensure that the relevant temporal phenomena were being captured.

### 5.4 Unsteady results

A single case with  $r = 4$  in.,  $Re_L = 200\,000$ , and  $M_\infty = 2$  was chosen for further investigation because of the multiple features inside the separated region. The case was run for approximately 1200 timesteps on 672 processors on the TACC Lonestar 5 cluster, which required approximately 120 hours.

Wall pressures were extracted along a midspan slice at locations of  $x/L = -0.1$ ,  $-0.05$ , and  $0.1$ . The location of the slice is indicated by the gray line shown

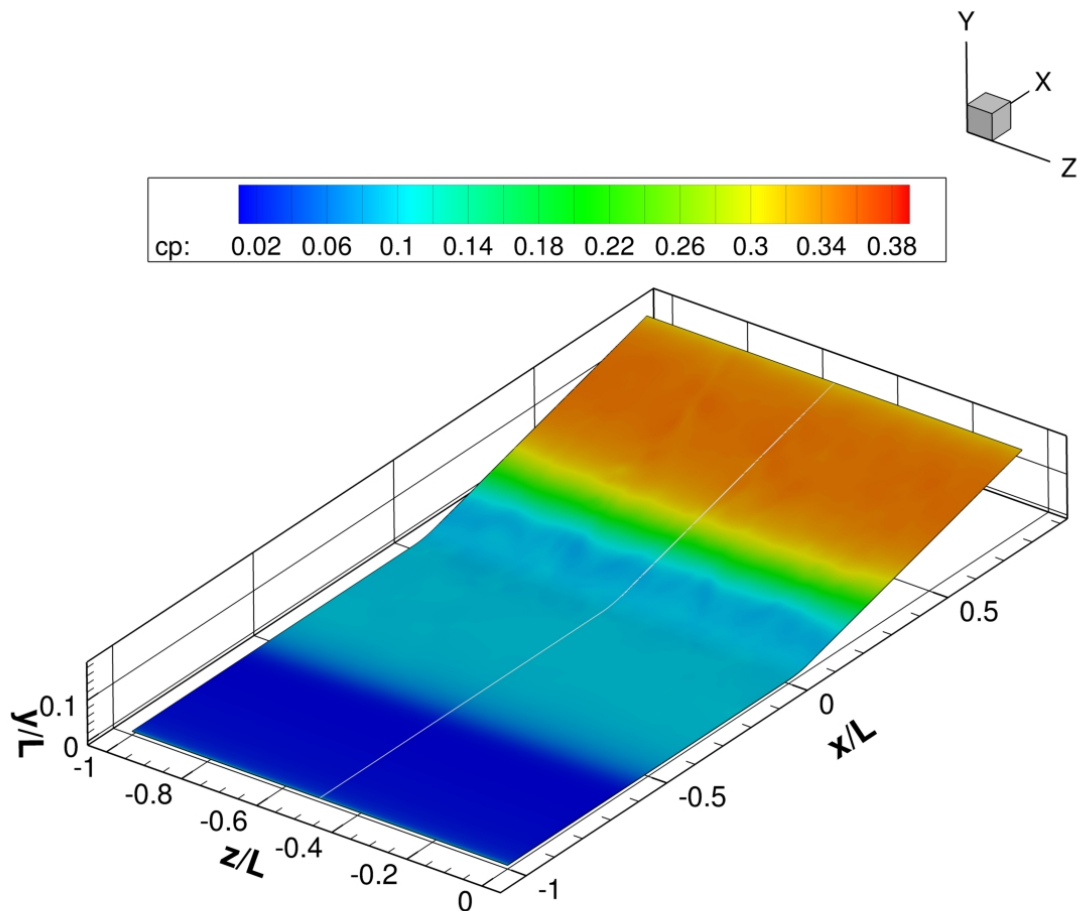
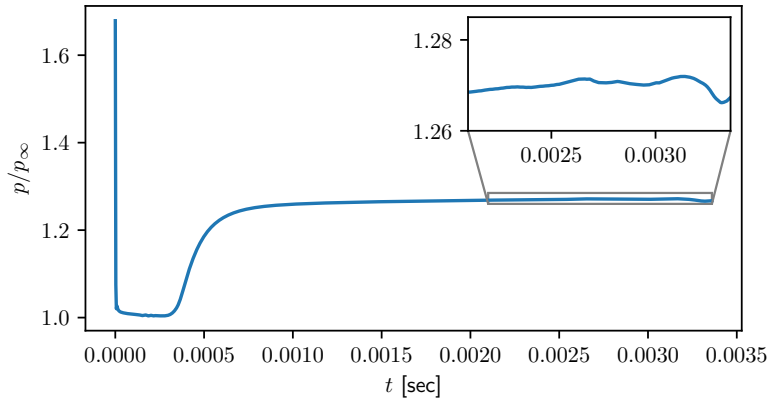
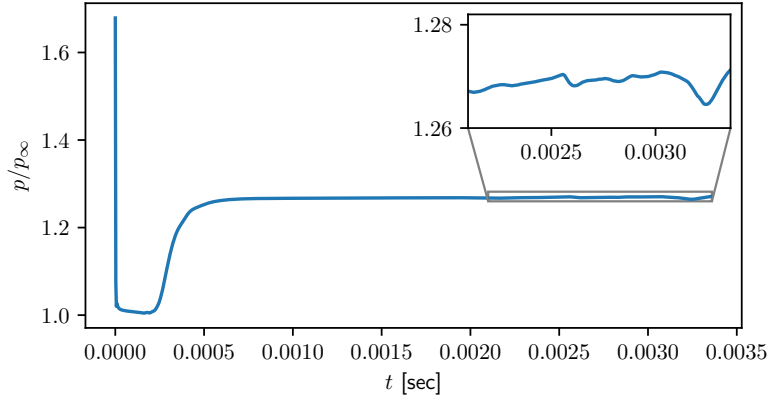


Figure 5.7: Schematic of locations at which wall pressures were extracted.

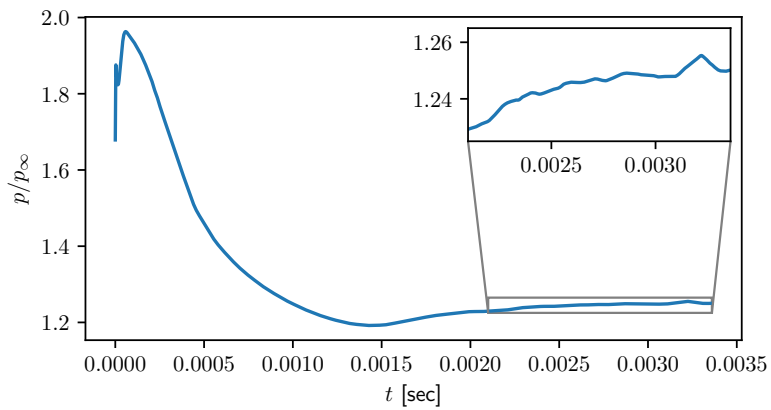
in Figure 5.7. Figure 5.8 shows plots of these wall pressures as a function of time. A quick examination of the figures suggests that the flow has reached steady-state. However, as shown by the zoomed inset plots, there are still fluctuations in pressure at the various locations, which suggests there are some spatio-temporal phenomena occurring.



(a)  $x/L = -0.1$ .



(b)  $x/L = -0.05$ .



(c)  $x/L = 0.1$ .

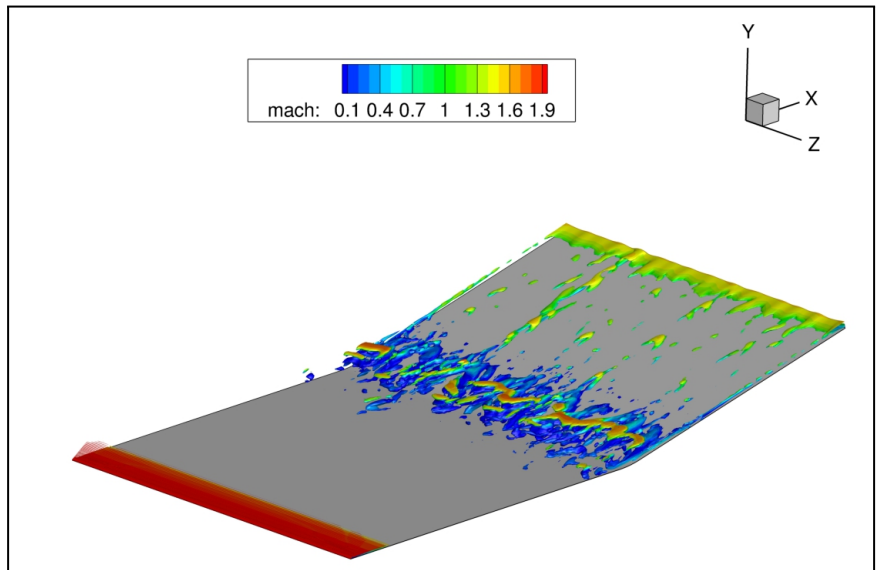
Figure 5.8: Wall pressure time history at different streamwise locations at the middle of the span.

Isosurfaces of  $Q$ -criterion, colored by Mach number, were plotted at different instances in time and are shown in Figure 5.9. Mathematically, the  $Q$ -criterion is the second invariant of the velocity gradient tensor,  $\nabla\mathbf{u}$ , or  $u_{i,j}$  [50]. Close examination of the figure reveals a complex flowfield inside and downstream of the separated region. The flow field qualitatively appears to be either transitional or turbulent. Another interesting feature is the presence of streamwise features evident in the isosurface near reattachment. These features may be the beginnings of Görtler vortices.

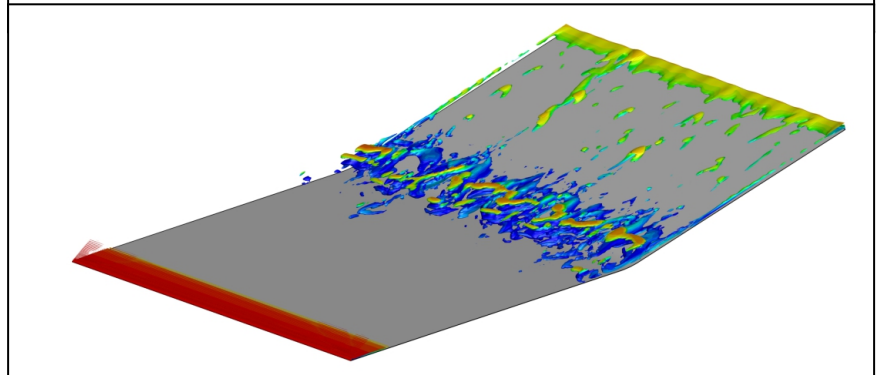
To ensure that the present unsteady results were not the result of starting transients in the flow solver, the same case was run using the steady solver in FUN3D. If the flow is actually steady, this fact should be reflected in the residual convergence. Two cases with Reynolds number based on flat plate length of 170 000 and 200 000 were solved using FUN3D. The resulting residual convergence histories can be seen in Figure 5.10. Both cases show oscillatory behavior, although the oscillations are higher frequency for the  $Re_L = 170\,000$  case.

No efforts were undertaken to ensure that all the relevant scales were resolved for a turbulent flow. As such, if the present case is actually transitional or turbulent, the results cannot be discussed in a physically meaningful way. Although this flow is likely transitional or turbulent, the unsteady, three-dimensional numerical solutions still serve a purpose in that they suggest that the two-dimensional numerical simulations are not capable of capturing the unsteady behavior of the shock wave/boundary-layer interaction at the higher Reynolds numbers presented in this study.

(a) Time step 1080.



(b) Time step 1100.



(c) Time step 1120.

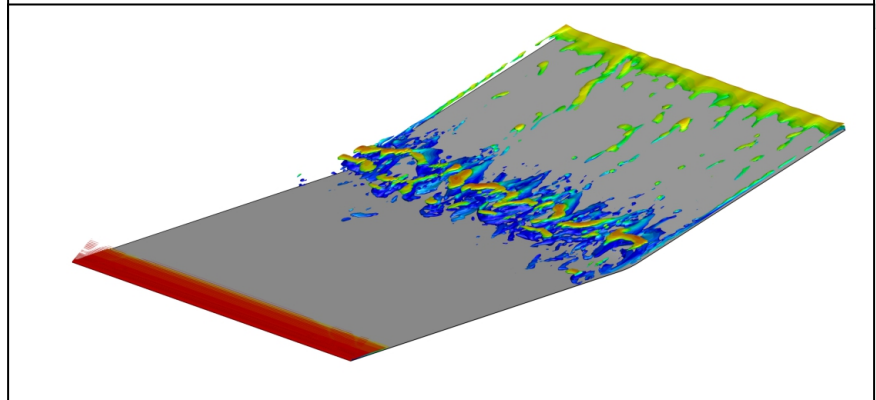


Figure 5.9: Isosurfaces of  $Q$ -criterion colored by Mach number at different instances in time.

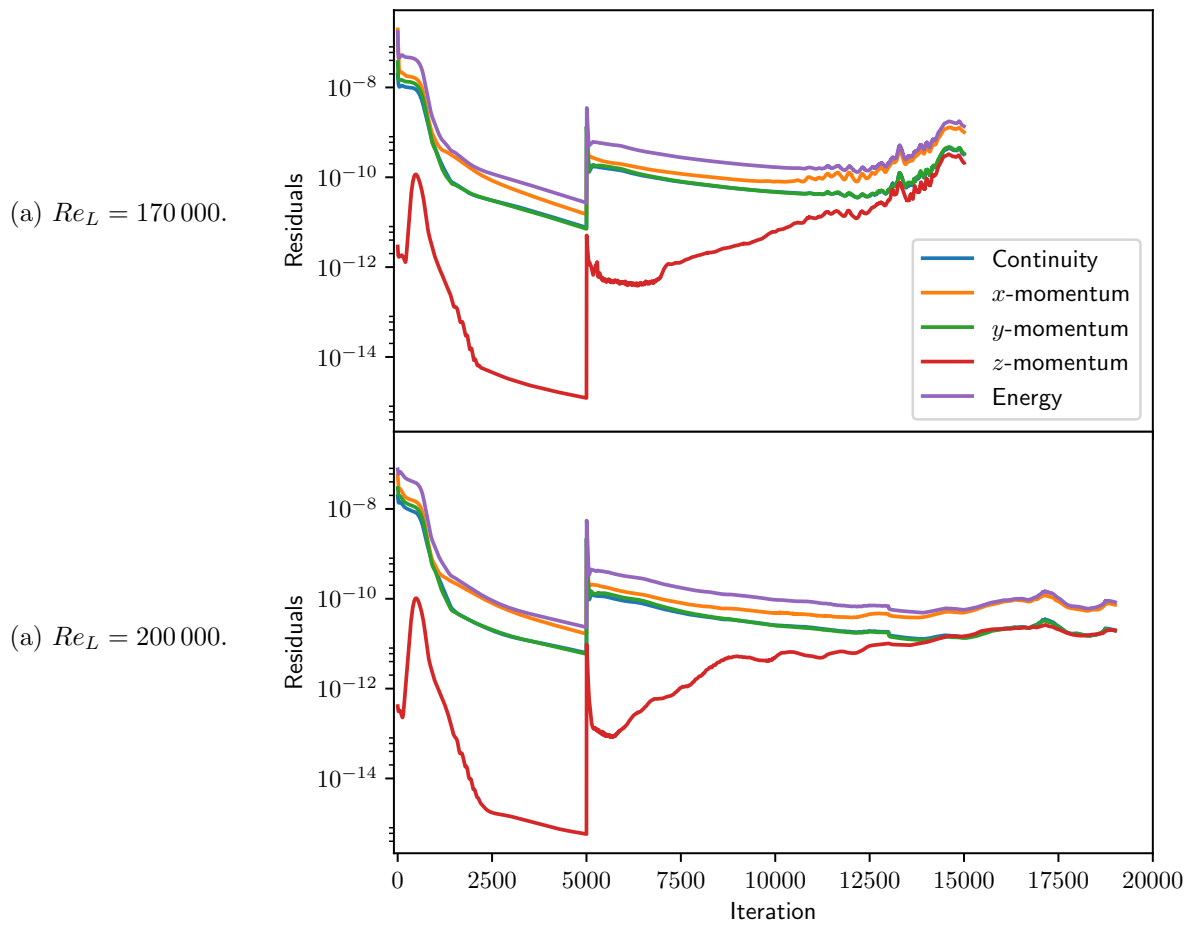


Figure 5.10: Comparison of residual convergence for steady-state numerical solutions with different Reynolds numbers.

## CHAPTER 6

### CONCLUDING REMARKS

#### 6.1 Summary

The goal of the present work was to improve the physical understanding of radius of curvature effects in shock wave/boundary layer interactions. This task has been accomplished via a joint computational and analytical approach (i.e., numerical solutions of the compressible Navier–Stokes equations and triple deck theory). New findings have been presented, namely, the linear trends in the separation point at low scaled ramp angle for CFD and triple deck results. Beyond this discovery, it was found that several small features appear inside the separated region at low Mach numbers. The number of features inside the separated region was determined to be a function of Mach number, Reynolds number and radius of curvature, with the effects of each parameter being discussed. A new, free-interaction theory-based scaling relationship was developed. This scaling relationship provides a convenient way to represent Mach, Reynolds and radius of curvature effects in a single curve for each flow deflection angle. Three-dimensional steady and unsteady numerical solutions of the compressible Navier–Stokes equations were sought with the purpose of exploring when the nominally steady, two-dimensional SBLI becomes unsteady and three dimensional. It was found that two-dimensional numerical solutions are not necessarily capable of capturing the transient behavior of the SBLIs at the higher Reynolds numbers used in the present study (i.e.  $Re_L \approx 200\,000$ ).

## 6.2 Future work

The scaling relationship which relates Mach number, Reynolds number, and radius of curvature was developed based on free interaction theory which was derived for a flat plate. It would be interesting to develop a new relationship for curved surfaces by writing the Navier–Stokes equations in a curvilinear coordinate system (polar coordinates for the case of a circular arc), and applying boundary layer assumptions and order of magnitude analysis, followed by applying the streamwise momentum equation at the wall. In this way, it might be possible to develop a more physically meaningful scaling relationship for interactions over a curved surface.

As shown in the previous chapter, the flow becomes unsteady at the higher Reynolds numbers. This unsteadiness may be related to an instability which arises as the Reynolds number increases. It would be interesting to run more unsteady flow solves to determine at what Reynolds number the flow becomes unsteady and three-dimensional. It would also be interesting to apply relatively new methods from stability analysis to find the most unstable mode and find the wave maker (i.e., the region where perturbations are amplified the most). There is also the possibility of applying transient growth analysis to the present case.

## APPENDIX A

### Upstream influence length calculation

In this appendix, the method used to find the upstream influence will be explained. The method is based on edge-detection algorithms from the field of image processing.

The upstream influence length,  $L_0$ , can be defined as the distance between the point where the pressure rise due to the shock wave begins and the location where the pressure rise would occur if the flow were inviscid<sup>1</sup>. The goal is to be able to automatically identify upstream influence, rather than undertaking the tedious task of visually inspecting the pressure distributions for each case. This problem can essentially be thought of as a one-dimensional edge-detection problem.

One approach to edge detection involves convolving the derivative of the discrete Gaussian distribution. The discrete Gaussian distribution is

$$g[n] = \frac{1}{\sqrt{2\pi}\sigma} \exp\left[\frac{-n^2}{2\sigma^2}\right], \quad (\text{A.1})$$

where  $\sigma$  is the standard deviation. Taking the derivative with respect to  $n$ ,

$$h[n] = \frac{dg}{dn} = \frac{-n}{\sqrt{2\pi}\sigma^3} \exp\left[\frac{-n^2}{2\sigma^2}\right]. \quad (\text{A.2})$$

Now, convolving (A.2) with the surface pressure distribution yields the signal seen in Figure A.1, where the convolution may be written as

$$y[n] = \sum_{k=0}^{N-1} h[n-k]p[k], \quad (\text{A.3})$$

where  $p[n]$  is the surface pressure distribution written in discrete form,  $h[n]$  is the derivative of the discrete Gaussian distribution,  $y[n]$  is the convolved signal, and  $N$  is the total number of points in the sequence,  $h[n]$ . The peaks in the plot correspond to the pressure rises from the shock waves in the pressure distribution. Therefore, identifying the locations of the peaks allows the  $x$ -coordinates of the pressure rises to

---

<sup>1</sup>See Chapter 1 for more information.

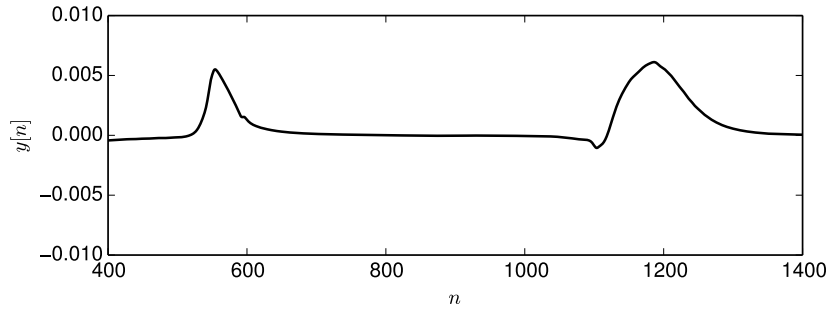


Figure A.1: Convolved signal.

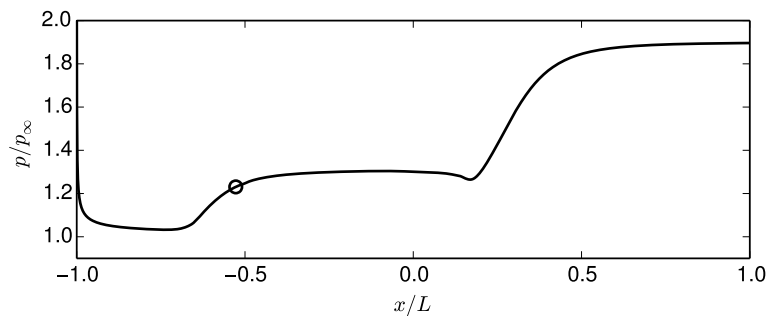


Figure A.2: Initial upstream influence point.

be determined. After finding the locations of the pressure rises, and restricting the range of values to  $-4/5 \leq x/L \leq 0.0$ , the point lies essentially in the middle of the pressure rise due to the separation shock (see Figure A.2).

Now, the point is “relaxed” until the slope of the pressure distribution is below some desired tolerance. The tolerance in the present work was set to  $1 \times 10^{-3}$ . The resulting upstream influence can be seen in Figure A.3.

This method was implemented using the Python scripting language so that the upstream influence length can be identified automatically using the surface pressure distribution from any data source (e.g., experiments or CFD).

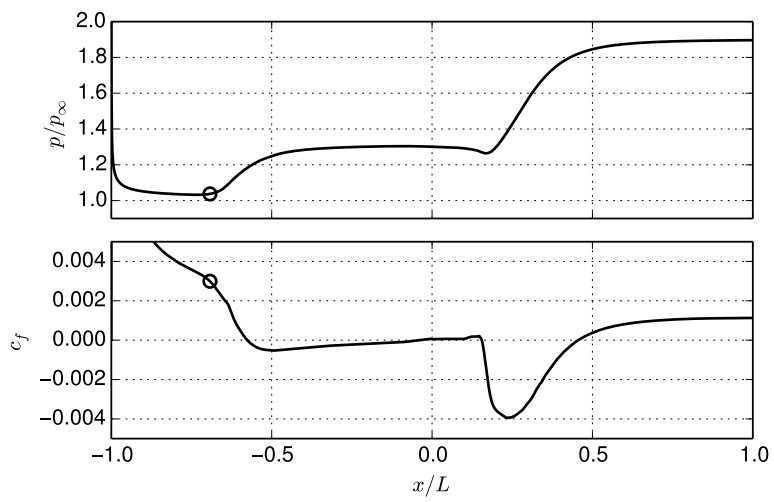


Figure A.3: Sample upstream influence location.

## Bibliography

- [1] K. W. Cassel, A. I. Ruban, and J. D. A. Walker, “An instability in supersonic boundary-layer flow over a compression ramp,” *Journal of Fluid Mechanics*, vol. 300, pp. 265–285, 1995.
- [2] A. A. Sfeir, “Supersonic laminar boundary layer separation near a compression corner,” Ph.D. dissertation, University of California, Berkeley, 1969.
- [3] D. S. Dolling, “Fifty years of shock-wave/boundary-layer interaction research: What next?” *AIAA Journal*, vol. 39, no. 8, pp. 1517–1531, 2001.
- [4] D. V. Gaitonde, “Progress in shock wave/boundary layer interactions,” *Progress in Aerospace Sciences*, vol. 72, pp. 80 – 99, 2015.
- [5] G. S. Settles, S. M. Bogdonoff, and I. E. Vas, “Incipient separation of a supersonic turbulent boundary layer at high Reynolds numbers,” *AIAA Journal*, vol. 14, no. 1, pp. 50–56, 1976.
- [6] J. Délerly and J. G. Marvin, “AGARDograph 280: Turbulent shock-wave boundary layer interaction,” AGARD, 1986.
- [7] H. Babinsky and J. K. Harvey, *Shock Wave–Boundary Layer Interactions*. Cambridge University Press, 2011.
- [8] K. Stewartson and P. Williams, “Self-induced separation,” *Proceedings of the Royal Society of London*, vol. 312, pp. 181–206, 1969.
- [9] M. J. Lighthill, “On boundary layers and upstream influence. I. A comparison between subsonic and supersonic flows,” *Proceedings of the Royal Society of London*, vol. 217, no. 1130, pp. 344–357, 1953.

- [10] S. Goldstein, “On laminar boundary-layer flow near a position of separation,” *The Quarterly Journal of Mechanics and Applied Mathematics*, vol. 1, no. 1, pp. 43–69, 1948.
- [11] M. J. Lighthill, “On boundary layers and upstream influence. II. Supersonic flows without separation,” *Proceedings of the Royal Society of London*, vol. 217, no. 1131, pp. 478–507, 1953.
- [12] —, “Upstream influence in boundary layers 45 years ago,” *Philosophical Transactions of the Royal Society of London A: Mathematical, Physical and Engineering Sciences*, vol. 358, no. 1777, pp. 3047–3061, 2000.
- [13] D. R. Chapman, D. M. Kuehn, and H. K. Larson, “Investigation of separated flows in supersonic and subsonic streams with emphasis on the effect of transition,” NACA, Tech. Rep. 1356, 1958.
- [14] A. Sansica, N. D. Sandham, and Z. Hu, “Forced response of a laminar shock-induced separation bubble,” *Physics of Fluids*, vol. 26, no. 9, 2014.
- [15] F. T. Smith and A. F. Khorrami, “The interactive breakdown in supersonic ramp flow,” *Journal of Fluid Mechanics*, vol. 224, pp. 197–215, 1991.
- [16] G. L. Korolev, J. S. B. Gajjar, and A. I. Ruban, “Once again on the supersonic flow separation near a corner,” *Journal of Fluid Mechanics*, vol. 463, pp. 173–199, 2002.
- [17] G. R. Inger, “On the curvature of compressible boundary layer flows near separation,” *Journal of Applied Mathematics and Physics*, vol. 28, pp. 1027–1035, 1977.

- [18] —, “Transonic shock-turbulent boundary layer interaction and incipient separation on curved surfaces,” in *AIAA 14th Fluid and Plasma Dynamics Conference*, 1981, AIAA 81-1244.
- [19] W. B. Sturek and J. E. Danberg, “Supersonic turbulent boundary layer in adverse pressure gradient. Part II: Data analysis,” *AIAA Journal*, vol. 10, no. 5, pp. 630–635, 1972.
- [20] —, “Supersonic turbulent boundary layer in adverse pressure gradient. Part I: The experiment,” *AIAA Journal*, vol. 10, no. 4, pp. 475–480, 1972.
- [21] J. F. Donovan, E. F. Spina, and A. J. Smits, “The structure of a supersonic turbulent boundary layer subjected to concave surface curvature,” *Journal of Fluid Mechanics*, vol. 259, pp. 1–24, 1994.
- [22] C. Wang, “The effects of curvature on turbulent mixing layers,” Ph.D. dissertation, California Institute of Technology, 1984.
- [23] V. Y. Neiland, “Theory of laminar boundary layer separation in supersonic flow,” *Fluid Dynamics*, vol. 4, no. 4, pp. 33–35, 1969.
- [24] M. V. Dyke, *Perturbation Methods in Fluid Mechanics*. Academic Press, 1964.
- [25] J. Cousteix and J. Mauss, *Asymptotic Analysis and Boundary Layers*. Springer-Verlag, 2007.
- [26] V. V. Sychev, A. I. Ruban, V. V. Sychev, and G. L. Korolev, *Asymptotic Theory of Separated Flows*, A. F. Messiter and M. V. Dyke, Eds. Cambridge University Press, 1998.

- [27] D. P. Rizzetta, O. R. Burggraf, and R. Jenson, “Triple-deck solutions for viscous supersonic and hypersonic flow past corners,” *Journal of Fluid Mechanics*, vol. 89, pp. 535–552, 1978.
- [28] M.-K. Huang and G. R. Inger, “Application of the triple-deck theory of viscous-inviscid interaction to bodies of revolution,” *Journal of Fluid Mechanics*, vol. 129, pp. 427–441, 1983.
- [29] G. Mengaldo, M. Kravtsova, A. I. Ruban, and S. J. Sherwin, “Triple-deck and direct numerical simulation analyses of high-speed subsonic flows past a roughness element,” *Journal of Fluid Mechanics*, vol. 774, pp. 311–323, 2015.
- [30] T. M. A. El-Mistikawy, “Separation prevention as an indirect problem based on the triple-deck theory,” *AIAA Journal*, vol. 32, no. 7, pp. 1423–1427, 1994.
- [31] G. R. Inger, “Theory of local heat transfer in shock/laminar boundary-layer interactions,” *Journal of Thermophysics and Heat Transfer*, vol. 12, no. 3, pp. 336–342, 1998.
- [32] F. T. Smith, “On the non-parallel flow stability of the Blasius boundary layer,” *Proceedings of the Royal Society of London A*, vol. 366, no. 1724, pp. 91–109, 1979.
- [33] O. S. Ryzhov, “Triple-Deck Instability of Supersonic Boundary Layers,” *AIAA Journal*, vol. 50, no. 8, pp. 1733–1741, 2012.
- [34] A. I. Ruban, “Numerical solution of the local asymptotic problem of the unsteady separation of a laminar boundary layer in supersonic flow,” *USSR Computational Mathematics and Mathematical Physics*, vol. 18, no. 5, pp. 175–187, 1978.

- [35] W. K. Anderson, J. C. Newman, and S. L. Karman, “Stabilized finite elements in FUN3D,” in *55th AIAA Aerospace Sciences Meeting*, 2017, AIAA 2017-0077.
- [36] R. T. Biedron, J. M. Derlaga, P. A. Gnoffo, D. P. Hammond, W. T. Jones, B. Kleb, E. M. Lee-Rausch, E. J. Nielsen, M. A. Park, C. L. Rumsey, J. L. Thomas, and W. A. Wood, *FUN3D Manual: 12.4*, NASA-TM-2014-218179, 2014.
- [37] W. K. Anderson and D. L. Bonhaus, “An implicit upwind algorithm for computing turbulent flows on unstructured grids,” *Computers and Fluids*, vol. 23, no. 1, pp. 1–21, 1994.
- [38] J. Blazek, *Computational Fluid Dynamics: Principles and Applications*. Elsevier, 2015.
- [39] H. Childs, E. Brugger, B. Whitlock, J. Meredith, S. Ahern, D. Pugmire, K. Biagas, M. Miller, C. Harrison, G. H. Weber, H. Krishnan, T. Fogal, A. Sanderson, C. Garth, E. W. Bethel, D. Camp, O. Rübel, M. Durant, J. M. Favre, and P. Navrátil, “VisIt: An End-User Tool For Visualizing and Analyzing Very Large Data,” in *High Performance Visualization—Enabling Extreme-Scale Scientific Insight*, 2012, pp. 357–372.
- [40] J. A. Schetz and R. D. W. Bowersox, *Boundary Layer Analysis*. American Institute of Aeronautics and Astronautics, 2011.
- [41] L. Howarth, “Concerning the effect of compressibility on laminar boundary layers and their separation,” *Proceedings of the Royal Society of London A: Mathematical, Physical and Engineering Sciences*, vol. 194, no. 1036, pp. 16–42, 1948.

- [42] K. Ahnert and M. Mulansky, “Odeint — solving ordinary differential equations in C++,” *AIP Conference Proceedings*, vol. 1389, no. 1, pp. 1586–1589, 2011.
- [43] S. G. Johnson. The NLOpt nonlinear optimization package. [Http://ab-initio.mit.edu/nlopt](http://ab-initio.mit.edu/nlopt).
- [44] L. M. Brown, R. R. Boyce, N. Mudford, and S. O’Byrne, “Intrinsic three-dimensionality of laminar hypersonic shock wave/boundary layer interactions,” in *16th AIAA/DLR/DGLR International Space Planes and Hypersonic Systems and Technologies Conference, 2009*, AIAA 2009-7205.
- [45] L. Brown, “Intrinsic three-dimensionality of laminar shock wave/boundary layer interactions,” Ph.D. dissertation, University of New South Wales at the Australian Defence Force Academy, 2010.
- [46] J. Sivasubramanian and H. F. Fasel, “Numerical investigation of shock-wave boundary layer interactions in supersonic flows,” in *54th AIAA Aerospace Sciences Meeting, 2016*, AIAA 2016-0613.
- [47] J. C. Robinet, “Bifurcations in shock-wave/laminar-boundary-layer interaction: global instability approach,” *Journal of Fluid Mechanics*, vol. 579, pp. 85–112, 2007.
- [48] G. R. Inger, “Similitude properties of high-speed laminar and turbulent boundary-layer incipient separation,” *AIAA Journal*, vol. 15, no. 5, pp. 619–623, 1977.
- [49] E. R. G. Eckert, “Engineering relations for heat transfer and friction in high-velocity laminar and turbulent flow over surfaces with constant pressure and temperature,” *Transactions of the ASME*, vol. 78, pp. 1273–1283, 1956.

- [50] J. C. R. Hunt, A. A. Wray, and P. Moin, “Eddies, streams and convergence zones in turbulent flows,” Center for Turbulence Research, Tech. Rep., 1988.

## BIOGRAPHICAL STATEMENT

James Grisham was born in Bedford, Texas in 1987. He obtained a bachelors degree in aviation science with a business administration minor from Tarleton State University in 2009. He worked as a contract pilot and flight instructor for two years prior to joining the University of Texas at Arlington. He has spent five years as a graduate student at UT Arlington working under Drs. Frank Lu (advisor) and Brian Dennis (co-advisor). During his graduate studies, he completed two internships at NASA Langley Research Center.

His research interests include computational fluid dynamics, shock wave/boundary layer interactions, gas dynamics, finite element methods and scientific computing. He has been a graduate teaching assistant since 2012 and is a student member of AIAA.